IPP-Report

Max-Planck-Institut
für Plasmaphysik

Georg Schlisio

Analysis of the gas balance for Wendelstein 7-X

IPP 2021-09
März 2021

Analysis of the gas balance for Wendelstein 7-X

Inauguraldissertation

zur

Erlangung des akademischen Grades eines
Doktors der Naturwissenschaften
(Dr. rer. Nat.)

der

Mathematisch-Naturwissenschaftlichen Fakultät

der

Universität Greifswald

vorgelegt von
Georg Schlisio

Greifswald, 30.09.2020

Dekan	Prof. Dr. Gerald Kerth
1. Gutachter	Prof. Dr. Thomas Sunn Pedersen
2. Gutachter	Prof. Dr. Bernhard Unterberg
Tag der Promotion:	26.02.2021

Abstract

This work presents the first experimental investigation of the gas balance on the optimized modular stellarator Wendelstein 7-X (W7-X). A balance of all injected and removed particles and a measurement of internal particle reservoirs allows inference of the bound particle reservoir in the wall, which is of interest due to its effects on plasma density control and fuel retention. Different scenarios of the gas balance are presented with data from the operation campaign 1.2 with an inertially cooled graphite divertor. Both net outgassing and net retention scenarios are presented and W7-X is found to operate stable in a wide range of scenarios with varying wall conditions.

Since fusion experiments are conducted in ultra-high vacuum, suitable gauges are required for total and partial pressure measurement. The challenges and opportunities of the operation of pressure gauges in the steady magnetic field extending beyond plasma pulses are discussed. The performance of newly improved neutral pressure gauges, based on crystal cathode emitters is quantified. These provide improved operational robustness since they can be operated for long periods of time in strong magnetic fields. A crystal cathode setup and and its operation performance is presented along with a fast calibration scheme.

Partial pressure measurements provide additional important information complementing the total neutral pressure measurements, and allowing additional physics insights. As part of this thesis work, a new diagnostic of this kind was implemented on W7-X, the so-called diagnostic RGA (DRGA). It provides a wealth of information on various neutral gas species, with a relatively high time resolution - of order a few seconds. The diagnostic setup and its first results are presented in this thesis.

Zusammenfassung

Diese Arbeit stellt die erste experimentelle Untersuchung der Gasbilanz für den optimierten modularen Stellarator Wendelstein 7-X (W7-X) vor. Eine Bilanz aller injizierten und entfernten Partikel und eine Messung der internen Partikelreservoirs erlaubt die Rückschlüsse auf das in der Wand gebundene Partikelreservoir, was wegen seiner Auswirkungen auf die Plasmadichtekontrolle und die Brennstoffrückhaltung von Interesse ist. Verschiedene Szenarien der Gasbilanz werden mit Daten aus der Betriebskampagne 1.2 mit einem inertialgekühlten Graphitdivertor vorgestellt. Es werden sowohl Netto-Ausgasungs- als auch Netto-Rückhalteszenarien vorgestellt, und es wird festgestellt, dass W7-X in einem breiten Spektrum von Szenarien mit unterschiedlichen Wandbedingungen stabil arbeitet.

Da Fusionsexperimente im Ultrahochvakuum durchgeführt werden, sind geeignete Messgeräte zur Messung des Gesamt- und Partialdrucks erforderlich. Die Herausforderungen und Möglichkeiten des Betriebs von Druckmessgeräten im stationären Magnetfeld über die Plasmapulse hinaus werden diskutiert. Die Leistung neu verbesserter Neutraldruckmessgeräte, die auf Kristallkathoden-Emittern basieren, wird quantifiziert. Diese bieten einen robusteren Betrieb, da sie über lange Zeiträume in starken Magnetfeldern betrieben werden können. Ein Kristallkathodenaufbau und seine Betriebsleistung wird zusammen mit einem schnellen Kalibrierungsschema vorgestellt.

Partialdruckmessungen liefern zusätzliche wichtige Informationen, die die Messungen des Totaldrucks ergänzen und zusätzliche physikalische Erkenntnisse ermöglichen. Im Rahmen dieser Doktorarbeit wurde eine neue Diagnostik dieser Art auf W7-X implementiert, der sogenannte diagnostic RGA (DRGA). Sie liefert eine Fülle von Informationen über verschiedene neutrale Gasspezies mit einer relativ hohen Zeitauflösung - in der Größenordnung von wenigen Sekunden. Der Diagnostikaufbau und seine ersten Ergebnisse werden in dieser Arbeit vorgestellt.

Contents

1 Introduction

Life on Earth has been sustained by energy from the sun for billions of years and allowed development of life up to our modern human civilization. Since shortly after the discovery of nuclear fusion processes in the sun in the first half of the 20th century, scientists pursued the idea of utilizing the same processes as energy source for mankind. The fusion of light nuclei with release of thermal energy has since been experimentally demonstrated [1] and its associated state of matter — plasma — has been thoroughly studied[I]. To harvest macroscopic amounts of energy from fusion processes and compensate for energy expended for the reaction, a sufficient rate of fusion reactions has to be achieved.

There exists a variety of fusion processes with vastly different cross sections, translating into different reaction rates. Proton-proton fusion as in the sun exhibits a significantly lower cross section than deuterium-tritium (DT) fusion[II], which has the highest cross section of all reactions and strongly varies with temperature. Significant fusion rates are reachable at about 150 million kelvin, or 13 keV. At such temperatures, matter only exists as plasma, an ionized gas where atoms are fully ionized and interact with electric and magnetic fields.

The main challenges of fusion in regard to energy production are not a lack of knowledge of nuclear processes, but rather associated with the plasma state of matter. A major focus in fusion energy research is therefore the study of *high-temperature plasma physics*. Long-time confinement of hot particles and exhaust of the thermal and neutronic energy pose the main questions in fusion research today. One measure of performance of a fusion plasma is the *triple product*, the

[I] Shafranov wrote an entertaining overview over the first twenty years of of concentrated fusion research in the mid 20th century [2].

[II] DT fusion: $^{2}\mathrm{H} + {}^{3}\mathrm{H} \rightarrow {}^{4}\mathrm{He} + \mathrm{n} + 14\,\mathrm{MeV}$

product of ion density n_i, energy confinement time τ_E and ion temperature T_i. It can be derived from the *Lawson criterion* [3] and has to exceed a certain value. A minimum in the required triple product for DT fusion is reached at around 25 keV.

Sustaining temperatures and densities required by fusion can be accomplished with magnetic fields due to the Lorentz force. Toroidal topologies with a twisted magnetic field are the most researched configuration to shape a hot plasma without contact to any solid surface. This twisted magnetic field, being a vector field, can be split into a toroidal and a poloidal magnetic field component. The representation of the magnetic field twist is the *rotational transform* ι proportional to the ratio of poloidal and toroidal turns of a given fieldline. The radial derivative of ι is known as *shear*.

The toroidal field is commonly produced by a set of coils arranged as torus. For the poloidal field generation there exist two competing concepts. In a *tokamak* a strong toroidal plasma current induces a toroidally symmetric poloidal field [4]. This current can reach several mega ampere and gives rise to many effects. While the current contributes to plasma heating via ohmic losses which is welcome, it also causes instabilities which can lead to a fast decay of toroidal current associated with sudden energy deposition on the wall of the fusion device, a so-called disruption [5]. Additionally, the ohmic losses require constant current drive which is typically achieved with a transformer setup. Due to Faradays law, only a changing transformer current can drive a plasma current. Limits in the maximum transformer current thus limit the duration of the plasma pulse, which is typically in the order of tens of seconds for currently operating experiments.[III]

In a *stellarator*, both poloidal and toroidal magnetic field are produced by external field coils, and no plasma current is necessary. While this solves current induced instabilities and makes steady-state magnetic fields a matter of coil operation, it comes at the cost of more complicated coil shapes, a need for optimization and an inherently three-dimensional machine with only discrete symmetries. While the first stellarator, proposed by Spitzer in 1958 [7], employed multiple coil sets, of which at least one had to fully extend around the whole experiment, later optimizations lead to a modular coil set [8, 9]. Due to the inherently three-dimensional nature of stellarators, effective optimization only became possible when computers evolved to be powerful enough to be used

[III] Much longer plasma pulses have been achieved with various current drive methods, but not at reactor-relevant plasma parameters [6].

for such calculations in the late 1980s. Around that time, several stellarator experiments were proposed, among them the large helical device (LHD) and Wendelstein 7-X (W7-X).

The tokamak was invented by Sacharov and Tamm at the Kurchatov institute in Moscow in 1952 and has dominated fusion research for over five decades after a demonstration of exceptionally good energy confinement and high plasma temperatures compared to other magnetic confinement approaches at the time. Over time, it has made tremendous progress in terms of achieved triple product value, plasma control, exhaust concepts and operation modes, has experimentally demonstrated DT fusion [10] and is now going to become the first fusion reactor, which is built as ITER (*latin*: the way), a joint undertaking of the largest economies in the world. Many of the plasma physics and technological breakthroughs achieved in tokamaks have significance for the stellarator as well, e.g. the exhaust concept with a divertor instead of a limiter, plasma heating mechanisms and plasma diagnostics.

To mitigate energy loss from the plasma [11] and achieve the required plasma temperatures, fusion experiments are conducted inside a vacuum vessel at particle densities significantly below atmospheric density.

According to the *European Research Roadmap to the Realization of Fusion Energy*[IV], commercial reactors are foreseen after the intermediate steps of ITER and Demonstration Power Plant (DEMO). The ITER tokamak[V] is currently under construction in southern France and aims at 500 MW (thermal) DT fusion power, which allows development of tritium breeding technology required for the fuel cycle [12]. DEMO is in an early design phase and it is yet to decide whether it becomes a tokamak or a stellarator. The DEMO machine is dedicated to demonstrate the full fuel cycle and also should be the first fusion device delivering power to the grid, although not at economic costs yet.

1.1. The exhaust problem

One major challenge for sustained fusion energy production is to have sufficient large energy confinement simultaneously with an efficient particle exhaust. Energy confinement is required to keep central ion temperatures high enough for sufficient fusion reactions, particle exhaust is required to remove fusion products

[IV] https://www.euro-fusion.org/eurofusion/roadmap/
[V] https://iter.org

(He in case of DT fusion) and impurities from wall interactions. The inherent coupling of energy and particle transport by convective transport leads to a conflict of interests, and requires a trade-off between the goals. Many concepts were developed to locally influence plasma behavior towards either goal, such as H-mode [13], detachment [14], divertors [15] and others. The goal of all these is optimization of particle exhaust and isolation of the core from impurities with as good as possible energy confinement.

Magnetically confined plasmas generally extend all the way to the material objects that surround the plasma. Early plasma experiments utilized dedicated *limiters*, special tiles optimized for direct plasma contact, to restrict the plasma expansion. With a limiter, the last closed flux surface (LCFS) separating the confined plasma core with closed field lines from the outer scrape-off layer (SOL) with field lines intersecting solid surfaces is also the point of most intense plasma-surface-interaction, allowing easy influx of impurities into the confined plasma thereby degrading the plasma performance.

A solution to this problem was found with the *divertor* [16] and reduced impurity influx was verified in various experiments [15, 17], and lead to the discovery of a high-confinement regime (H-mode) in the *axialsymmetrisches Divertor-Experiment* (ASDEX) tokamak [17]. The introduction of an external magnetic field creates an X-point and spatially separates the plasma-wall-interaction point from the LCFS. Many different divertor concepts have been developed and experimentally tested in tokamaks, to enhance particle exhaust while protecting the confined plasma from wall interaction byproducts. In stellarators, more divertor concepts are feasible. The resonant divertor makes use of intrinsic magnetic islands [18] forming at rational ι surfaces and is the divertor concept used in W7-X introduced in section 1.2. The ergodic divertor of LHD uses the stochastization effect from overlapping islands due to strongly varying ι (high shear).

Due to the aforementioned coupling of particle and energy transport, significant amounts of energy need to be exhausted along with the particles and pose a great challenge for the divertor plates. Typical limits for continuous heat load on divertor plates are $10\,\mathrm{MW/m^2}$, for transient loads up to $25\,\mathrm{MW/m^2}$.[VI] Possible means for first wall heat load reduction are a reduction of plasma incident angle on the divertor target plates and plasma energy dissipation before

[VI] For comparison: Peak heat flux at space shuttle reentry: $0.5\,\mathrm{MW/m^2}$, electrical welding: $15\,\mathrm{MW/m^2}$, average heat flux on solar surface: $63\,\mathrm{MW/m^2}$, solar constant (solar radiation on earth orbit): $1.3\,\mathrm{kW/m^2}$.

particles reach the divertor plates. Shallower angles lead to a wider spread of flux across the surface, but require well-controlled alignment between the divertor surface and the magnetic field. Plasma cooling before reaching the divertor is achieved by injection of strongly radiating impurity gases or an increase of neutral particle density in front of the divertor plates, which act as neutral cushion and dissipate energy by collisonal cooling and neutralization of ions with neutral gas, so-called *detachment* [14].

The very demanding conditions at the divertor target plates require a careful selection of materials for the plasma-facing components. Traditionally, graphite tiles were widely used due to easy availability, good machining properties, high temperature stability, lightweight but stable structure and radiative self-cooling in overload conditions. However, large fuel retention in graphite and derived materials, like carbon fibre reinforced carbon (CFC), lead to the conclusion, that graphite is not able to comply with regulative rules regarding radioactive tritium and also poses a problem for the fuel cycle, where tritium is rare and needs to fully recirculate if it is not used up in fusion processes. Exemplary calculation for a graphite ITER estimate an order of 100 plasma pulses before the tritium inventory exceeds the legal limits [19]. Alternative first wall materials under consideration are beryllium and tungsten as well as liquid metal divertor concepts. The most advanced material so far is tungsten, which has much lower tritium retention, but however is much heavier than carbon, rare and thus expensive, brittle, reactive and also has a liquid phase, which can cause problems in overload scenarios. Tungsten has been used as first wall material successfully in Joint European Torus (JET) and ASDEX Upgrade (AUG) and is also foreseen as divertor material in ITER.

Despite the developed technical solutions and sophisticated material, the power load on the divertor remains one of the central challenges for fusion. Recent promising results [20] on island divertors in stellarators indicate a much larger contact area between plasma and divertor leading to spread out power deposition leading to lower peak heat fluxes onto the divertor. The physics of plasma-wall interaction (PWI) is a rich field of research and falls mostly under the domain of material science, where materials of different compositions are exposed to fusion-relevant conditions and investigated for their properties regarding fuel retention, heat load tolerance, neutron damage, chemical and mechanical sputtering and other aspects. This thesis is concerned with the mutual influence of plasma and wall in terms of particle exchange. The employed method is a balance of all involved particle reservoirs to infer the bound particle

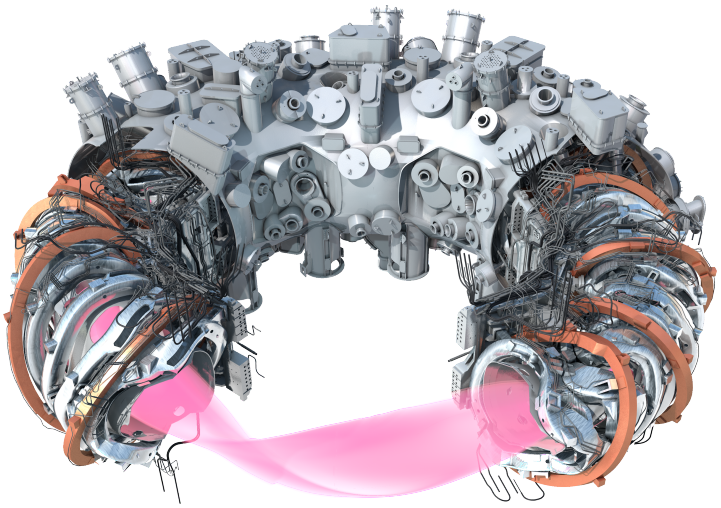

Figure 1.1.: CAD rendering of the W7-X experiment with cut away layers. From inside out: The plasma is shown in pink, surrounded by the plasma vessel (grey), the nonplanar (silver) and planar (orange) coils and the cryostat vessel (also grey). ©IPP

number and is presented in chapter 3.

1.2. Wendelstein 7-X

W7-X is the latest experiment of a line of stellarator experiments conducted at the Max-Planck Institute for Plasma Physics (IPP) in Germany since the 1960s.

It is an optimized modular stellarator with a five-fold symmetry and superconducting magnetic field coils [21]. Modularization allowed to avoid building a coil encompassing the whole machine in one, but instead building modular coils of a more complex geometry. The main magnetic coil system of W7-X consists of 70 superconducting magnets of seven different shapes, 50 non-planar coils producing the twisted magnetic field and 20 planar coils for greater flexibility in magnetic configuration space.

Figure 1.1 shows a cut of the W7-X device. The central plasma is surrounded by a plasma vessel (PV) adapted to the plasma shape, on which the superconducting coils are mounted. An outer cryostat vessel surrounds the PV as well as the coil system and completes the outer shape. Key technical figures are given

Number of modules	5
Major radius	5.5 m
Minor radius	0.55 m
Plasma volume	28 m^3
Plasma vessel volume	110 m^3

Table 1.1.: Key technical figures of the Wendelstein 7-X stellarator experiment.

in table 1.1.

W7-X was optimized for low parallel plasma current, low neoclassical transport, good trapped particle confinement as well as a number of other optimization criteria [22] of which some have already been experimentally verified [23].

The divertor of W7-X is designed as a segmented divertor, intersecting the magnetic islands in each module [24]. An image of the divertor and surrounding baffles is shown in figure 1.2. The divertor was designed as an open divertor to allow many different magnetic configurations of the versatile magnetic coil system. There exist ten divertor modules, one upper and one lower in each stellarator symmetric module. The divertor modules are about 4 m long and consist of different parts used in different magnetic configurations. The most distinguished difference from the so-called *standard magnetic configuration* is the *high iota* configuration, where the main contact point of plasma and divertor shifts from the *low iota* part used in *standard* configuration[VII] to the *high iota* part. These two parts of the divertor have separate pumping gaps and pumping systems.

The concept of W7-X was first presented in 1988 and assembly started in 2005. A commissioning campaign (operation phase (OP) 1.1) with incomplete wall protection and a graphite limiter was conducted in late 2015 and early 2016 where plasma pulse lengths up to 6 s were achieved [25]. In 2017 and 2018, two campaigns (OP 1.2a and b) were conducted with an inertially cooled fine-grain graphite divertor and complete first wall protection [26]. The inertially cooled divertor was limited with respect to the heating energy, but provided a valuable opportunity to explore divertor operation in this new machine with a robust but not steady-state capable plasma-wall interaction device. The maximum plasma duration was extended to 100 s at 2 MW of heating power. For the upcoming

[VII] In fact, all configurations except *high iota* configuration have their wall contact on the low iota part of the divertor.

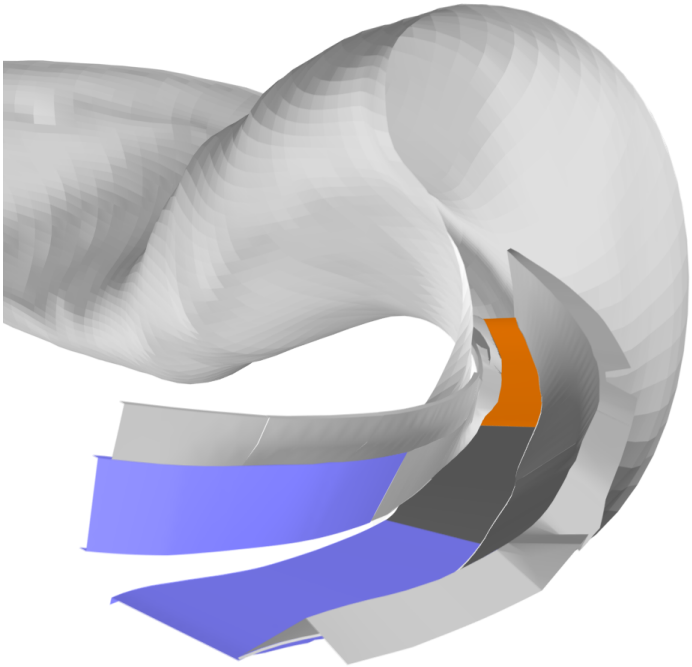

Figure 1.2.: Visualization of the W7-X plasma vessel (grey) and the plasma-facing components. The *low iota* horizontal and vertical target shown in blue, the central part in dark grey, the *high iota* horizontal target in orange and the surrounding baffles in light grey. Only the lower divertor is shown, a flip-symmetric assembly exists in the top part and together they form one module.

plasma campaign OP 2, currently planned for 2022 and beyond, a water-cooled CFC divertor is installed for steady-state operation and the inertially cooled divertor was removed from the PV. The maximum foreseen plasma duration is 30 min at 10 MW of heating power.

The first wall of W7-X besides the divertor is a combination of graphite tiles on the baffles and heat shield and stainless steel wall panels [27]. Due to the well-known fuel retention properties of graphite [19] and promising results with metal divertors [28] a future replacement of the W7-X divertor with a tungsten redesign is in an early planning phase.

With all the described features W7-X is currently the most advanced stellarator experiment.

2

Neutral gas diagnostic system at Wendelstein 7-X

The plasma vessel of W7-X has a volume of about 110 m^3 and experiences pressures in the range of $1 \cdot 10^{-7}$ mbar to $1 \cdot 10^{-2}$ mbar. The magnetic field strength on-axis is between 2.5 T to 3 T, reaches a maximum of 7 T near the coils and then falls off quickly to several mT in the torus hall. Due to strong electron cyclotron resonance heating (ECRH), a microwave background radiation level exists during plasma operation, and its magnitude varies greatly depending on the position in the vessel, the applied heating method and plasma conditions. All diagnostics need to deal with these external factors without disturbing the vacuum conditions or plasma-confining magnetic field.

As in every ultra-high vacuum (UHV) device, one needs to monitor both total and partial pressure in different situations, and W7-X is equipped with a number of diagnostics to achieve that.

The operation of pressure gauges in a stellarator with stable magnetic field beyond the plasma phase presents new opportunities and challenges. The main opportunity is the possibility to monitor outgassing phases, while the main challenge is the much extended operating time of the gauges.

2.1. Hot cathode manometers

The main total pressure sensors during an experiment are descendants of the so-called ASDEX pressure gauge (APG), a hot cathode gauge developed at IPP in the 1980's and further refined since then [11]. Its basic principle is an accelerated electron beam in a sample volume, impact-ionizing residual gas ions. An

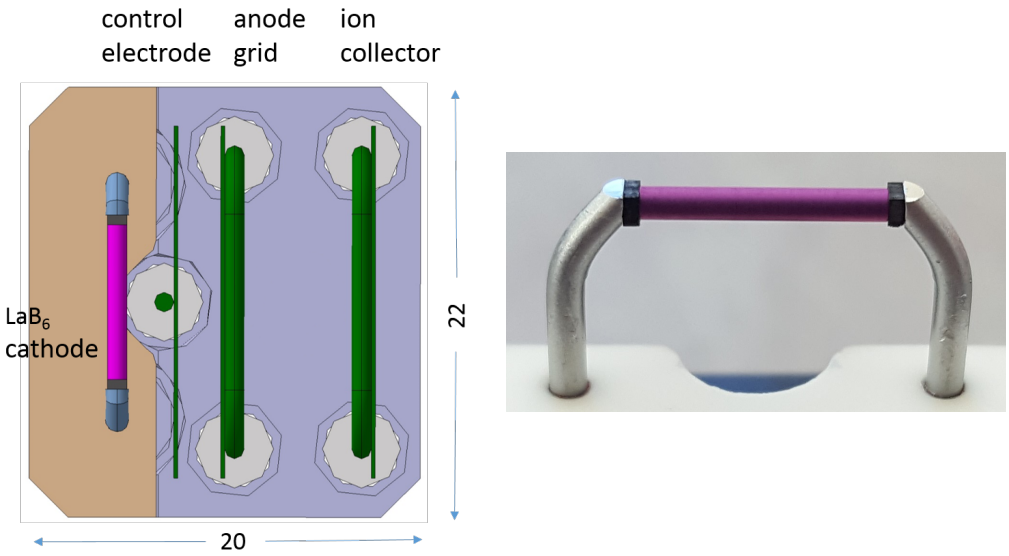

Figure 2.1.: **Left**: Schematic view of the grid assembly of a crystal cathode pressure gauge (CCPG) manometer head, size in mm. The magnetic field vector is aligned along the horizontal axis in the picture. Taken from article III, see there for photo of assembly. **Right**: Closeup photo of a lanthanum hexaboride (LaB_6) crystal cathode setup. The purple crystal of 8 mm length and 1 mm diameter is clamped between two molybdenum-rhenium posts mounted on a ceramics base plate. Black plates of pyrolithic graphite between the crystal and the rod with higher resistance act as heaters for the crystal.

aligned electric field collects the ions on collector plates, which yields a current proportional to the particle number and thereby allows inference of total particle density.

The electron beam is created from a heated cathode, hence the name, and, in case of the APGs, controlled by a set of grids. Strong magnetic fields confine the electrons and require alignment of the gauge axis parallel to the magnetic field vector $\vec{B}$ to ensure electrons can reach the sample volume. This alignment then requires the typically ohmically heated cathode to be perpendicular to the magnetic field, which yields a $\vec{j} \times \vec{B}$ force on the cathode filament. In the case of APGs, the cathode is a thoriated tungsten filament heated with approximately 20 A, which results in a force of 3 N for the case of 3 T and a filament length of 5 cm. These forces are well known and have not played a major role in short

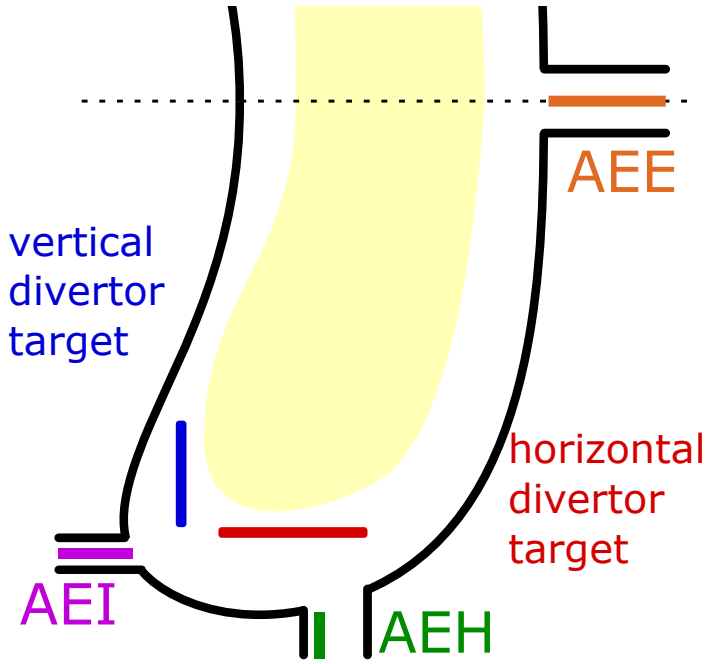

Figure 2.2.: Schematic poloidal cut of the W7-X plasma vessel. The dashed black line indicates the horizontal symmetry plane, the major radius increases from left to right. Total pressure gauge positions are indicated along with the low iota part of the divertor target plates in blue (vertical) and red (horizontal): AEE - outer midplane, AEH - pumping port, AEI - pumping gap. Central yellow shade symbolizes confined plasma region, additional in-vessel components, such as baffles and heat shields, are omitted. Reproduced from article I, adapted from article III.

pulse operation as typically seen in tokamaks, but become problematic for long pulse operation, as expected in W7-X, ITER and future fusion reactors [29].

At W7-X, a new type of cathode has been proposed, built and tested, consisting of an indirectly heated crystal held in position by two posts [30]. Due to the high electrical conductivity of the crystal material, a direct ohmic heating is not practical, and one pyrolithic graphite block on each end is used to heat the crystal by heat conduction. Most successful operation of this crystal cathode pressure gauge (CCPG) so far has been conducted with lanthanum hexaboride

(LaB_6), reported in article III, but investigation of several metal carbides are ongoing to avoid neutronic transmutation of boron in view of future application in neutron rich environments. Figure 2.1 shows a pressure gauge and crystal cathode setup, distribution of measurement positions is shown in figure 2.2.

These gauges require a calibration to relate the measured ion current to the pressure present in the device. Due to the sensitivity of the calibration to the field alignment, this calibration was conducted in the machine after vacuum bake-out. To efficiently calibrate all sensors at once, the torus was filled with gas to a number of static pressure steps. This was achieved by closure of all gate valves and injecting precalculated amounts of gas into the evacuated torus. The obtained signal was related to the total pressure signal obtained from a number of pre-calibrated capacitance manometers with a linear fit-function $p = c \cdot I_i$ appropriate for the linear range between the x-ray limit at pressures below $5 \cdot 10^{-7}$ mbar and the high-pressure plasma ignition limit above 0.1 mbar. Article III contains further information on the calibration procedure as well as the longterm stability observed in W7-X OP 1.2b.

Due to the gas-type dependence of ionization gauges, an assumption about main species or a combination with a residual gas analyzer (RGA) can improve accuracy. That topic is discussed in section 2.3.

2.2. Cold cathode manometers

In contrast to a hot cathode gauge, a cold cathode gauge does not produce an electron beam to ionize residual gas, but instead uses high voltage to break down neutrals and ignite and confine a plasma inside the gauge. The discharge current varies with density and allows inference of the neutral density. Most commonly, a Penning trap [31] is used for this kind of assembly.

In W7-X, two types of cold cathode gauges are in use: commercial Penning gauges with integrated electronics and own magnetic field, typically run as pre-calibrated longtime pressure monitoring tool of vacuum components and combined with a thermal conductivity gauge, a so-called Pirani gauge [32]; and a Wisconsin In-Situ Penning (WISP) gauge [33], developed to use the intrinsic magnetic field of W7-X and optimized for fast observation of high pressures in the sub-divertor chamber. The WISP gauge can be equipped with an optical fiber to spectroscopically monitor the light emission of the small cold plasma inside the gauge and thus infer partial pressures from the emission line ratios,

making it an optical gas analyzer (OGA).

While the first type of gauges is used as machine instrumentation pre-calibrated for nitrogen and is recorded at a sampling rate of only 1 Hz, the WISP is designed to act as fast neutral diagnostic and is sampled in the kHz range. Machine instrumentation gauges are useful to monitor long term trends during long outgassing phases between experiments or over night between experiment days.

Just as hot cathode gauges, the cold cathode gauge signal also depends on the gas type and combination with an RGA allows to improve accuracy.

2.3. Residual gas analysis

Dedicated partial pressure analysis is often done with residual gas analyzer (RGA)s, which use several methods of detection. One method is the aforementioned optical observation of characteristic light emission (OGA), which is, however, mostly restricted to hydrogen isotopes and helium due to the complex spectroscopic nature of other gases. Most other methods are based on ionization and moderate acceleration of the probed gas, mass filtering and subsequent detection. Many kinds of mass filters have been invented, of which the quadrupole mass filter [34], the omegatron [35] and the ion trap [36] are the most notable ones.

Quadrupole mass filters are used in quadrupole mass spectrometer (QMS) setups and allow very compact setup, a wide mass range and a high sensitivity, which leads to frequent use for operational vacuum monitoring as well as for diagnostic purposes. A stable trajectory in a quadrupole mass filter is described by a set of differential equations, the Mathieu equations [37] and characteristic for one mass over charge (m/Z) value.

Omegatrons have very high resolution for low masses and allow distinguishing hydrogen species. Due to the need of an external magnetic field, they often require a bulky external magnet, but could potentially be used inside the plasma vessel in magnetic confinement fusion utilizing the intrinsic magnetic field, like the WISP gauges. So far, they have been used in Alcator C-MOD [38], but are not present in any currently operating machine. While their properties promise to deliver high time- and m/Z resolved spectra especially for light gases, susceptibility to pressures above approximately $1 \cdot 10^{-5}$ mbar and a requirement of accurate field alignment are potential problems for the application of omega-

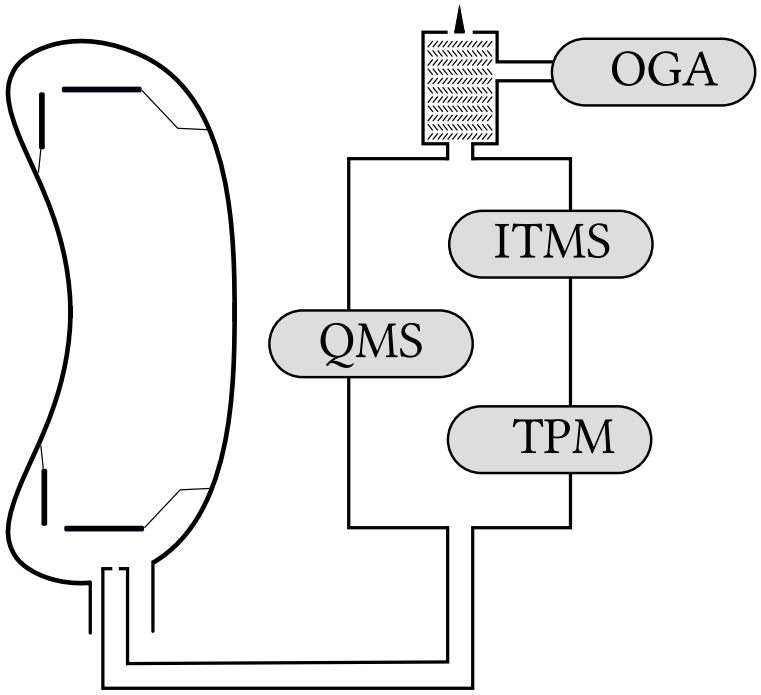

Figure 2.3.: Schematic view of the diagnostic RGA (DRGA) concept as applied at W7-X. Plasma vessel cross section with baffled divertor on the left, DRGA sampling tube and analysis chamber with measurement systems and exhaust on the right: quadrupole mass spectrometer (QMS), ion-trap mass spectrometer (ITMS), optical gas analyzer (OGA), total pressure measurement (TPM). The OGA is connected to an inter-stage port of the turbomolecular pump for higher working pressure. Geometry and sizes not to scale.

trons in fusion research.

A Paul trap is the base of an ion-trap mass spectrometer (ITMS) and is also an application of the Mathieu equations. In contrast to the quadrupole mass filter, it selects ions solely with alternating electric fields that create m/Z selective potential well. A thorough treatment of ITMS physics was given by R. E. March [39].

Except for the OGA, the RGAs are based on the concept of free streaming ionized particles and suffer from external magnetic stray fields, which are unavoidable to a certain degree in magnetically confined fusion experiments. To still be able to utilize QMSs and ITMSs in magnetic confinement fusion, the

concept of a diagnostic RGA (DRGA) was developed [40].

It combines an external analysis chamber in a field reduced area equipped with a number of RGAs with a pressure-reduced sampling tube from the region of interest inside the plasma vessel. A schematic view is shown in figure 2.3. Low pressure in the sampling tube and analysis chamber allows gas transport in the molecular flow regime, where gas propagation is dominated by collisions with the wall and the characteristic velocity is the thermal speed of the molecules.

This concept was developed with the requirements of ITER in mind and a prototype diagnostic RGA (P-DRGA) was built and lab-tested [41]. The prototype did not include a sampling tube and used a gas mixing station as gas source. For OP 1.2b, the opportunity arose to integrate the P-DRGA at W7-X, equip it with a simple sampling tube and operate it in the first divertor campaign. Integration and construction of the sampling tube required some technical solutions, which are reported in article II together with first results of the operation during OP 1.2b. After the successful operation the P-DRGA is now being improved for W7-X OP 2.

The diagnostic RGA concept includes an OGA as well, where exhaust gas is spectroscopically monitored in a Penning trap. An inter-stage port of the diagnostic turbomolecular pump is used to get a higher pressure and enhance light yield. This system has been developed and tested separately in deuterium-tritium environments at JET [42].

The test of the P-DRGA at W7-X presents an important step towards the *latin*: the way, first fusion reactor (ITER) DRGA, as it allows experimental validation of the sampling tube concept. The design for the ITER DRGA, intended for fuel monitoring of exhaust gases of the test reactor, includes a double-walled heated sampling tube to reduce sticking of gases on the wall.

W7-X is also equipped with a number of QMS for operational purposes, mainly leak checking during commissioning and long term monitoring of vacuum conditions. Due to insufficient shielding against magnetic stray field their data is only usable for qualitative trend assessment.

3
Gas balance method

As discussed in chapter 1, as the plasma flows out from the flux surfaces, it enters and streams along magnetic field lines that intersect material surfaces. Besides direct collision with wall tiles, the plasma can also emit fast neutral particles from charge exchange[I] or radiation absorbed by the wall. All these processes transfer particles and/or energy to the wall and lead to a rich class of phenomena.Particles can be retained and released from wall surfaces, depending on the material properties, temperature, and concentrations inside and outside of the material.

The evolution of the wall particle inventory can not directly be measured in real time, but inferred only from its influence on other quantities accessible by measurement. This can be achieved by means of a *gas balance*, which is based on the assumption of a continuity equation:

$$\text{Injected} - \text{removed} = \text{content} - \text{prior content}\,. \tag{3.1}$$

The particle content can then be further split up into free and bound particles N_w, the free particles again into neutral particles N_n and ionized particle molecular equivalent N_p. Since we account for particles in their chemically stable state, the neutral particle number might differ from the ionized particle number. To avoid misconceptions, we refer to the plasma reservoir size as its *molecular equivalent*, related to the ionized particle number by the number of atoms per molecule $n_{\mathrm{at},a}$ of species *a*. Figure 3.1 shows a scheme of the introduced reservoirs.

[I] A faster hydrogen ion and a slower hydrogen atom or molecule exchange an electron and the fast and now neutral particle transfers energy to the wall.

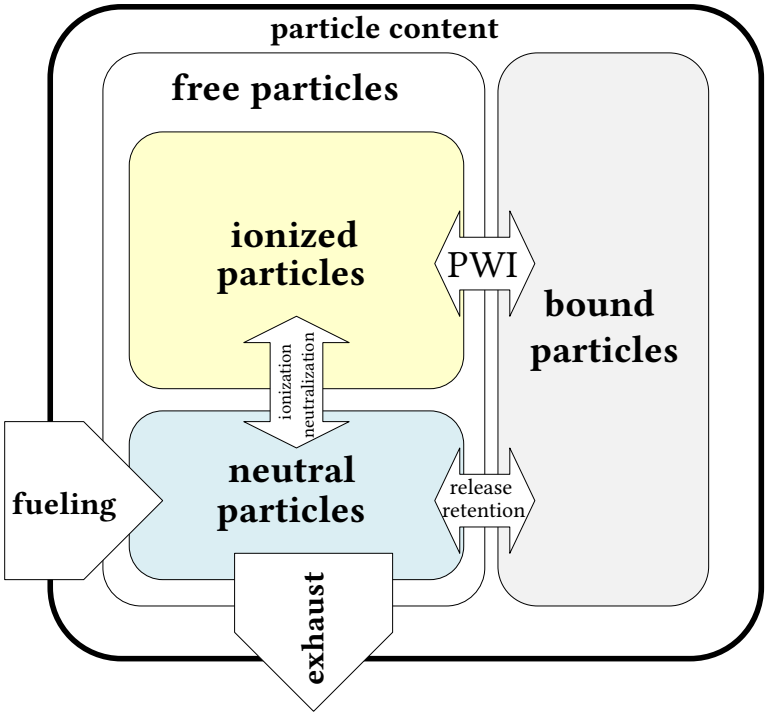

Figure 3.1.: Schematic view of the reservoir model. The outer contour symbolizes the plasma vessel, subdivision of the particle content according to equation (3.2). Arrows indicate migration between reservoirs and are annotated with the main mechanisms. The role of NBI is left out for simplicity. Reproduced from article I.

The balance can then be formulated for every gas species:

$$\int_{t_0}^{t} \dot{N}_{\mathrm{in},a} - \int_{t_0}^{t} \dot{N}_{\mathrm{out},a} = N_{\mathrm{n},a} + N_{\mathrm{p},a} + N_{\mathrm{w},a} - N_{\mathrm{w},a,0} + S_{+,a} - S_{\text{-},a}\,, \tag{3.2}$$

where $\dot{N}_{in}$ denotes the injection rate and $\dot{N}_{\mathrm{out}}$ denotes the removal rate. Chemical conversions, such as methanization, oxidation, ammonia formation and nuclear conversions such as helium formation in a fusion reactor, are accounted for by the source and sink terms S_{+} and $S_{\text{-}}$, respectively, in this balance. In W7-X these terms are negligible and dropping them is a good approximation for working gases in non-fusing plasma physics experiments.

Fusion experiments are typically operated in a pulsed mode, where pulse length can vary from seconds to hours. For that reason, the gas balance is often evaluated per pulse, but also over multiple pulses or even a full experimental campaign. The chosen scenario defines temporal start and end point of equation (3.2) and determines, if e.g. N_p drops to zero between pulses.

The model presented in this chapter is not easily implemented in fusion experiments, since it requires detailed measurement of partial pressures and plasma composition as well as close monitoring of plasma and surface chemistry. Article I explains a practical implementation of this balance on W7-X for hydrogen in OP 1.2.

3.1. Reservoirs

3.1.1. Injected particles

The injection rate $\dot{N}_\mathrm{in}$ is given by all external particle sources in the experiment. In W7-X there are the following sources:

- main gas fueling system [43]
- diagnostic gas beams: He beam [44], alkali beam [45], gas puff imaging [46]
- neutral beam injection (NBI) [47]
- frozen hydrogen pellet injection [48, 49]
- tracer-encapsulated solid pellet injection [50]
- leaks

While fueling systems are often very well calibrated for the injected particle number, other system influences on the gas balance are only secondary focus of the design and operation and might not be sufficiently monitored. Typically though, it is sufficient to monitor the main gas sources or restrict the investigation to pulses with minor interference from unaccounted systems.

The NBI system is designed to inject fast neutral particles into the confined plasma region, where they ionize by collisions and contribute to plasma particle and energy content. Due to the nature of neutral beam systems, a significant

amount of slow neutral particles can be injected as well. These either originate from the neutralizer or from beam losses to the duct, which can induce strong outgassing of the duct walls. The role of a NBI system is potentially complex and is very specific to the used NBI system and experiment setup.

3.1.2. Removed particles

The removed particle rate $\dot{N}_{\text{out}}$ is given by all permanent gas sinks. The exhaust rate Q is given by the product of pumping speed S and pressure p at the pump flange, and can be converted to a particle flux with the ideal gas law using the gas temperature T:

$$Q = p \cdot S\,, \tag{3.3}$$

$$\dot{N}_{\text{out}} = \frac{Q}{k_{\text{B}} T}\,. \tag{3.4}$$

Several technologies are in use for vacuum pumping in fusion devices. The most common technology in high vacuum applications is the turbomolecular pump (TMP). Rotating blades at high speeds in combination with a static blade assembly accelerate gas particles towards the exhaust and high compression can be reached with this setup. The pumping speed varies with molecular mass, due to a varying capturing factor inside the pump geometry [51].

Cryo pumps consist of a set of plates at cryogenic temperatures where impinging gas is frozen out and thus trapped in a layer of increasing thickness. Once the capacity is exhausted, cryo pumps are regenerated by heating the panels above melting temperature of the gettered gases, which are then typically pumped with turbomolecular pump (TMP)s. The pumping speed of cryo pumps depends on the gas type as well as on the filling rate and typically decreases over time.

Another type of getter pumps use chemical getter layers to trap particles, often titanium is used. A pump surface is exposed to a layer of active material, e.g. by evaporation from a ohmically heated wire coated with titanium, and chemically binds impinging gas molecules. Like cryo pumps, these chemical getter pumps require regeneration as well, which is achieved by renewing the active layer on top of the saturated layers from previous usage. After accumulation of thick layers, these can start flaking off and pollute the vacuum chamber and mechanical cleaning is required. Much like cryo pumps, the pumping speed

decreases with gas uptake and depends on chemical properties of the pumped gas as well.

In W7-X the main vacuum system consists of 30 TMPs with a total pumping speed at the plasma vessel of about $30\,\mathrm{m}^3/\mathrm{s}$ (in hydrogen) and for OP 2 10 cryo pumps with a total pumping speed of $75\,\mathrm{m}^3/\mathrm{s}$ (in hydrogen) are installed. TMPs are in use also in several diagnostics, which usually contribute little to the total particle removal rate due to small pumping speed, low pressure at the pumped location and intentional restriction of gas flow by apertures. The NBI system is the only system in W7-X besides the main vacuum pumps exhausting a significant amount of particles. The NBI box is equipped with a small TMP and large titanium getter pumps with a maximum pumping speed of approximately $500\,\mathrm{m}^3/\mathrm{s}$. A thorough analysis of the W7-X NBI gas balance in terms of both total particle injection (fast and slow) and particle removal remains to be done.

3.1.3. Neutral particle content

The neutral particle content inside the plasma vessel is accessible by pressure measurement and geometric assumptions. For a given partial pressure p_a, a volume V_n and temperature T the ideal gas law again allows to calculate the total particle number of species a:

$$N_{\mathrm{n},a} = \frac{p_a V_\mathrm{n}}{k_\mathrm{B} T}\,. \tag{3.5}$$

A gas temperature is rarely measured and might not even exist in a strict sense, e.g. due to a velocity distribution disturbed by fast neutral particles from charge exchange or dissociation. Also, one needs to account for a time-dependence of the volume. Inside the confined plasma, neutral density is very low due to the rapid ionization of neutrals as they enter the hot, dense plasma.

With the plasma making wall contact at the divertor, it creates a barrier for neutral particles and separates the main chamber neutral reservoir from the sub-divertor neutral reservoir with pressure differences up to two orders of magnitude. This effect is referred to as *divertor plugging*. It allows a separate calculation of neutral sub-reservoirs with separate pressure measurement, volume and even temperature assumptions, which are then combined into the total neutral number $N_{\mathrm{n},a}$. As discussed in chapter 2, gas-type resolved partial pressure measurement requires high effort and presents a serious obstacle for trace gases.

The total pressure is much easier accessible and serves as a good estimate for the partial pressure of majority gases.

Pressure measurement is always a local measurement and needs to be extrapolated to surrounding volumes. The boundaries of these volumes have a complicated shape and the transition into the plasma is a gradual process. This limits the accuracy of neutral reservoir estimation, and assumptions about all the aforementioned conditions need to be made. These can be aided with simulations, e.g. with the EMC3-Eirene code [52]. Figure 3.2 shows simulation results of neutral gas temperature and pressure for the case of molecular hydrogen in W7-X. While the temperature of neutrals rises by more than two orders of magnitude inside the dense confined plasma, the density decreases even stronger. This justifies to assume a negligible molecular density in the plasma. The separation of the volumes in the main chamber and below the divertor with distinctly different pressure as explained above is also supported by this simulation. Corresponding total pressure gauge positions are shown in figure 2.2.

3.1.4. Plasma molecular equivalent

Under the assumption that in the plasma all atoms are fully ionized, one can derive the molecular equivalent of plasma particles for each species from the electron density n_e and the species fractions $f_a = n_a/n_\mathrm{e}$ for species *a*. From the neutrality assumption follows

$$n_\mathrm{e} = \sum_i Z_i n_i \,, \tag{3.6}$$

$$f_a = \frac{1 - \sum_{i \neq a} Z_i f_i}{Z_a} \,, \tag{3.7}$$

with the mean electron density n_e, atomic charge number Z_a, ion density n_a for species *a*. The total molecular equivalent follows then as

$$N_{\mathrm{p},a} = \frac{n_\mathrm{e} V_\mathrm{p}}{n_{\mathrm{at},a}} \cdot f_a \tag{3.8}$$

$$= \frac{n_{\mathrm{e},l}\, V_\mathrm{p}}{n_{\mathrm{at},a}\, l} \cdot \frac{1 - \sum_{i \neq a} f_i Z_i}{Z_a} \tag{3.9}$$

with the number of atoms per molecule $n_{\mathrm{at},a}$ and the plasma volume V_p. In W7-X the mean electron density can be derived from the line-integrated electron

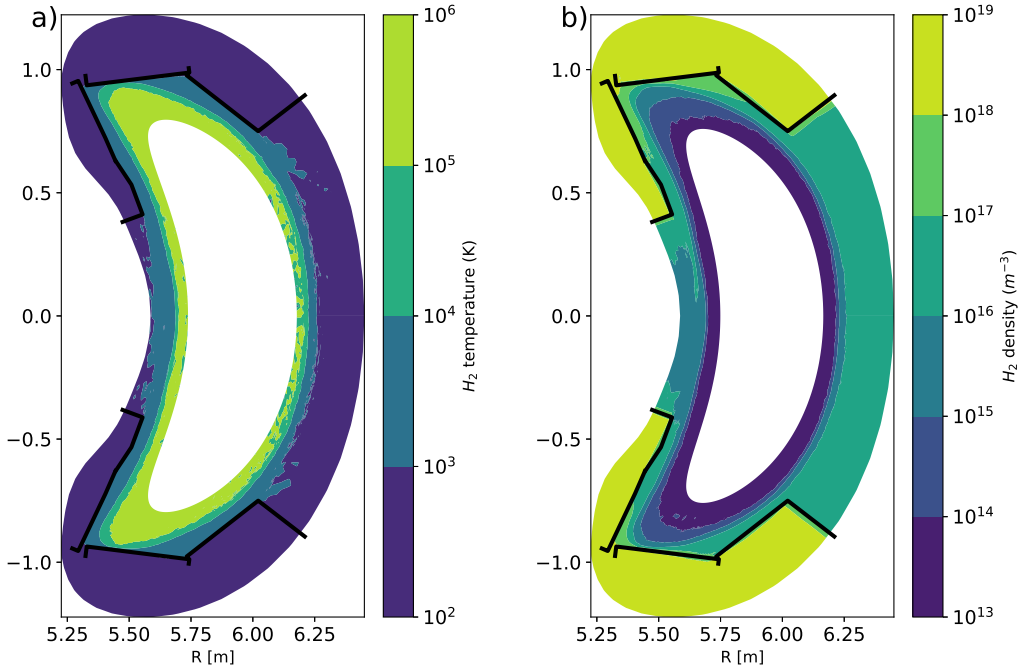

Figure 3.2.: Simulation of neutral gas properties in the bean-shaped cross-section of W7-X ($\phi = 0$) from EMC3-EIRENE at typical plasma parameters, overplottet with first wall structures in black. **a)**: Temperature. Cold neutrals outside the plasma are visible, core domain excluded. **b)**: H_2 molecular density. Distinct reservoirs are visible: *Inside the plasma*, only negligible particle densities are found, *surrounding the plasma* is a region of medium pressure and the *subdivertor* space shows much higher densities. This simulation is not intended for quantitative use, but meant to illustrate and motivate the different reservoirs. Molecule density was capped at $10 \cdot 10^{13}\,\mathrm{m}^{-3}$ excluding the noisy plasma core. The subdivertor geometry is not reproduced properly here, so no inference on subdivertor volume is possible from this plot. Reproduced from article I.

density $n_{\mathrm{e},l}$ measured an interferometer [53] and the sight line length l of about 1.33 m. The sight line length varies by a few cm with magnetic configuration and plasma pressure effects, which is a small uncertainty compared to the difficulties of exact impurity fraction determination.

The impurity content in W7-X is monitored be a number of diagnostics, most notably charge exchange recombination spectroscopy (CXRS) [54], soft-x-ray pulse height analysis (PHA) [55], ultraviolet overview spectroscopy (HEXOS) [56], Z_{eff} diagnostic [57] and the filterscopes [58].

3.1.5. Bound particles

Of all terms in equation (3.2) the bound reservoir in the wall is the least accessible for measurement. While post-mortem analysis of in-vessel components gives important insight into long-term effects integrated over the whole lifetime of a sample, short term measurements are feasible only with great effort on small samples. The latter can be achieved via a retractable manipulator arm exposing material samples to plasma contact, like it is currently prepared for W7-X [59].

For a higher time resolution and non-destructive investigation, inference of the wall reservoir N_{w} from all other quantities in equation (3.2) is necessary. Due to practical reasons, the relative change to a reference time t_0 is calculated as $N_{\mathrm{w}} - N_{\mathrm{w},0}$. If the beginning of a plasma pulse is used as reference, this allows easy assessment of the wall reservoir evolution during the plasma pulse.

The described approach accumulates all uncertainties in the measurement of aforementioned quantities in the wall reservoir and calls for a detailed treatment of these errors. This has not been done in detail, because many of the error sources are not well known. The total estimated error for the wall reservoir is around 40 % and mainly arises from the uncertainties in pressure measurement in the exhaust quantification. The overall findings of net retention and release are robust under this estimation. A more thorough error analysis will be conducted in the commissioning phase of the next operation phase.

3.1.6. Internal sources and sinks

The source and sink terms, $S_{+,a}$ and $S_{-,a}$, in equation (3.2) couple balance equations of different gas species, but can also involve previously solid material. Processes captured in these terms are nuclear fusion reactions with fuel burnup and helium ash production and chemical reactions. While the former does not

play a role in most fusion experiments, chemical reactions of hot plasma is not uncommon in magnetically confined fusion devices. The carbon tiles used in W7-X can react with impurities or hydrogen, e.g. to CO and hydrocarbons, and tungsten is known to catalyze ammonia formation [60]. Since this study presents a first gas balance for W7-X and concentrated on hydrogen as majority plasma species, these terms are only mentioned for completeness.

3.2. Typical reservoir sizes in Wendelstein 7-X

In balance equations, one usually finds two terms dominating over minor terms. For time-dependent equations this might change over time. Typical reservoir sizes and rates in W7-X OP 1.2 for hydrogen are given in table 3.1 and potential hydrogen retention in the carbon divertor and steel walls stand out as largest numbers.

An example is shown in figure 3.3, where the dominance of injected and removed particles can be observed.

The neutral inventory size naturally depends strongly on the pressure. The background pressure in between plasma pulses is sufficiently low to contribute only a negligible number of particles compared to the plasma molecular equivalent or the injected or removed particle number. During plasma, most of the gas content of the PV is ionized or bound in the wall and even the relatively high pressured volume below the divertor contributes only little to the absolute particle number. After the termination of the plasma pulse, the hot walls start outgassing and the whole plasma vessel is filled with released gas. This neutral reservoir contributes to the overall balance in a significant way, especially in short plasmas and with very hot wall components.

We can conclude that the role of pressure measurement for the gas balance is most important for exhaust quantification and neutral estimation in the immediate post-plasma phase.

3.3. Gas balance in other fusion experiments

The method of gas balance as presented here has been used at many fusion experiments to gain information about dynamic and static gas retention of different gas species. T. Loarer gave an excellent overview of gas balance in

Reservoir description	**typical size or rate (molecules)**
prefill	$3 \cdot 10^{20}$
maximum fueling from one valve	$1.7 \cdot 10^{21}\,\mathrm{s}^{-1}$
plasma particle content (at $1 \cdot 10^{20}$ electrons/m^2)	$9 \cdot 10^{20}$
neutral background pre-operation (at $1 \cdot 10^{-7}$ mbar)	$2 \cdot 10^{17}$
midplane neutral reservoir during plasma (at $3 \cdot 10^{-6}$ mbar)	$6.2 \cdot 10^{18}$
divertor neutral reservoir during plasma (at $1 \cdot 10^{-4}$ mbar)	$1.2 \cdot 10^{19}$
neutral reservoir during outgassing phase (at $1 \cdot 10^{-4}$ mbar)	$2.7 \cdot 10^{20}$
pumped H_2 OP1.2 (TMP only: $30\,\mathrm{m}^3/\mathrm{s}$) (at $1 \cdot 10^{-4}$ mbar)	$7 \cdot 10^{19}\,\mathrm{s}^{-1}$
pumped H_2 OP2 (TMP + cryo pump: $105\,\mathrm{m}^3/\mathrm{s}$) (at $1 \cdot 10^{-4}$ mbar)	$2.5 \cdot 10^{20}\,\mathrm{s}^{-1}$
H_2 surface and bulk retention in the carbon divertor	$1.7 \cdot 10^{24}$
H_2 surface retention in the strike line	$1 \cdot 10^{22}$
H_2 surface retention in steel	$7 \cdot 10^{23}$

Table 3.1.: Comparison of different typical reservoir sizes. All conversions assumed at $T = 300\,\mathrm{K}$ for Hydrogen. Table reproduced from article I, where the derivation of retention numbers is given.

major tokamaks in 2007 [19] with a focus on fuel retention, and many more specific studies used the tool, e.g. for DIII-D [61], ASDEX Upgrade [62, 63], LHD [64, 65], JET [66] and KSTAR [67].

Research focuses on tritium retention, as this will be of high interest for regulatory reasons, and uses deuterium or protium as proxy for tritium. Main findings in tokamaks are the unfitness of graphite first-wall components due to their strong hydrogen retention.

In low fueled experiments a near full recovery of particles was reported from AUG as well as JET, while at higher total gas injection a rollover to a net reten-

tion effect was observed.

3.4. Gas balance results at Wendelstein 7-X

Application of the presented method to the full particle content in W7-X requires a large set of measured data which is not available at this point. Main challenges are e.g. uncertainties in injection and removal rates by the NBI and He-beam system, limited partial-pressure measurement capabilities and the role of the complicated carbon balance [68].

The analysis of this work, presented in article I, is restricted to rather simple cases of purely ECRH heated hydrogen plasmas fueled from the main gas valve system. More complicated cases, such as investigation of gas mixtures (e.g. in He glow discharges), non-majority gases (e.g. nitrogen puffing experiments for divertor radiation studies), NBI experiments or experiments with He-beam or pellet fueling schemes require more detailed partial pressure measurement and a better understanding of the respective systems in terms of their influence on neutral balance, which has not been achieved yet.

Figure 3.3 shows the example of a gas balance in W7-X. The chosen program was the record duration plasma of 100 s length. Heated with 2 MW ECRH at a line-integrated density of $5 \cdot 10^{19}\,\mathrm{m}^{-2}$ and conducted in the *high iota* magnetic configuration it had its main PWI area on the *high iota* target plate of the divertor. The main gas fueling system was used in feedback mode to keep the line-integrated density constant. While initially much gas was needed to fuel the plasma, the fueling rate reduced constantly while plasma density and exhaust rate stayed constant over most of the pulse. At approximately 80 s into the pulse, a few seconds after external fueling rate ceased, the plasma density starts to rise linearly for the last 20 s until end-of-heating terminates the plasma at 100 s and the plasma particles neutralize.

The described phenomena are interpreted as a result of continuous power deposition on the inertially cooled divertor, which heats up significantly during the experiment and mobilizes particles bound in deep reservoirs in the graphite divertor material, e.g. water. The mobilized particles leave the divertor tiles as gas and are either ionized by the plasma, deposited on colder surfaces or pumped away. RGA measurements support the hypothesis of outgassing water. Oxygen from dissociated water is not observed, as it is chemically bound by the remaining boron layer on most plasma facing component (PFC)s. With

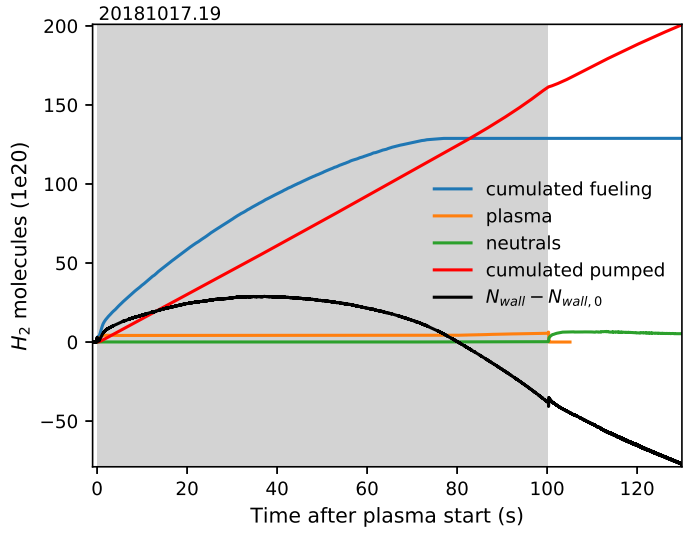

Figure 3.3.: Hydrogen gas balance of the W7-X OP 1 record length pulse (20181017.19) as example result of the presented method. Evolution of reservoirs over time, shaded area denotes plasma heating phase: total injected molecules (blue), total removed particles (red), plasma molecular equivalent (orange), free neutral gas content (green) and inferred wall reservoir change relative to start of heating (black). In total, $1.3 \cdot 10^{22}$ molecules are injected and $4 \cdot 10^{22}$ molecules are pumped away by the end of the outgassing phase. Adapted from article I.

increasing temperature and deeper penetration of heat into the bulk material, the wall particle source increases and replaces the feedback-controlled external fueling until it fully compensates the particle losses and the external fueling ceases. Further increase of the wall source then leads to the observed density increase towards the end of the pulse.

This experiment was preceded by a series of shorter pulses of increasing length. They observed replacement of external fueling by wall fueling as well, but at earlier times. This indicates a successive depletion of particle reservoirs in the divertor targets and can be understood as a conditioning effect on the divertor. Since this low heating power can only sustain a certain maximum plasma density, the preparatory programs are concluded to be necessary for the successful execution of the 100 s plasma pulse.

4
Conclusions

This Ph.D. thesis analyzes the gas balance for Wendelstein 7-X (W7-X) and its theoretical background as well as practical solutions for neutral pressure measurement in magnetic confinement fusion. The gas balance allows to infer a time evolution of the wall particle content and provides a tool to assess plasma experiments with respect to their effect on the bound reservoir. Knowledge of the bound reservoir is required for plasma density control and provides input to the experiment leader on the current wall conditions.

The major achievement of this thesis work is the first assessment of the hydrogen gas balance of the stellarator W7-X, presented in article I. We find a wide variety of operation regimes in varying wall conditions and significant release or retention of hydrogen, depending on the temperature evolution of the wall components as wall as time history of previous plasma pulses. It is shown here that the record-duration plasma pulse (100 s) only could be performed with controlled plasma density because the preceding pulses successively conditioned the divertor tiles.

Due to the significance of highly time-resolved total and partial pressure monitoring for the gas balance, two diagnostics were implemented and operated successfully.

In this work, the new diagnostic system (diagnostic RGA (DRGA)) was deployed on W7-X and first experimental results were obtained. In this first experimental validation of the DRGA concept completed with a gas sampling tube, time-resolved partial pressures of the constituents of the residual gas in W7-X were measured and is reported in article II. The diagnostic is considered a prototype for the ITER tokamak, the world's foremost fusion experiment currently under construction in Cadarache, France.

The third major achievement was the successful calibration and operation of enhanced hot cathode gauges in W7-X, the *crystal cathode pressure gauges* (CCPG). Article III reports on the successful calibration and operation of the CCPGs in W7-X, which proved to be a valuable tool for exhaust and plasma edge studies. The new fast calibration scheme of these reliable total pressure gauges presents a significant advancement over previous calibration modes and the ASDEX pressure gauge (APG) in use before.

Bibliography

[1] M. L. E. Oliphant, P. Harteck and Lord Rutherford. »Transmutation effects observed with heavy hydrogen«. In: *Proceedings of the Royal Society of London. Series A, Containing Papers of a Mathematical and Physical Character*, Vol. 144.853 (May 1934), pages 692–703. doi: 10.1098/rspa.1934.0077.

[2] V. D. Shafranov. »The initial period in the history of nuclear fusion research at the Kurchatov Institute«. In: *Physics-Uspekhi*, Vol. 44.8 (Aug. 2001), pages 835–843. doi: 10.1070/PU2001v044n08ABEH001068.

[3] J. D. Lawson. »Some Criteria for a Power Producing Thermonuclear Reactor«. In: *Proceedings of the Physical Society. Section B*, Vol. 70.1 (Jan. 1957), page 6. doi: 10.1088/0370-1301/70/1/303.

[4] L. A. Artsimovich. »Tokamak devices«. In: *Nuclear Fusion*, Vol. 12.2 (Mar. 1972), pages 215–252. doi: 10.1088/0029-5515/12/2/012.

[5] F. C. Schuller. »Disruptions in tokamaks«. In: *Plasma Physics and Controlled Fusion*, Vol. 37.11A (Nov. 1995), A135–A162. doi: 10.1088/0741-3335/37/11A/009.

[6] T. C. Luce. »Realizing steady-state tokamak operation for fusion energy«. In: *Physics of Plasmas*, Vol. 18.3 (Mar. 2011), page 030501. doi: 10.1063/1.3551571.

[7] L. Spitzer. »The Stellarator Concept«. In: *Physics of Fluids*, Vol. 1.1958 (1958), pages 253–264. doi: 10.1063/1.1705883.

[8] F. Wagner. »Stellarators and Optimised Stellarators«. In: *Fusion Technology*, Vol. 33.2T (Mar. 1998), pages 67–83. doi: 10.13182/FST98-A11946996.

[9] A. H. Boozer. »What is a stellarator?« In: *Physics of Plasmas*, Vol. 5.5 (May 1998), page 1647. doi: 10.1063/1.872833.

[10] JET team. »Fusion energy production from a deuterium-tritium plasma in the JET tokamak«. In: *Nuclear Fusion*, Vol. 32.2 (Feb. 1992), page 187. doi: 10.1088/0029-5515/32/2/I01.

[11] G. Haas and H.-S. Bosch. »In vessel pressure measurement in nuclear fusion experiments with ASDEX gauges«. In: *Vacuum*, Vol. 51.1 (Sept. 1998), pages 39–46. doi: 10.1016/s0042-207x(98)00131-6.

[12] M. E. Sawan and M. A. Abdou. »Physics and technology conditions for attaining tritium self-sufficiency for the DT fuel cycle«. In: *Fusion Engineering and Design*, Vol. 81.8-14 (Feb. 2006), pages 1131–1144. doi: 10.1016/j.fusengdes.2005.07.035.

[13] ASDEX team. »The H-Mode of ASDEX«. In: *Nuclear Fusion*, Vol. 29.11 (Nov. 1989), pages 1959–2040. doi: 10.1088/0029-5515/29/11/010.

[14] G. F. Matthews. »Plasma detachment from divertor targets and limiters«. In: *Journal of Nuclear Materials*, Vol. 220-222 (Apr. 1995), pages 104–116. doi: 10.1016/0022-3115(94)00450-1.

[15] C. R. Burnett et al. »The Divertor, a Device for Reducing the Impurity Level in a Stellarator«. In: *Physics of Fluids*, Vol. 1.5 (1958), pages 438–445. doi: 10.1063/1.1724361.

[16] L. Spitzer. »A Proposed Stellarator«. In: *US atomic energy commission report*, Vol. NYO-993 (PM-S-1) (July 1951). url: https://www.osti.gov/biblio/4285898.

[17] M. Keilhacker. »The ASDEX divertor tokamak«. In: *Nuclear Fusion*, Vol. 25.9 (Sept. 1985), pages 1045–1054. doi: 10.1088/0029-5515/25/9/008.

[18] F. Karger and K. Lackner. »Resonant helical divertor«. In: *Physics Letters A*, Vol. 61.6 (June 1977), pages 385–387. doi: 10.1016/0375-9601(77)90341-3.

[19] T. Loarer et al. »Gas balance and fuel retention in fusion devices«. In: *Nuclear Fusion*, Vol. 47.9 (Aug. 2007), pages 1112–1120. doi: 10.1088/0029-5515/47/9/007.

[20] H. Niemann et al. »Large wetted areas of divertor power loads at Wendelstein 7-X«. In: *Nuclear Fusion*, Vol. 60.8 (July 2020), page 084003. doi: 10.1088/1741-4326/ab937a.

[21] C. Beidler et al. »Physics and Engineering Design for Wendelstein VII-X«. In: *Fusion Science and Technology*, Vol. 17.1 (Jan. 1990), pages 148–168. doi: 10.13182/fst90-a29178.

[22] G. Grieger et al. »Physics Studies for Helical-Axis Advanced Stellarators: 12. Conference Proceedings«. In: *Plasma Physics and Controlled Nuclear Fusion Research 1988*. 1989, pages 369–387. url: https://inis.iaea.org/search/search.aspx?orig_q=RN:21008752.

[23] H. M. Smith et al. »Would the Wendelstein 7-X "record discharge" have been possible in other magnetic configurations?« In: *22nd International Stellarator and Heliotron Workshop 2019 (ISHW 2019)*. 2019. url: https://pure.mpg.de/pubman/faces/ViewItemOverviewPage.jsp?itemId=item_3168387.

[24] H. Renner et al. »Physical Aspects And Design of the Wendelstein 7-X Divertor«. In: *Fusion Science and Technology*, Vol. 46.2 (Sept. 2004), pages 318–326. doi: 10.13182/FST04-A570.

[25] T. S. Pedersen et al. »Key results from the first plasma operation phase and outlook for future performance in Wendelstein 7-X«. In: *Physics of Plasmas*, Vol. 24.5 (2017), page 055503. doi: 10.1063/1.4983629.

[26] T. S. Pedersen et al. »First divertor physics studies in Wendelstein 7-X«. In: *Nuclear Fusion*, Vol. 59.9 (July 2018), page 096014. doi: 10.1088/1741-4326/ab280f.

[27] J. Boscary et al. »Design and technological solutions for the plasma facing components of WENDELSTEIN 7-X«. In: *Fusion Engineering and Design*, Vol. 86.6-8 (Oct. 2011), pages 572–575. doi: 10.1016/j.fusengdes.2010.11.020.

[28] K. Heinola et al. »Long-term fuel retention in JET ITER-like wall«. In: *Physica Scripta*, Vol. 167 (Feb. 2016), page 014075. doi: 10.1088/0031-8949/t167/1/014075.

[29] U. Wenzel et al. »On the performance of ASDEX pressure gauges with cathodes of thoriated tungsten«. In: (in preparation).

[30] U. Wenzel et al. »An ionization pressure gauge with LaB6 emitter for long-term operation in strong magnetic fields«. In: *Review of Scientific Instruments*, Vol. 89.3 (Mar. 2018), page 033503. doi: 10.1063/1.5019765.

[31] F. Penning. »Die Glimmentladung bei niedrigem Druck zwischen koaxialen Zylindern in einem axialen Magnetfeld«. In: *Physica*, Vol. 3.9 (Nov. 1936), pages 873–894. doi: 10.1016/S0031-8914(36)80313-9.

[32] M. v. Pirani. »Selbszeigendes Vakuum-Messinstrument«. In: *Verhandlungen der Deutschen Physikalischen Gesellschaft*, Vol. 8.24 (30th Dec. 1906), pages 686–694. url: https://archive.org/details/verhandlungende00goog/page/n793/mode/2up.

[33] T. Kremeyer et al. »Wisconsin In Situ Penning (WISP) gauge: A versatile neutral pressure gauge to measure partial pressures in strong magnetic fields«. In: *Review of Scientific Instruments*, Vol. 91.4 (Apr. 2020), page 043504. doi: 10.1063/1.5125863.

[34] W. Paul and H. Steinwedel. »Apparatus for separating charged particles of different specific charges«. US Patent 2,939,952. June 1960. url: https://pdfpiw.uspto.gov/.piw?PageNum=0&docid=02939952.

[35] H. Sommer, H. A. Thomas and J. A. Hipple. »The measurement of e/M by cyclotron resonance«. In: *Physical Review*, Vol. 82.5 (June 1951), pages 697–702. doi: 10.1103/physrev.82.697.

[36] W. Paul and H. Steinwedel. »Ein neues Massenspektrometer ohne Magnetfeld«. In: *Zeitschrift für Naturforschung A*, Vol. 8.7 (Jan. 1953), pages 448–450. doi: 10.1515/zna-1953-0710.

[37] É. Mathieu. »Mémoire sur le mouvement vibratoire d'une membrane de forme elliptique.« In: *Journal de mathématiques pures et appliquées*, Vol. 13 (1868), pages 137–203. url: http://sites.mathdoc.fr/JMPA/PDF/JMPA_1868_2_13_A8_0.pdf.

[38] R. Nachtrieb, B. LaBombard and E. Thomas. »Omegatron ion mass spectrometer for the Alcator C-mod tokamak«. In: *Review of Scientific Instruments*, Vol. 71.11 (2000), pages 4107–4118. doi: 10.1063/1.1311942.

[39] R. E. March. »An Introduction to Quadrupole Ion Trap Mass Spectrometry«. In: *Journal of Mass Spectrometry*, Vol. 32.4 (Apr. 1997), pages 351–369. DOI: 10.1002/(sici)1096-9888(199704)32:4<351::aid-jms512>3.0.co;2-y.

[40] C. C. Klepper et al. »Design of a diagnostic residual gas analyzer for the ITER divertor«. In: *Fusion Engineering and Design*, Vol. 96 (Oct. 2015), pages 803–807. DOI: 10.1016/j.fusengdes.2015.04.053.

[41] T. R. Younkin et al. »Description of the prototype diagnostic residual gas analyzer for ITER«. In: *Review of Scientific Instruments*, Vol. 85.11 (Nov. 2014), 11E816. DOI: 10.1063/1.4892157.

[42] D. L. Hillis et al. »Deuterium-tritium concentration measurements in the divertor of a tokamak via a modified Penning gauge«. In: *Fusion engineering and design*, Vol. 34 (Mar. 1997), pages 347–351. DOI: 10.1016/s0920-3796(96)00653-9.

[43] J. Schacht et al. »The gas supply and gas inlet control systems of the fusion experiment Wendelstein 7-X«. In: *Fusion Engineering and Design*, Vol. 129 (2018), pages 6–11. DOI: 10.1016/j.fusengdes.2018.02.036.

[44] T. Barbui et al. »The He/Ne beam diagnostic for line-ratio spectroscopy in the island divertor of Wendelstein 7-X«. In: *Journal of Instrumentation*, Vol. 14.07 (July 2019), page C07014. DOI: 10.1088/1748-0221/14/07/c07014.

[45] S. Zoletnik et al. »Advanced neutral alkali beam diagnostics for applications in fusion research«. In: *Review of Scientific Instruments*, Vol. 89.10 (Oct. 2018), page 10D107. DOI: 10.1063/1.5039309.

[46] K. Tang. *Design of the gas-puff imaging diagnostic for Wendelstein 7-X*. Bachelor's Thesis. MIT, 2019. URL: https://hdl.handle.net/1721.1/123364.

[47] P. McNeely et al. »Current status of the neutral beam heating system of W7-X«. In: *Fusion Engineering and Design*, Vol. 88.6-8 (Oct. 2013), pages 1034–1037. DOI: 10.1016/j.fusengdes.2013.03.006.

[48] M. Dibon et al. »Blower Gun pellet injection system for W7-X«. In: *Fusion Engineering and Design*, Vol. 98 (2015), pages 1759–1762. DOI: 10.1016/j.fusengdes.2015.01.050.

[49] T. E. Gebhart et al. »Design and Modeling of Vacuum Pumping for Steady-State Pellet Fueling Systems«. In: *Fusion Science and Technology*, Vol. 75.2 (Dec. 2018), pages 89–97. doi: 10.1080/15361055.2018.1541399.

[50] R. Bussiahn et al. »Tracer-Encapsulated Solid Pellet (TESPEL) injection system for Wendelstein 7-X«. In: *Review of Scientific Instruments*, Vol. 89.10 (Oct. 2018), 10K112. doi: 10.1063/1.5038844.

[51] O. B. Malyshev. »Characterisation of a turbo-molecular pumps by a minimum of parameters«. In: *Vacuum*, Vol. 81.6 (Feb. 2007), pages 752–758. doi: 10.1016/j.vacuum.2005.11.055.

[52] Y. Feng et al. »A 3D Monte Carlo code for plasma transport in island divertors«. In: *Journal of Nuclear Materials*, Vol. 241-243 (Feb. 1997), pages 930–934. doi: 10.1016/S0022-3115(97)80168-7.

[53] K. J. Brunner et al. »Real-time dispersion interferometry for density feedback in fusion devices«. In: *Journal of Instrumentation*, Vol. 13.09 (Sept. 2018), P09002. doi: 10.1088/1748-0221/13/09/p09002.

[54] O. P. Ford et al. »Charge exchange recombination spectroscopy at Wendelstein 7-X«. In: *Review of Scientific Instruments*, Vol. 91.2 (Feb. 2020), page 023507. doi: 10.1063/1.5132936.

[55] M. Kubkowska et al. »First results from the soft X-ray pulse height analysis system on Wendelstein 7-X stellarator«. In: *Fusion Engineering and Design*, Vol. 136 (Nov. 2018), pages 58–62. doi: 10.1016/j.fusengdes.2017.12.024.

[56] W. Biel et al. »High efficiency extreme ultraviolet overview spectrometer: Construction and laboratory testing«. In: *Review of scientific instruments*, Vol. 77.10 (Oct. 2006), 10F305. doi: 10.1063/1.2221659.

[57] A. Pavone et al. »Measurements of visible bremsstrahlung and automatic Bayesian inference of the effective plasma charge Zeff at W7-X«. In: *Journal of Instrumentation*, Vol. 14.10 (Oct. 2019), page C10003. doi: 10.1088/1748-0221/14/10/C10003.

[58] R. J. Colchin et al. »The filterscope«. In: *Review of scientific instruments*, Vol. 74.3 (Mar. 2003), pages 2068–2070. doi: 10.1063/1.1537038.

[59] M. Hubeny et al. »Diagnostic setup for the divertor manipulator at Wendelstein 7-X«. In: *Nuclear Materials and Energy*, Vol. 18 (Jan. 2019), pages 77–81. doi: 10.1016/j.nme.2018.11.028.

[60] J. H. van Helden et al. »Detailed study of the plasma-activated catalytic generation of ammonia in N2-H2 plasmas«. In: *Journal of Applied Physics*, Vol. 101.4 (Feb. 2007), page 043305. doi: 10.1063/1.2645828.

[61] S. L. Allen et al. »Particle Control and Transport Experiments in the DIII-D Tokamak with Graphite Walls«. In: *Proc. 23rd Fusion Energy Conference*. 2010, pages 11–16. url: https://fusion.gat.com/pubs-ext/IAEA10/A26897.pdf.

[62] V. Rohde et al. »Dynamic and static deuterium inventory in ASDEX Upgrade with tungsten first wall«. In: *Nuclear fusion*, Vol. 49.8 (July 2009), page 085031. doi: 10.1088/0029-5515/49/8/085031.

[63] V. Rohde et al. »Wall retention of deuterium and gaseous impurities in all tungsten ASDEX Upgrade«. In: *Plasma Physics and Controlled Fusion*, Vol. 51.12 (2009), page 124033. doi: 10.1088/0741-3335/51/12/124033.

[64] Y. Nakamura et al. »Particle balance in NBI heated long pulse discharges on LHD«. In: *Journal of nuclear materials*, Vol. 290 (Mar. 2001), pages 1040–1044. doi: 10.1016/S0022-3115(00)00463-3.

[65] G. Motojima et al. »Global helium particle balance in LHD«. In: *Journal of Nuclear Materials*, Vol. 463 (Aug. 2015), pages 1080–1083. doi: 10.1016/j.jnucmat.2014.10.081.

[66] M. Oberkofler et al. »First nitrogen-seeding experiments in JET with the ITER-like Wall«. In: *Journal of Nuclear Materials*, Vol. 438 (July 2013), S258–S261. doi: 10.1016/j.jnucmat.2013.01.041.

[67] Y. Yu et al. »First comprehensive particle balance study in KSTAR with a full graphite first wall and diverted plasmas«. In: *Plasma Physics and Controlled Fusion*, Vol. 54.10 (Aug. 2012), page 105006. doi: 10.1088/0741-3335/54/10/105006.

[68] M. Mayer et al. »Material erosion and deposition on the divertor of W7-X«. In: *Physica Scripta*, Vol. T171 (Jan. 2020), page 014035. doi: 10.1088/1402-4896/ab4b8c.

Acronyms

APG ASDEX pressure gauge
ASDEX *axialsymmetrisches Divertor-Experiment*
AUG ASDEX Upgrade

CFC carbon fibre reinforced carbon
CXRS charge exchange recombination spectroscopy

DEMO Demonstration Power Plant
DRGA diagnostic RGA

ECRH electron cyclotron resonance heating

HEXOS ultraviolet overview spectroscopy

IPP Max-Planck Institute for Plasma Physics
ITER *latin*: the way, first fusion reactor
ITMS ion-trap mass spectrometer

JET Joint European Torus

LaB_6 lanthanum hexaboride

LHD large helical device
LCFS last closed flux surface

NBI neutral beam injection

OGA optical gas analyzer
OP operation phase

P-DRGA prototype diagnostic RGA
PFC plasma facing component
PHA soft-x-ray pulse height analysis
PV plasma vessel
PWI plasma-wall interaction

QMS quadrupole mass spectrometer

RGA residual gas analyzer

SOL scrape-off layer

TMP turbomolecular pump

UHV ultra-high vacuum

W7-X Wendelstein 7-X
WISP Wisconsin In-Situ Penning

List of Figures

A
Thesis Articles

Authors contributions:

Article I

»The evolution of the bound particle reservoir in Wendelstein 7-X and itsinfluence on plasma control«

G. Schlisio, U. Wenzel, D. Naujoks, T. S. Pedersen, H. Grote, V. R. Winters, H.Niemann, M. Mulsow, M. Krychowiak, P. Drewelow, Y. Gao, M. Jakubowski, A. Puig Sitjes, H. Laqua, J. Knauer, K. J. Brunner and W7-X team

submitted to Nuclear fusion, (2020),

G. Schlisio conducted the analysis, wrote the manuscript, and is part of the total and partial pressure measurement teams. U. Wenzel has advised during analysis, providing guidance and leads the total pressure measurement team. D. Naujoks has contributed with discussions regarding PWI. T.S. Pedersen has advised during analysis, providing guidance. H. Grote is the responsible person for the W7-X vacuum system and has helped with discussion and advice. V. Winters has contributed EMC3-Eirene simulations and helped in drawing conclusions from those. M. Mulsow is member of the total pressure measurement team responsible for the acquired data. M. Krychowiak is the responsible person for the divertor gas inlet system and responsible for the provided data. H. Niemann is part of the IR team and helped with discussion and technical advice. P. Drewelow, Y. Gao, M. Jakubowski, A. Puig Sitjes are the IR diagnostic group and responsible for divertor surface temperature measurements. H. Laqua is

responsible for the ECRH data. J. Knauer, K.J. Brunner provided the interferometry data. The final editing involved all co-authors (G. Schlisio, U. Wenzel, D. Naujoks, T.S. Pedersen, H. Grote, V.R. Winters, H. Niemann, M. Mulsow, M. Krychowiak, P. Drewelow, Y. Gao, M. Jakubowski, A. Puig Sitjes, H. Laqua, J. Knauer, K.J. Brunner).

The W7-X Team operated the W7-X stellarator experiment, conducted the plasma experiments, provided a platform for data acquisition, storage, evaluation, discussion of results and publication.

Article II

»First results from the implementation of the ITER diagnostic residual gas analyzer prototype at Wendelstein 7-X«

G. Schlisio, C. C. Klepper, J. H. Harris, T. M. Biewer, V. R. Winters, U. Wenzel, P. Kornejew, H. Laqua, M. Krychowiak and W7-X team

Review of Scientific Instruments, Vol. 90.9 (Sept. 2019), doi: 10.1063/1.5098125

G. Schlisio wrote the manuscript, planned and conducted operation and is responsible for the P-DRGA system at W7-X and its data. C.C. Klepper invented the DRGA system and built the original hardware together with T.M. Biewer, and advised during integration. J.H. Harris coordinated the collaboration, assisted with advise and paved the administrative road by convincing many. U. Wenzel assisted during W7-X integration and during the collaboration. V.R. Winters, P. Kornejew and M. Krychowiak are part of the spectroscopy team and are responsible for the data acquisition of the OGA. H. Laqua is the responsible person for the ECRH system and responsible for ECRH data. The final editing involved all co-authors (G. Schlisio, C.C. Klepper, J.H. Harris, T.M. Biewer, V.R. Winters, U. Wenzel, P. Kornejew, H. Laqua, M. Krychowiak).

The W7-X Team operated the W7-X stellarator experiment, conducted the plasma experiments, provided a platform for data acquisition, storage, evaluation, discussion of results and publication.

Article III

»Performance of new crystal cathode pressure gauges for long-pulse operation in the Wendelstein 7-X stellarator«

U. Wenzel, G. Schlisio, M. Mulsow, T. S. Pedersen, M. Singer, M. Marquardt, D. Pilopp and N. Rüter

Review of Scientific Instruments, Vol. 90.12 (Dec. 2019), doi: 10.1063/1.5121203

U. Wenzel wrote the manuscript, lead, planned and conducted operation. G. Schlisio conducted operation, planned, performed and evaluated the calibration. M. Mulsow assisted in operation, T.S. Pedersen supervised the operation preparation. M. Singer, M. Marquardt, D. Pilopp, and N. Rüter are members of the manometer team. The final editing involved all co-authors (U. Wenzel, G. Schlisio, M. Mulsow, T.S. Pedersen, M. Singer, M. Marquardt, D. Pilopp, and N. Rüter).

Confirmed by Supervisor,
Greifswald, 30.09.2020

Prof. Dr. Thomas Sunn Pedersen

Confirmed by doctoral candidate,

Greifswald, 30.09.2020

Georg Schlisio

A.1. Article I

»The evolution of the bound particle reservoir in Wendelstein 7-X and itsinfluence on plasma control«
G. Schlisio, U. Wenzel, D. Naujoks, T. S. Pedersen, H. Grote, V. R. Winters, H.Niemann, M. Mulsow, M. Krychowiak, P. Drewelow, Y. Gao, M. Jakubowski, A. Puig Sitjes, H. Laqua, J. Knauer, K. J. Brunner and W7-X team
submitted to Nuclear fusion, (2020),

nuclear fusion
IAEA

PAPER

The evolution of the bound particle reservoir in Wendelstein 7-X and its influence on plasma control

To cite this article: G. Schlisio *et al* 2021 *Nucl. Fusion* **61** 036031

IOP Publishing | International Atomic Energy Agency Nuclear Fusion

Nucl. Fusion **61** (2021) 036031 (10pp) https://doi.org/10.1088/1741-4326/abd63f

The evolution of the bound particle reservoir in Wendelstein 7-X and its influence on plasma control

G. Schlisio*, U. Wenzel, D. Naujoks, T.S. Pedersen, H. Grote, V.R. Winters, H. Niemann, M. Mulsow, M. Krychowiak, P. Drewelow, Y. Gao, M. Jakubowski, A. Puig Sitjes, H. Laqua, J. Knauer, K.J. Brunner and the W7-X team[a]

Max-Planck-Institut für Plasmaphysik, Wendelsteinstraße 1, 17491 Greifswald, Germany

E-mail: georg.schlisio@ipp.mpg.de

Received 18 September 2020, revised 7 December 2020
Accepted for publication 23 December 2020
Published 17 February 2021

Abstract

The investigation of fuel retention in fusion experiments is important in view of plasma density control as well as tritium inventory for future fusion reactors. We present a first gas balance of the stellarator Wendelstein 7-X with its inertially cooled graphite divertor. The gas balance is used to estimate the wall inventory and it is found that the wall plays an important and dynamic role, absorbing or releasing particles depending on the plasma conditions. Several different scenarios are presented and the effect of fueling and heating on the wall inventory is assessed. We find that the record duration plasma experiment of 100 s required previous shorter plasmas to be successfully conducted.

Keywords: magnetic confinement fusion, Wendelstein 7-X, stellarator, gas balance

(Some figures may appear in colour only in the online journal)

1. Introduction

Future fusion reactors face a number of yet unsolved problems, such as power and particle exhaust, both related to the boundary of the plasma. The interaction between energetic plasma particles and the wall leads to particles being retained and released on the walls. This results in a coupling of plasma and wall in terms of particles, which in turn influences core particle content and has the potential to degrade density control. For reactor-like steady-state fusion plasmas, e.g. ITER, this has to be solved by a net-zero particle flux between plasma and surrounding wall [1].

Wendelstein 7-X (W7-X) is an optimized modular stellarator [2] designed for steady-state operation with parameters approaching those of a reactor for up to 30 min of continuous plasma and as such a promising test bed for these problems. W7-X is outfitted with carbon tiles on the heat shields and divertors and cooled stainless steel panels in low loaded areas [3]. All these plasma facing surfaces will be referred to as *first wall* in this treatment.

W7-X was in first commissioning operation (OP1.1) in 2015 with a graphite limiter [4]. In its second operation phase, OP1.2 in 2017 and 2018, it was operated with an inertially cooled graphite divertor and an extended set of diagnostics [5]. Currently 10 water-cooled carbon-fiber-composite divertors are being installed and will be commissioned and operated in the next campaigns, here collectively referred to as operation phase 2 (OP2). The island divertor in W7-X is toroidally varying and segmented, intersecting magnetic islands in each module.

In this paper we present an analysis of the evolution of the wall particle reservoir of W7-X as found with the inertially cooled divertor in OP1.2 in attached plasmas. The wall reservoir is obtained from a gas balance as a balance of injected and removed particles.

* Author to whom any correspondence should be addressed.
[a] See Klinger *et al* 2019 (https://doi.org/10.1088/1741-4326/ab03a7) for the W7-X team.

Gas balances have been calculated for most major fusion experiments, such as DIII-D [6], ASDEX Upgrade [7, 8], LHD [9, 10], JET [11] and KSTAR [12]. Significant hydrogen retention is commonly found in carbon machines [13] and frequently attributed to amorphous carbon layers (so-called a:CH layers) [14] as well as implantation, but net outgassing scenarios are found as well.

Section 2 introduces the basic concepts and methodology and deals with the assumptions necessary. In section 3 a simple W7-X plasma is introduced and the results are discussed. In section 4 a sequence of two plasmas and the influence of plasma conditions are investigated. Section 5 explains the gas balance of the way to the record duration plasma in OP1.2b.

2. Concepts, methodology, and assumptions

In a reactor inventory accounting will be of high importance when regulatory rules require a close monitoring of radioactive material, especially tritium. Common fusion experiments are not well equipped for detailed accounting and balancing, but existing diagnostics can be used to augment a 0D model. The assumption of a simple continuity equation balancing cumulated injection rate $\int \dot{N}_{\mathrm{in}}$ and exhaust rate $\int \dot{N}_{\mathrm{out}}$ assumes no particles being generated or lost inside the experiment and is a good first-order approximation. The particle content can now be split up into different reservoirs: free neutral particles N_{n}, plasma molecular equivalent N_{p} and bound particles N_{w} bound in the wall. A visual representation is given in figure 1. All reservoirs except the bound reservoir start at zero or close to zero at the beginning of a plasma pulse, and since analysis is done pulse by pulse, we introduce an offset $N_{\mathrm{w},0}$ representing the unknown wall content at heating start.

$$\int_{t_0}^{t} \dot{N}_{\mathrm{in}} - \int_{t_0}^{t} \dot{N}_{\mathrm{out}} = N_{\mathrm{n}} + N_{\mathrm{p}} + N_{\mathrm{w}} - N_{\mathrm{w},0}. \qquad (1)$$

Particles are counted in units of their chemically stable state, e.g. molecules. In W7-X the main gas species is hydrogen, while especially in the beginning of the campaign helium was used for conditioning. All investigated experiments in this study were conducted with hydrogen.

The assumption of a continuity equation as stable particles with no chemical change has to be relaxed for plasma chemistry as well as fuel burnup and He-ash formation in a reactor. That leads to a coupling term between the balances for different species. One example is the carbon chemistry on the large carbon surface of the first wall, carbohydrates as well as carbon oxides can be regularly observed in the exhaust gas in small quantities, e.g. by means of a residual gas analyser (RGA) [15]. With increasing tungsten surface [16] and continued nitrogen seeding [17] ammonia formation [18] could become a noticeable phenomenon in W7-X as well. This is neglected here, since it does not play a role in W7-X at least for hydrogen as majority plasma species investigated here.

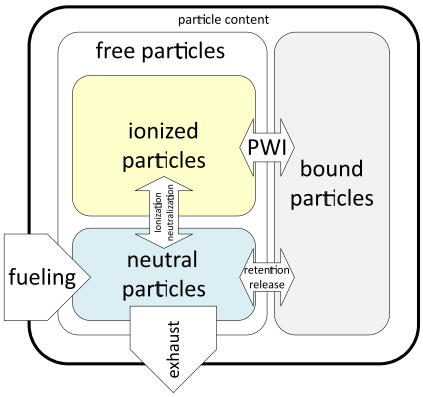

Figure 1. Schematic view of the reservoir model. The outer contour symbolizes the plasma vessel, subdivision of the particle content according to equation (1). Arrows indicate migration between reservoirs and are annotated with the main mechanisms. The role of neutral beam injection (NBI) is left out for simplicity.

Not all of the parameters in equation (1) are easily accessible and for some only rough estimates exist. This requires making some assumptions or estimations, discussed below.

2.1. Plasma molecular equivalent N_{p}

The estimation of plasma molecular equivalent is retrieved from the line integrated density measurement and geometric factors for hydrogen as

$$N_{\mathrm{p}} = \frac{1}{2}\frac{n_{\mathrm{e}} V_{\mathrm{p}}}{l} \cdot \left(1 - \sum_{\mathrm{i}} f_{\mathrm{i}} \cdot Z_{\mathrm{i}}\right) \qquad (2)$$

with the line-integrated density n_{e}, the sight line length l, the plasma volume V_{p} and the impurity fraction f_{i} and atomic number Z_{i}. The line-integrated density is measured with an interferometer [19] with a sight line of 1.33 m in plasma. This length varies with magnetic configuration and plasma beta below 4 % and is assumed constant.

The factor $\left(1 - \sum_{\mathrm{i}} f_{\mathrm{i}} \cdot Z_{\mathrm{i}}\right)$ corrects the electron density for the additional electrons from impurities to obtain the number of hydrogen ions. Assuming an example case of an impurity fraction f_{i} of 2% carbon and 1% oxygen in hydrogen, neglecting further possible impurities and assuming complete ionization of all impurities yields a correction factor of 0.8. This scenario is an upper estimate for W7-X OP1.2b post boronization, and the effect on the following analysis is small, so we assume this to be constant at the stated levels. Impurity content is W7-X is monitored with a number of diagnostics, such as charge exchange recombination spectroscopy [20], soft-x-ray pulse height analysis [21], ultraviolet overview spectroscopy [22] and Z_{eff} diagnostic [23].

The plasma volume V_{p} of W7-X is about 28 m^3 and changes only little in the type of experiment investigated here. We assume that only a negligible amount of ionized particles exists outside of this volume. Since we account for molecules in all other reservoirs, the obtained atom number has to be converted

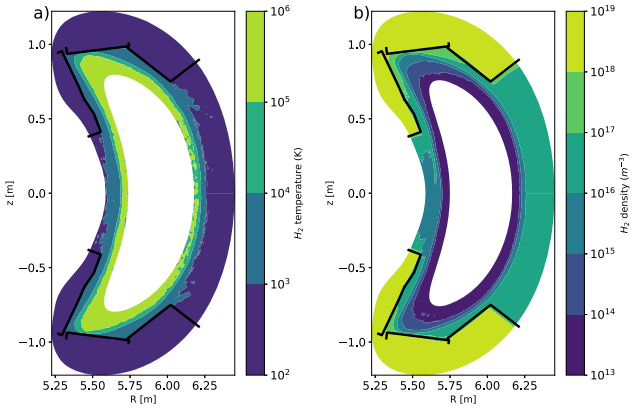

Figure 2. Simulation of neutral gas properties in the bean-shaped cross-section of W7-X ($\phi = 0$) from EMC3-EIRENE, overplottet with first wall structures in black. Simulated plasma parameters: $P_{\mathrm{ECRH}} = 4.5$ MW, $D = 1$ m^2 s^{-1}, $\chi = 3 \cdot D$, $n_{\mathrm{e,s}} = 1 \times 10^{19}$ m^{-3}, EIM magnetic configuration without error field correction. (*a*) Temperature. Cold neutrals outside the plasma are visible, core domain excluded. (*b*) H_2 molecular density. Distinct reservoirs are visible: *inside the plasma*, only negligible particle densities are found, *surrounding the plasma* is a region of medium pressure and the *subdivertor* space shows much higher densities. This simulation is not intended for quantitative use, but meant to illustrate and motivate the different reservoirs. Molecule density was capped at 10×10^{13} m^{-3} excluding the noisy plasma core. The subdivertor geometry is not reproduced properly here, so no inference on subdivertor volume is possible from this plot.

to molecules by dividing by the number of atoms per molecule, which is 2 for hydrogen.

2.2. Neutral particle content N_{n}

Neutral particle content N_{n} is determined by pressure measurement, the ideal gas law, and temperature and geometric assumptions:

$$N_{\mathrm{n}} = \frac{pV_{\mathrm{n}}}{k_{\mathrm{B}}T} \tag{3}$$

with the pressure p, the neutral volume V_{n}, the Boltzmann constant k_{B} and the gas temperature T.

The total plasma vessel volume is about 110 m^3, but does not always represent the neutral volume. During plasma operation, it is reduced by the plasma volume, where due to high plasma temperatures and densities neutrals are ionized within short distance of flight. This is confirmed by H_α emission indicating ionization only in a thin boundary layer.

W7-X utilizes hot cathode ionization gauges suited for long-pulse operation [24], based on ASDEX gauges common in tokamaks [25], to measure in-vessel pressure with high time resolution. These are supplemented with a set of *in situ* Penning gauges [26] and low-sampled commercial Penning gauges for operational and long-term monitoring of vacuum conditions [27].

Due to the overall availability of measurements in quantities of volume times pressure (per unit time for fluxes), the ideal gas law is used to convert measurements to absolute particle numbers. While the ideal gas law is suitable for most gases at low pressures and temperatures far away from phase

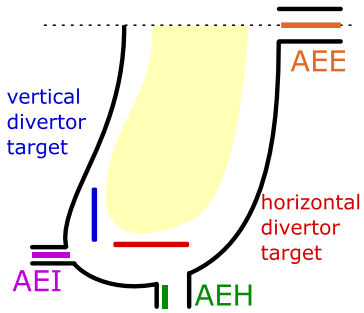

Figure 3. Schematic poloidal cut of W7-X to illustrate the total pressure gauge position. The plasma vessel shown in black, divertor target plates in blue (vertical) and red (horizontal), relevant measurement locations: AEE—outer midplane, AEH—pumping port, AEI—pumping gap. Central yellow shade symbolizes plasma region. Additional in-vessel components, such as baffles and heat shields, are not shown. The term *pumping gap* refers to the gap between horizontal and vertical divertor target, where neutral particles enter the sub-divertor space. The divertor has a segment used in *high iota* magnetic configuration, located in a toroidally shifted location. There, only a horizontal target and a pumping port measurement location exists. Adapted from [24].

boundaries, the neutral momentum distribution does not necessarily always follow a Maxwellian distribution required for the definition of a temperature. Nonetheless, lacking a practical alternative, and for reasons of simplicity, a Maxwellian distribution is assumed in this study.

The neutral temperature depends on the position of measurement and the plasma conditions, but is assumed to be constant over the whole evaluation domain at a value of 300 K unless stated otherwise. This is the cooling water temperature of the plasma vessel and thus the equilibrium temperature for gas after several collisions with the wall structure.

The validity of this assumption is confirmed by EMC3-EIRENE [28] simulations shown in figure 2 and can be explained by molecules forming on the wall and thus being thermalized there. In the simulations, atoms show a much higher temperature, which is understood as that they most likely originate from charge exchange and dissociation processes closer to the plasma. Due to their low absolute numbers they do not significantly contribute to the neutral pressure and can be neglected here.

During plasma operation, the pressure value inside and outside the divertor differ significantly. This is desired, as it greatly enhances particle exhaust while keeping the neutral influx into the main plasma low. On the other hand it requires to split the neutral volume into smaller parts, to get a more fine-grained estimation of neutral particle content. The sub-divertor space in OP1.2 was estimated from CAD with 5.12 m^3 for the low-iota part and 0.47 m^3 for the high-iota part, two segments of the divertor named for the configurations in which they are used. Their sub-divertor volumes are separated by closures and pumped through different ports. Pressure in the low-iota sub-divertor space is averaged between the measurement locations in the pumping port and in the pumping gap, in the high-iota part measured in the pumping port, and in the main chamber in the outer midplane. See figure 3 for a sketch of the gauge positions.

2.3. Removed particles

Pump performance is given as *pumping speed* S in units of volume per unit time. The exhaust rate Q is then given by the product of pumping speed S and pressure p, but again conversion to absolute particle numbers with the ideal gas law requires a gas temperature T:

$$Q = p \cdot S, \tag{4}$$

$$\dot{N}_{\mathrm{out}} = \frac{Q}{k_{\mathrm{B}} T}. \tag{5}$$

Since the main pumps at W7-X are located in receded positions due to low magnetic field acceptance, particles thermalize on the duct walls and can safely be assumed to have reached vessel temperature when being pumped.

In OP1, W7-X's main pumping system consists of 30 turbo-molecular pumps (TMPs) with a total pumping speed of 30 $\mathrm{m}^3\ \mathrm{s}^{-1}$ in hydrogen during OP1.2. With the new water-cooled divertor installed for OP2, pumping is enhanced by additional cryopumps with an approximate pumping speed of 75 $\mathrm{m}^3\ \mathrm{s}^{-1}$. With pressures below 1×10^{-3} mbar at the pump inlet, the pumping speed does not depend on the pressure and the exhaust rate is only determined by the inlet pressure.

Various diagnostic pumps exist, but contribute only negligible pumping speed and are often mounted in low-conductivity ducts further reducing the pump rate. They are not considered in this work.

Pumping of the NBI box is achieved by titanium getter pumps, which have a very high initial pumping speed degrading over time. The NBI box in connected to the W7-X plasma vessel with a large duct typically closed by a gate valve. The exact amount of pumped particles due to NBI operation is not known, because relevant gauges malfunctioned during operation. NBI experiments were excluded from this work, with one exception. Implications on the exception are discussed in section 5.

2.4. Injected particles

The particle sources comprise all external particle sources, such as gas valves, pellet injectors, diagnostic and heating particle beams as well as leaks. In W7-X there is a main fueling valve system [29], a divertor gas inlet system [30], a frozen pellet injector [31, 32], an impurity pellet injector [33], an impurity laser sputtering device [34] and a NBI system [35] as particle sources.

Only the main valve system, the divertor gas inlet, frozen pellet injector and NBI significantly contribute to the particle inventory and for simplicity reasons, only experiments utilizing the main fueling valves were selected for this investigation.

The valve system use piezo valves augmented with a Pirani flow sensor with an output in pressure times volume per unit time. They were calibrated for each gas with injections into the evacuated vessel. For the injected gas, vessel temperature is assumed. Their calibration was conducted in cold state and measured temperature of the fueling gas reservoirs were not significantly different from cooling water temperature.

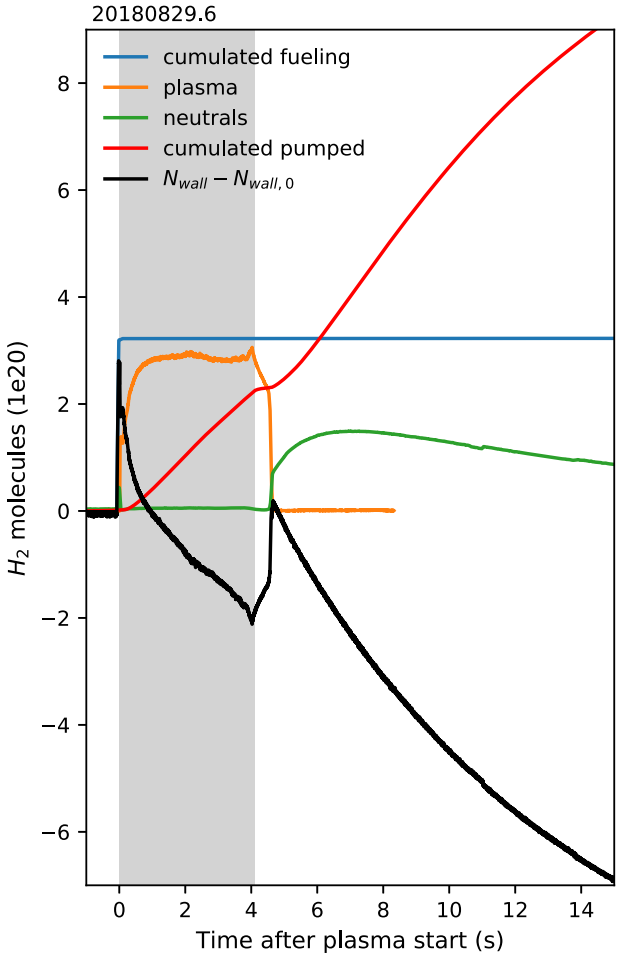

Figure 4. Gas balance of a basic exemplary plasma of OP1.2 with inertially cooled divertor after boronization. Cumulated fueling (blue) and exhaust (red) are shown along with the plasma molecular equivalent(orange) and the total neutral inventory (green). Net wall content (black) derived according to equation (1). Plasma heating phase with pure electron cyclotron heating (ECRH) is indicated with gray shade.

2.5. Bound particles

The bound particle reservoir is only indirectly quantifiable and is expected to be the largest. Depending on material properties and first-wall treatment, e.g. by wall conditioning, vacuum conditions, plasma wetting and heating, this reservoir can change significantly from discharge to discharge.

Unless the other reservoirs, its initial value is neither zero nor easily known, and consists of retained particles in the first wall material that can be mobilized under certain conditions. Graphite, the main material for plasma facing components in W7-X, is known to absorb large amounts of water. After boronization, oxygen is efficiently captured and water is released as hydrogen only. All scenarios discussed were conducted after boronization.

3. Basic plasma

A typical simple plasma in W7-X during OP1.2 was heated by pure ECRH, prefilled with a hydrogen gas puff of 3×10^{20}

Table 1. Comparison of typical reservoir sizes and particle rates. Free neutral inventory only reaches significant size during outgassing, (potential) bound reservoir exceeds all other by far. All conversions assumed at $T = 300$ K for molecular hydrogen.

Reservoir description	Typical size or rate(molecules)
Prefill	3×10^{20}
Maximum fueling from one valve[a]	1.7×10^{21} s^{-1}
Plasma particle content (at 1×10^{20} electrons/m^2)	9×10^{20}
Neutral background pre-operation (at 1×10^{-7} mbar)	2×10^{17}
Midplane neutral reservoir during plasma (at 3×10^{-6} mbar)	6.2×10^{18}
Divertor neutral reservoir during plasma (at 1×10^{-4} mbar)	1.2×10^{19}
Neutral reservoir during outgassing phase (at 1×10^{-4} mbar)	2.7×10^{20}
Pumped H_2 OP1.2 (TMP only: 30 m^3 s^{-1}) (at 1×10^{-4} mbar)	7×10^{19} s^{-1}
Projected pumping H_2 OP2 (TMP + cryo pump: 105 m^3 s^{-1}) (at 1×10^{-4} mbar)	2.5×10^{20} s^{-1}
H_2 surface and bulk retention in the carbon divertor[b]	1.8×10^{24}
H_2 surface retention in the strike line[c]	1×10^{22}
H_2 surface retention in steel	7×10^{23}

[a]Main gas valve system, 11 valves in total, individual values vary up to ±30%.
[b]Estimate, see text for details.
[c]See text for details.

molecules and continuously fueled from a mid-plane position via feedback control on a constant pre-set value of the line integrated density signal. More complex experiments were conducted, including frozen hydrogen pellet injection, impurity injection, NBI diagnostic and heating operation, density ramps and more, but are not addressed in this study for simplicity.

Figure 4 shows the gas balance of an example plasma of the W7-X inertially cooled divertor campaign (OP1.2) after boronization, conducted in the so-called *low iota* magnetic configuration. It is heated with 4 MW ECRH, fueled with hydrogen gas and reaches a line-integrated density of 3.5×10^{19} m^{-2} line integrated electron density which amounts to ca. 2.5×10^{20} molecules. The target line-integrated density of 2×10^{19} m^{-2} was continuously exceeded, so no additional fueling was applied during the whole duration of the 4 second program.

The plasma reservoir is fed by most of the gas prefill and quickly attaches to the wall, where the hot plasma forms a barrier for neutral particles from the strikeline (divertor plugging [36]). This results in a rise of the sub-divertor pressure and significant particle exhaust according to equation (5). By the end of heating, about as much gas was exhausted as was ionized, with the wall releasing a significant amount of particles as well.

At the end of heating the plasma quickly disappears and the recombinating particles form a significant neutral reservoir, which is however not as large as the plasma reservoir. Most of the particles remain in the wall, but start outgassing over a longer timespan. The lowest sub-divertor pressure is found at the beginning and end of plasma, when the plasma is not attached to the divertor target plates and neutrals are not efficiently compressed into the pumping gap. Within seconds after plasma decay, the outgassing fills the plasma vessel and allows efficient particle exhaust again.

The shown example yield a net outgassing of the wall of about 2×10^{20} particles by the end of heating but mobilized a much greater reservoir for the subsequent outgassing phase.

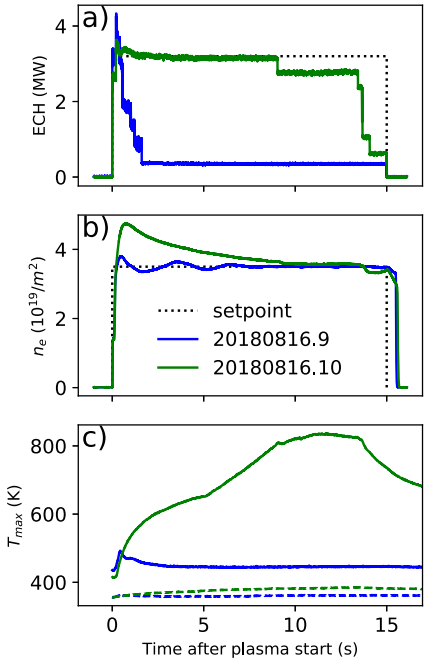

Figure 5. Comparison of two programs of similar density: (*a*) total heating power, (*b*) line-integrated density, (*c*) maximum divertor surface temperature (solid line) and baffle temperature (dashed line). Target density and heating power in black, 201 808 16.9 in blue, 201 808 16.10 in green. Despite great difference in heating power and deposited energy, the same density is reached.

With a total net outgassing of about 2.3×10^{21} particles this plasma can be classified as having a wall conditioning effect, removing about eight times as much as fueled.

3.1. Comparison of typical particle reservoir sizes

For illustration purpose, typical reservoir sizes at relevant parameters are given in table 1. One clearly sees that the neutral reservoirs during and before plasma do usually not contribute significantly to the plasma vessel particle content, either due to their small size in the case of the sub-divertor

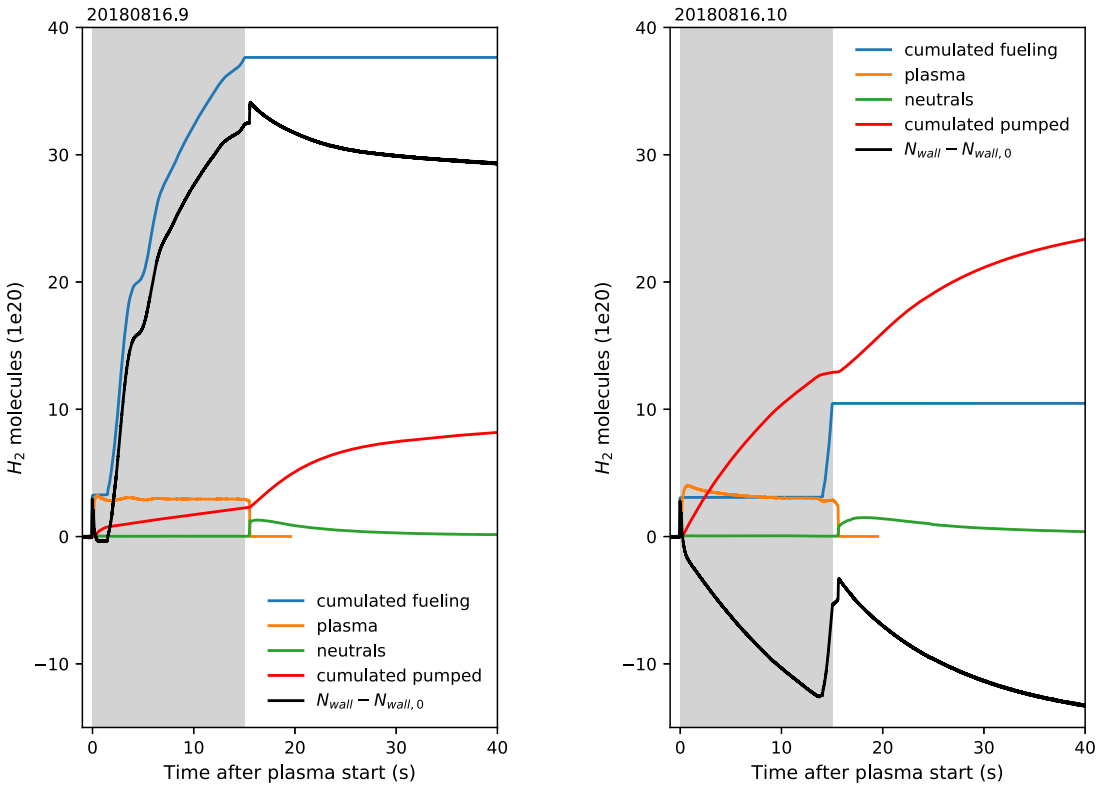

Figure 6. Comparison of two consecutive plasmas with very similar line-integrated density but low (left) and high (right) heating power and resulting divertor temperature. See figure 5 for plasma parameters. With the poorly heated divertor and heavy fueling, a huge wall reservoir builds up and the following plasma can sustain (apart from a prefill) entirely on gas from the wall. The fueling pulse at the very end of the second plasma is a reaction of the feedback control system to compensate the density loss originating from ECRH power drop and does not indicate wall depletion. Plotting details as in figure 4.

space or due to the low pressure. Only during the outgassing phase following successful divertor target heating, the neutral reservoir transiently becomes a major contribution in the balance.

The derived numbers partially match with the modeling from [27]. Good agreement is found in the fueling rate, and also for the exhaust rate, as a sub-divertor pressure of 1×10^{-3} mbar was assumed in that study.

Estimating the wall particle reservoir can only be done with rough estimations due to many unknowns.

Literature treatments distinguish between surface and bulk retention. The surface reservoir is given with 10^{18} cm^{-2} [37] in graphite, which amounts to about 2×10^{23} particles on the divertor (20 m^2) and 1×10^{24} particles for the total 105 m^2 of carbon surfaces in W7-X.

With the primary interaction surface on the divertor of an about 1 m^2 [38] (up to 1.5 m^2, but only about 0.5 m^2 in *high iota* configuration), 1×10^{22} particles in the surface area are directly accessible to the plasma.

Bulk retention in the divertor tiles with a thickness of 3 cm (graphite volume of about 0.6 m^3 and a weight of about 1076 kg) can be estimated to about 1.6×10^{24} particles (5 g/t [39]) of hydrogen. This value strongly depends on sample properties [40] but may serve as a rough estimate here.

Other carbon surfaces as the baffles (35 m^2) and heat shield (50 m^2) are not designed for direct plasma contact, but may receive varying loads mobilizing retained particles. These effects are neglected here for simplicity reasons.

The hydrogen surface retention in steel is about two orders of magnitude lower than in graphite (10^{16} cm^{-2}) [41, 42], and thus yields about 7×10^{23} particles for the 70 m^2 of steel first wall. Since no steel components are in direct contact with plasma, the bulk retention was not considered relevant.

Further steel surfaces are covered with carbon tiles or extend into the ports, but are not taken into account in this estimation.

In conclusion, the bound reservoirs potentially exceed the other reservoirs by orders of magnitude.

4. Short term wall reservoir

In this section, we will discuss the influence of short-term reservoirs which influence wall behavior of consecutive plasma experiments. The chosen examples were conducted in magnetic standard configuration, and had a programmed duration of 15 s, a target plasma line-integrated density of 3.5×10^{19} m^{-2} controlled by the fueling system and a nominal heating power of 3.2 MW ECRH. Due to gyrotron issues, the full heating power was not always applied, leading to notable effects on the gas balance.

Of the repetitions, two are of interest: one (201 808 16.9) ran for the full programmed duration at very low input

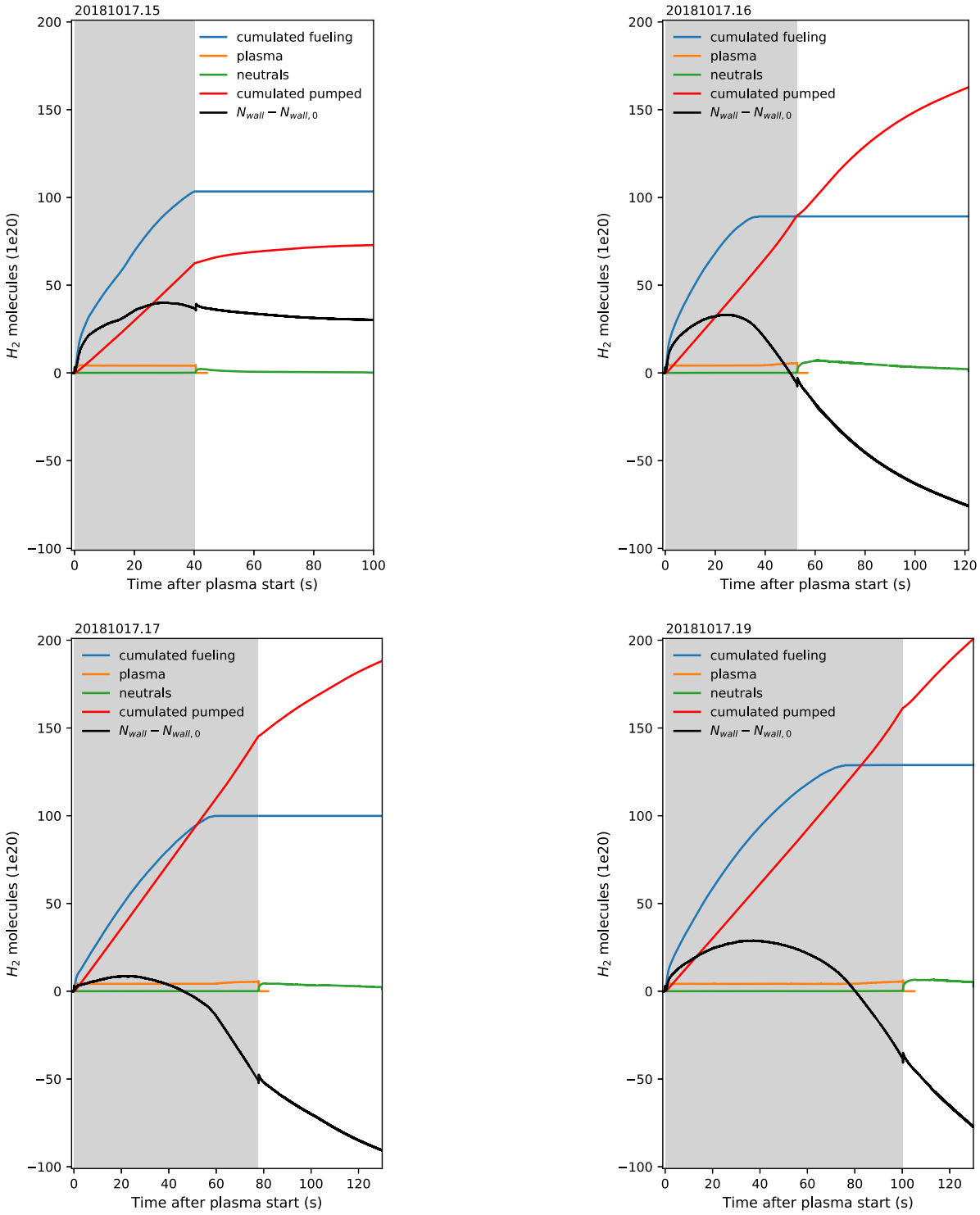

Figure 7. Gas balance of the four consecutive programs leading up to the 100 s plasma. Number 18 was a failed attempt with no injected power and has no significance for the reported balance and has thus been left out. The net wall reservoir increases at first, turns over and gets negative eventually, about when the external fueling ceases and plasma particle reservoir shows a slight increase as well. This indicates a strong wall source not fully compensated by the exhaust. Plot details as in figure 4.

power of 600 kW and reached target density only with very strong fueling. The following program (201 808 16.10) was heated with the foreseen heating power and did not require any fueling to even exceed target density. Figure 5 shows an overview of both programs. The low heating power in the first plasma resulted in low deposited power on the divertor, whose maximum surface temperature stabilized at 450 K. The baffle temperature remained nearly unchanged at 360 K.

The effect on wall behavior is shown in figure 6. Low wall recycling on cold walls leads to a massive retention of gas and required strong fueling in the first experiment. The wall retained 3×10^{21} additional particles, about ten times the plasma content molecular gas equivalent, after the plasma phase. During the outgassing phase, that reduced by more than a factor of three to 8×10^{20} during the outgassing phase, still loading the wall with more than double the entire plasma particle molecular equivalent.

On the following attempt with full heating, no external fueling besides the prefill was required. The attaching plasma heated the inertially cooled divertor plates, but left the baffle at nearly the same temperature as before. The heat-up mobilized more particles than needed to sustain plasma density leading to an overshoot. At the same time, high divertor pressures of 1×10^{-4} mbar allowed efficient exhaust. The fueling pulse toward the end tried to compensate the density decrease due to heating power loss and associated density drop. In total, the program removed about 1.3×10^{21} molecules from the wall by the end of heating, which is about double of the retained fuel from the previous plasma. Further outgassing removes more than that again, leading to a release of 3.7×10^{21} molecules from the wall.

This demonstrates the strong influence of the wall history over multiple pulses, where fuel can be retained and released very dynamically.

5. Long term reservoir

One of the highlights of the first divertor campaign of W7-X was the demonstration of a long stable plasma reaching a duration of 100 s at 2 MW of ECRH power and a line-integrated density of 5×10^{19} m^{-2}. Due to safety concerns with respect to the inertially cooled divertor, total injected power per experiment was restricted to 200 MJ, resulting in a rather low maximum heating power. The program was conducted in the *high iota* magnetic configuration, where the main plasma-wall-interaction point is located on the high-iota divertor target. That divertor target was only used in 14% of all experiments and did not experience as varied heat loads as the main divertor target. In result, deeper layers of the fine grain graphite were presumably not as well conditioned as other targets, and the long heating phase needed to be prepared by shorter experiments, even though this experiment was conducted toward the end of the campaign after long initial glow-discharge cleaning, multiple boronizations and an extended experiment program improving wall conditions.

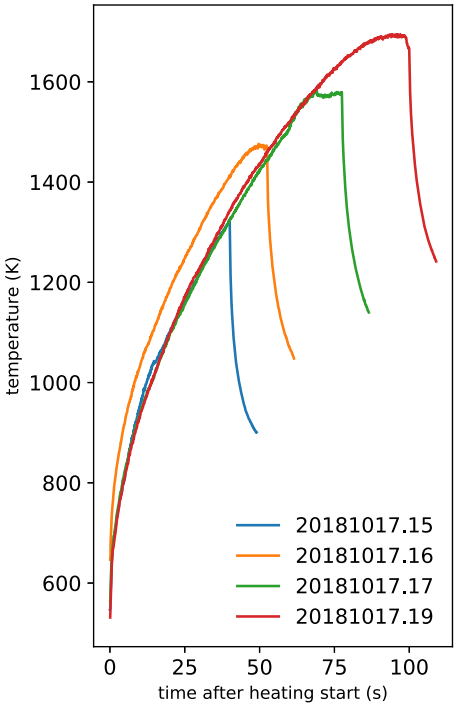

Figure 8. Divertor tile maximum surface temperature evolution of the same programs as in figure 7. All programs exhibit the same behavior, the slightly higher temperature in the second program is due to an elevated base temperature.

The 100 s plasma was prepared by a sequence of three similar plasmas with duration of about 40 s, 60 s and 80 s for operational reasons. The first experiment of the series lasted for 40 s and showed perfectly flat heating and density time traces. In the following longer experiments however, the density started to rise toward the end, indicating the presence of a strong particle source in the plasma vessel. Figure 7 shows the gas balance of all four consecutive programs. The onset of the density increases coincides with the end of auxiliary hydrogen gas fueling in density-feedback mode.

In the 40 s and 80 s plasma (201 810 17.15 and 201 810 17.17) NBI blips were introduced over a 10 s period, which required an opening of the NBI gate valve and resulted in additional particle removal. In the former, the NBI blips were introduced in the beginning, in the latter near the end. The particle input through the blips is minimal and is not considered here, the particle removal is higher but quantitatively unknown due to a lack in diagnostic. This introduces a perturbation on the removed particles, which does not change the overall picture and is thus not taken into account.

The surface temperature evolution of the divertor plates shown in figure 8 exhibits very similar heat-up for all pulses until the termination of plasma heating, plasma decay and subsequent inertial cooling of the divertor plates. A shorter cool-down phase before the second pulse resulting in an elevated base temperature of the divertor graphite tiles explains the moderately higher temperatures in the second pulse (201 810 17.16), which matches the other pulses in shape.

Table 2. Overview of total injected and removed particles as well as net wall result, for all discussed experiments. All particle numbers are given as 10^{20} H_2 molecules. Last column shows ratio of injected and removed particle count for easier comparison.

Scenario	Experiment ID	Plasma duration	Total injected	Total removed	Net wall	Removed/injected
Simple plasma (section 3)	201 808 29.6	4 s	3.23	25.9	−22.7	8.02
Short term retention (section 4)	201 808 16.9	15 s	37.6	30.0	7.60	0.80
	201 808 16.10	15 s	10.5	47.3	−36.8	4.50
Long term retention (section 5)	201 810 17.15	40 s	103	95.9	7.10	0.93
	201 810 17.16	53 s	89.2	287	−198	3.22
	201 810 17.17	78 s	99.9	344	−244	3.44
	201 810 17.19	100 s	129	402	−273	3.12

The inferred wall reservoir in figure 7 exhibits an interesting effect in all programs: after an initial phase of net retention it turns over and reaches net release around the time when the density starts to rise. This is understood as the wall particle source increasing with surface temperature, leading from initial net wall retention to net wall outgassing as the divertor tile temperature increases. The shift of this transition to later times and higher surface temperatures indicates, that particle reservoirs inside the graphite tiles are increasingly depleted and the outgassing happens only at higher surface temperatures. A plausible explanation is the spread of heat into the full divertor tile and even its holding structure.

A slight increase in the water signal in all RGAs indicates, that water is part of the released gas, presumably from previously unheated divertor parts. Due to the remaining boron layer from boronization, the oxygen is quickly gettered and does not strongly radiate in the plasma edge. The remaining hydrogen fuels the plasma and is measured as additional fueling source, which successively replaces the external gas fueling and leads to an increase in plasma density, when it exceeds the loss channels and the external gas fueling has ceased.

The net wall inventory in the first program is still slightly positive, with 7×10^{20} retained particles at the end of the outgassing phase, and turns strongly negative for the following programs, reaching a level of about 2×10^{22} removed molecules per program, of which up to a quarter was removed already during plasma. Overall, the sequence removed more than 7×10^{22} particles from the wall, which is about 4% of the estimated total reservoir in the carbon divertor.

It is concluded that the 100 s plasma could not be conducted without the preceding steps to condition the divertor, since the strong wall source otherwise would have raised the plasma density beyond the limit that can be sustained with the given heating power. For the upcoming campaigns with a water-cooled divertor, the picture however might change significantly. While the initial conditioning might take longer due to reduced outgassing time after plasma wetting, the heat cannot spread widely through the components and is hopefully efficiently exhausted without mobilizing deep reservoirs in the graphite. Also, the total amount of graphite is reduced in the divertor.

6. Conclusions

We have shown a gas balance for W7-X with an inertially cooled graphite divertor in attached scenarios. A wide range of operation regimes exists in varying wall conditions which either fill or deplete the wall with significant amount of hydrogen.

Significant wall heating is key to mobilize retained gas in the carbon structures, while auxiliary fueling on low-heated walls leads to strong fuel absorption. Even in a well-conditioned machine, preparatory plasma experiments were required to prepare long plasma experiments.

Especially after boronization, the influx of oxygen into the outer plasma could be well controlled even when mobilizing deep reservoirs containing water. Table 2 shows an overview of all discussed plasma scenarios and their key figures.

A systematic study beyond the shown cases could add to a better understanding of the long-term conditioning effect of plasma operation, which is important with respect to the steady-state target of W7-X in the future.

With a fully water-cooled first wall in future campaigns, equilibrium wall conditions during plasma will be easier to reach and should present a favorable environment for further plasma investigations. Both attached and detached plasmas will be able to reach steady wall conditions, and assessment of wall conditions will hopefully become much easier. Also, the available wall reservoir potentially shrinks, as the bulk material will not heat up as much anymore due to active cooling. The outgassing phase on the other hand will be shortened significantly due to rapid cooling of bulk and surface material, requiring different wall conditioning approach than with an inertially cooled divertor.

Acknowledgments

This work has been carried out within the framework of the EUROfusion Consortium and has received funding from the Euratom research and training programme 2014–2018 and 2019–2020 under Grant agreement No. 633053. The views and opinions expressed herein do not necessarily reflect those of the European Commission.

ORCID iDs

G. Schlisio https://orcid.org/0000-0002-5430-0645
U. Wenzel https://orcid.org/0000-0002-4107-9291
D. Naujoks https://orcid.org/0000-0003-4265-6078
T.S. Pedersen https://orcid.org/0000-0002-9720-1276
V.R. Winters https://orcid.org/0000-0001-8108-7774
H. Niemann https://orcid.org/0000-0003-0300-1060
M. Mulsow https://orcid.org/0000-0002-3737-8889
P. Drewelow https://orcid.org/0000-0003-0121-9058
Y. Gao https://orcid.org/0000-0001-8576-0970
M. Jakubowski https://orcid.org/0000-0002-6557-3497
A. Puig Sitjes https://orcid.org/0000-0002-4733-6068
J. Knauer https://orcid.org/0000-0001-7359-6472
K.J. Brunner https://orcid.org/0000-0002-0974-0457

References

[1] Loarer T. *et al* 2005 *20th IAEA Fusion Energy Conf. Proc.* **36** 36078348
[2] Beidler C. *et al* 1990 *Fusion Technol.* **17** 148
[3] Boscary J. *et al* 2011 *Fusion Eng. Des.* **86** 572
[4] Pedersen T.S. *et al* 2017 *Phys. Plasmas* **24** 055503
[5] Pedersen T.S. *et al* 2018 *Plasma Phys. Control. Fusion* **61** 014035
[6] Allen S.L. *et al* 2010 *23rd IAEA Fusion Energy Conf. Proc.* EXD/6-4
[7] Rohde V., Mayer M., Mertens V., Neu R. and Sugiyama K. 2009 *Nucl. Fusion* **49** 085031
[8] Rohde V., Kallenbach A., Mertens V. and Neu R. 2009 *Plasma Phys. Control. Fusion* **51** 124033
[9] Motojima G. *et al* 2015 *J. Nucl. Mater.* **463** 1080
[10] Nakamura Y. *et al* 2001 *J. Nucl. Mater.* **290–293** 1040
[11] Oberkofler M. *et al* 2013 *J. Nucl. Mater.* **438** S258
[12] Yu Y. *et al* 2012 *Plasma Phys. Control. Fusion* **54** 105006
[13] Loarer T. *et al* 2007 *Nucl. Fusion* **47** 1112
[14] Tanabe T., Bekris N., Coad P., Skinner C.H., Glugla M. and Miya N. 2003 *J. Nucl. Mater.* **313–316** 478
[15] Schlisio G., Klepper C.C., Harris J.H., Biewer T.M., Winters V.R., Wenzel U., Kornejew P., Laqua H. and Krychowiak M. 2019 *Rev. Sci. Instrum.* **90** 093501
[16] Dhard C.P. *et al* 2019 *Fusion Eng. Des.* **146** 242
[17] Reimold F., Wischmeier M., Bernert M., Potzel S., Kallenbach A., Müller H.W., Sieglin B. and Stroth U. 2015 *Nucl. Fusion* **55** 033004
[18] Drenik A. *et al* 2017 *Fusion Eng. Des.* **124** 239
[19] Brunner K.J. *et al* 2018 *J. Instrum.* **13** P0 9002
[20] Ford O.P. *et al* 2020 *Rev. Sci. Instrum.* **91** 023507
[21] Kubkowska M. *et al* 2018 *Fusion Eng. Des.* **136** 58
[22] Biel W., Greiche A., Burhenn R., Jourdain E. and Lepere D. 2006 *Rev. Sci. Instrum.* **77** 10F305
[23] Pavone A. *et al* 2019 *J. Instrum.* **14** C10003
[24] Wenzel U., Schlisio G., Mulsow M., Pedersen T.S., Singer M., Marquardt M., Pilopp D. and Rüter N. 2019 *Rev. Sci. Instrum.* **90** 123507
[25] Haas G. and Bosch H.-S. 1998 *Vacuum* **51** 39–46
[26] Kremeyer T., Flesch K., Schmitz O., Schlisio G. and Wenzel U. 2020 *Rev. Sci. Instrum.* **91** 043504
[27] Grote H., Kisslinger J., Renner H., Boscary J., Greuner H., Hoffmann F.W. and Mendelevitch B. 2003 *J. Nucl. Mater.* **313–316** 1298–303
[28] Feng Y. *et al* 2014 *Contrib. Plasma Phys.* **54** 426
[29] Schacht J. *et al* 2018 *Fusion Eng. Des.* **129** 6
[30] Barbui T. *et al* 2019 *J. Instrum.* **14** C07014
[31] Dibon M. *et al* 2015 *Fusion Eng. Des.* **98–99** 1759–62
[32] Gebhart T.E., Shiraki D., Baldzuhn J., Baylor L.R. and Meitner S.J. 2019 *Fusion Sci. Technol.* **75** 89–97
[33] Bussiahn R., Tamura N., McCarthy K.J., Burhenn R., Hayashi H., Laube R. and Klinger T. 2018 *Rev. Sci. Instrum.* **89** 10K112
[34] Wegener T. *et al* 2018 *Rev. Sci. Instrum.* **89** 073505
[35] McNeely P. *et al* 2013 *Fusion Eng. Des.* **88** 1034–7
[36] Pedersen T.S. *et al* 2019 *Nucl. Fusion* **59** 096014
[37] Zakharol A.P., Gorodetsky A.E., Alimov V.K., Kanashenko S.L. and Markin A.V. 1997 *J. Nucl. Mater.* **241–243** 52–67
[38] Niemann H. *et al* 2020 *Nucl. Fusion* **60** 084003
[39] Denisov E., Kompaniets T., Kurdyumov A. and Mazayev S. 1996 *J. Nucl. Mater.* **233–237** 1218
[40] Atsumi H. 2002 *J. Nucl. Mater.* **307–311** 1466
[41] Hino T., Higashi Y., Yamauchi Y., Komori A., Nishimura K. and Ashikawa N. 2008 *Vacuum* **83** 493
[42] Hino T., Katada Y., Yamauchi Y., Akiba M., Suzuki S. and Ezato T. 2009 *J. Nucl. Mater.* **386–388** 736

A.2. Article II

»First results from the implementation of the ITER diagnostic residual gas analyzer prototype at Wendelstein 7-X«
G. Schlisio, C. C. Klepper, J. H. Harris, T. M. Biewer, V. R. Winters, U. Wenzel, P. Kornejew, H. Laqua, M. Krychowiak and W7-X team
Review of Scientific Instruments, Vol. 90.9 (Sept. 2019), doi: 10 . 1063 / 1 . 5098125

Review of Scientific Instruments ARTICLE scitation.org/journal/rsi

First results from the implementation of the ITER diagnostic residual gas analyzer prototype at Wendelstein 7-X

Cite as: Rev. Sci. Instrum. 90, 093501 (2019); doi: 10.1063/1.5098125
Submitted: 1 April 2019 • Accepted: 12 August 2019 •
Published Online: 3 September 2019

G. Schlisio,[1,a)] C. C. Klepper,[2] J. H. Harris,[2] T. M. Biewer,[2] V. R. Winters,[3] U. Wenzel,[1] P. Kornejew,[1] H. Laqua,[1] M. Krychowiak,[1] and W7-X team[b)]

AFFILIATIONS

[1]Max-Planck-Institut für Plasmaphysik, Wendelsteinstraße 1, 17491 Greifswald, Germany
[2]Oak Ridge National Laboratory, Oak Ridge, Tennessee 37831-6169, USA
[3]University of Wisconsin-Madison, Madison, Wisconsin 53706, USA

[a)]georg.schlisio@ipp.mpg.de
[b)]See author list of T. Klinger *et al.*, Nucl. Fusion **59**, 112004 (2019).

ABSTRACT

Fusion reactors and long pulse fusion experiments heavily depend on a continuous fuel cycle, which requires detailed monitoring of exhaust gases. We have used a diagnostic residual gas analyzer (DRGA) built as a prototype for ITER and integrated it on the most advanced stellarator fusion experiment, Wendelstein 7-X (W7-X). The DRGA was equipped with a sampling tube and assessed for gas time of flight sample response, effects of magnetic field on gas detection and practical aspects of use in a state of the art fusion environment. The setup was successfully commissioned and operated and was used to observe the gas composition of W7-X exhaust gases. The measured time of flight gas response was found to be in the order of a second for a 7 m sample tube. High values of magnetic field were found to affect the partial pressure readings of the DRGA and suggest that additional shielding is necessary in future experimental campaigns.

I. INTRODUCTION

Long pulse plasma operation, such as in ITER and future fusion reactors, requires a continuous fuel cycle of particle input and exhaust to achieve equilibrium. Constant fueling is achieved by gas puffing or frozen fuel pellet injection. Gas exhaust is usually provided in a divertor configuration with a pump. Quantification of this exhausted gas gives easy and thorough insight into plasma wall interaction (PWI) and plasma processes (e.g., He formation, plasma chemistry, etc.) and is accomplished with a Diagnostic Residual Gas Analyzer (DRGA). The ITER DRGA is being developed at the Oak Ridge National Laboratory (ORNL) as a diagnostic for ITER.[1] The existing prototype for the ITER DRGA,[2] here abbreviated as P-DRGA, features an unshielded sensor cluster without the ITER sampling tube concept. The P-DRGA was integrated into W7-X with a simple divertor gas sampling tube to test the integrated measurement approach for the first time in an environment close to the ITER target design. Especially, the use of a pressure-reduced long sampling tube, which is key to this design, had not been experimentally demonstrated before.

Mass spectrometers are a convenient way of determining gas composition and are thus widely used in vacuum technology and are also foreseen in the ITER DRGA design explained in detail in Ref. 1. Their sensitivity to external magnetic fields and neutron irradiation, however, collides with common conditions in magnetic fusion experiments and future reactors, e.g., magnetic fields up to 8 T and intense high-energy neutron irradiation. To mitigate these effects, distance is an advantageous and cheap countermeasure. This results in a receded position from the plasma with a sampling tube connecting the actual analysis chamber to the region of interest, usually the divertor or pump region of a fusion device. As the sampling tube is made longer, the time response of the measurement becomes

worse. Introducing a pressure reducing orifice at the tip of the sampling tube allows maintaining molecular flow regime all along the tube and thus shortening time response and maintain diagnostic functionality.

Wendelstein 7-X (W7-X) is the world's most advanced stellarator fusion experiment.[3–5] With its graphite island divertor, water-cooled divertor tiles, and steady state magnetic field, it is designed for long pulse operation up to 30 min. After initial commissioning with a limiter, W7-X operated with an inertially cooled divertor unit over a span of two campaigns: OP1.2a (2017) and OP1.2b (2018). The P-DRGA was only operated in OP1.2b.

In Sec. II, we present the technical solutions of the P-DRGA setup. A simple analytical model for gas flow in the sampling tube is explained and compared to the experiment in Sec. III. In Sec. IV, the topic of magnetic field interference is briefly examined. The practical aspects of the measurements during W7-X experimental campaign OP1.2b are discussed in Secs. V and VI, and some final remarks are given in Sec. VII.

II. HARDWARE DESCRIPTION

The existing P-DRGA was lab-validated at ORNL.[6] It consists of an actively pumped analysis chamber equipped with a commercially available quadrupole mass spectrometer (MKS MV2), a spectroscopically observed Penning trap (Alcatel CF2), and some total pressure gauges for operational purposes. The ion trap mass spectrometer (ITMS) described in Ref. 2 has not yet been implemented. The emitted light from the Penning trap—located at an interstage port of the turbo molecular pump (TMP) to obtain higher pressure and thus stronger light emission—was collected by a lens and transferred about 50 m in an optical fiber with 1 mm core and observed with the W7-X filterscope system (see Refs. 7 and 8). An overview of the complete setup is shown in Fig. 1.

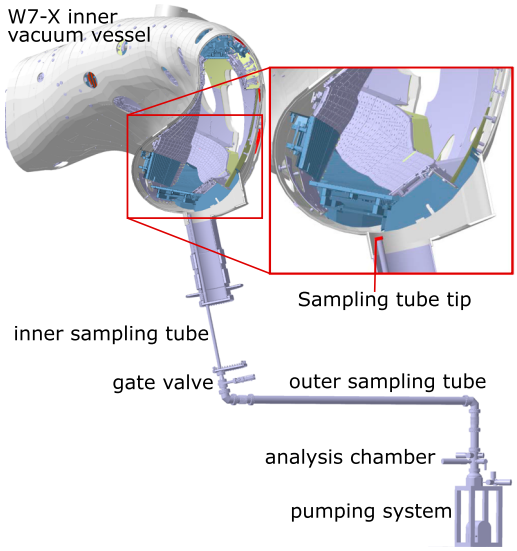

FIG. 1. Labeled overview of the complete system as installed on W7-X. The inset shows the position of the sampling tube in the port below the divertor. Cut taken at 203.4° toroidal angle.

A. Sampling tube

The top of the analysis chamber is connected with a sampling tube, leading gas from the W7-X subdivertor space to the DRGA analysis chamber. The sampling tube starts below the divertor about 0.5 m from the pumping gap. The portion of the sampling tube inside the vacuum system of W7-X is referred to as the *inner sampling tube*, while the portion exvessel is referred to as the *outer sampling tube*. A gate valve acts as a vacuum barrier and separator between the inner and outer sampling tube. The outer sampling tube continues through the torus hall outside of W7-X. Two bends (81° and 90°) turn the tube for the 3.4 m long horizontal section and back into the vertical position, where it connects with the analysis chamber. Each bend is followed by a bellows (one vertical, one horizontal) to reduce mechanical stresses on flanges. The complete tube is made from stainless steel, and the outer sampling tube as well as the analysis chamber are equipped with a heating mechanism to allow baking during vacuum commissioning. The dimensions of all parts are given in Table I, while Fig. 1 shows the position of the labeled sections as well as the position of the tube tip with respect to the divertor. The total length of the sampling tube is about 7 m.

The sampling tube is designed to quickly transport gas from the divertor area to the analysis region. Therefore, it is necessary to keep the gas flow in the molecular regime in all scenarios. To achieve this, the tip of the sampling tube is equipped with a pressure reduction mechanism embedded into a cap, whose setup is described in Sec. II B.

The ITER sampling tube will have to fulfill additional requirements, especially concerning tritium pumping. The geometrical path of the ITER DRGA will consist of a similar series of bends to navigate penetrations and other installed hardware. So, while the W7-X implementation is not a turn-for-turn clone of the planned ITER path, it is of a similar length and complexity. As such, the P-DRGA implementation on W7-X provides a valuable experimental test of the time-of-flight delays that can be expected on ITER. The current design for ITER calls from 2 DRGA systems. The total path length of the equatorial port DRGA path is 20 m, while the total path length of the divertor pumping port DRGA (in direct analog to the W7-X P-DRGA) is 10 m.

B. Cap

The opening of the inner sampling tube toward the subdivertor space has to ensure safe and defined conditions inside the sampling tube. This includes blocking of microwave stray radiation and reduction of pressure.

Microwave heating is an advantageous heating scheme for fusion plasmas. In W7-X the main heating scheme is electron cyclotron heating (ECH) with a frequency of 140 GHz[9] while ion cyclotron heating (ICH) is being prepared for future operation phases.[10] While most of the radiation is normally absorbed in the plasma, a fraction is scattered inside the vacuum vessel and forms a nearly isotropic radiation background, the so called *microwave stray radiation*.[11] Metal surfaces mostly reflect stray radiation, but it might interfere with any nonmetal equipment in the setup, e.g., gate valve insulation rings, measurement equipment, etc., and is thus to be kept away from those parts. An ECH filter made of 2 mm copper sheet with 286 holes of 0.7 mm diameter is the standard stray radiation

TABLE I. Overview of the geometry along the sampling tube. Lines marked with an asterisk were not taken into account in the TOF calculation. All parts are assumed to be straight cylinders, and for the cone, the mean diameter was used.

Description	Length (mm)	Diameter (mm)	Part
*Microwave stray radiation cover	2	39	Cap
*Spacer ring	5	39	
*Pressure reducing orifice	0.5	3	
Straight tube	2152	39	Inner sampling tube
Cone	81	39 . . . 70	
Gate valve and straight section	170	70	
Bend 81°	252	100	Outer sampling tube
Bellows	250	100	
Straight tube section	3140	100	
Bend 90°	270	100	
Bellows	250	100	
Straight tube section	265	100	
Analysis chamber upto RGA	150	100	Analysis chamber
*Analysis chamber upto pump	150	100	
Total length	7137.5		

blocking scheme utilized at W7-X for small tubes from microwave radiation with frequencies lower than 140 GHz. Such an ECH filter was mounted on the very tip of the DRGA sampling tube in a cap, as shown in Fig. 2.

This cap also holds an orifice plate with a central orifice. Tuning the diameter of this circular orifice reduces gas flow into the DRGA, reducing pressure in the sampling tube. This always ensures molecular flow along the tube and keeps the RGA at working pressures below 1×10^{-3} Pa in all realistic plasma scenarios. The gas flow calculations in Sec. III allow calculation of the maximum pressure inside the sampling tube just behind the orifice, to fulfill the aforementioned requirement. From the experience of the first divertor campaign, OP1.2a, the maximum subdivertor pressure to be expected in OP1.2b was estimated to be 1×10^{-1} Pa. This defines a pressure difference Δp cap has to sustain by restricting the flow.

Since the stray radiation filter also restricts the flow, it has to be taken into account. A motivation of the calculation is laid out in Appendix B. The calculated diameter for H_2 of 3.5 mm was rounded to 3 mm to have a safety margin. The divertor pressure did not quite reach the expected 0.1 Pa, but the pressure at the RGA was sufficient for operation while it did not exceed the safety threshold even at high pressure events. This scheme of orifice design can be regarded as a full success.

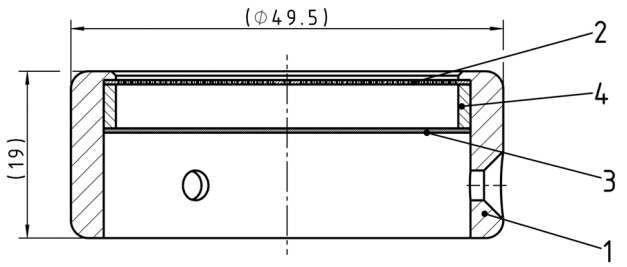

FIG. 2. Cut through the cap of the inner sampling tube: (1) body of the cap, (2) ECH stray radiation filter, (3) pressure reducing orifice plate, and (4) spacer ring. Dimensions in mm.

III. CONDUCTANCE AND TOF IN SAMPLING TUBE

For time-resolved data evaluation, an understanding of the time between the gas entering the sampling tube at the divertor end and the gas being analyzed at the RGA is required. We call this the *time of flight* (TOF). For complex geometries, this can be numerically calculated with commercially available codes, taking full geometry and wall conditions into account. A simple analytical model with some linear assumptions can also be applied and benchmarked with an experiment.

We assume molecular flow, the Knudsen number $Kn = \frac{\lambda}{D}$, the fraction of the mean free path λ, and the characteristic dimension (here: diameter of the tube) D in the sampling tube is to be above 1 at all times. For this calculation, we do not take the sampling tube cap into account, since its compact design will not influence the TOF in a significant way. Also, we calculate the maximum allowable pressure, which is defined by the maximum working pressure of the RGA at 1×10^{-3} Pa by vendor specification.

For the analytical model, we assume a completely straight tube consisting only of straight cylindrical sections with varying diameter. This allows the conductance, pumping speed, and pressure profile along the sampling tube to be calculated. The obtained pressure profile is shown in Fig. 3.

The TOF τ through a straight tube of length L and diameter D is calculated with

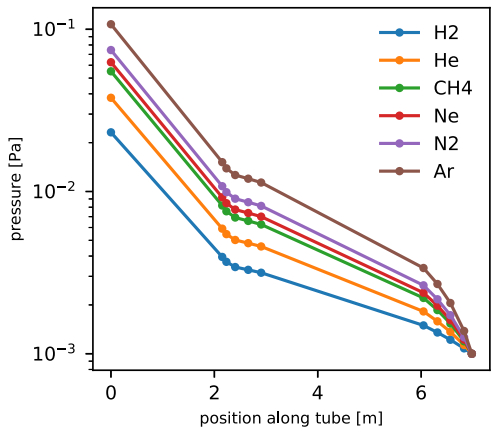

FIG. 3. Calculated pressure distribution at geometry boundaries of the sampling tube up to the tip. Geometry details in Table I.

$$\tau = \frac{\pi D^3 v L + 6 S_0 L^2}{4 D v S_0}, \tag{1}$$

where S_0 is the pumping speed at the pump side and v is the mean molecular speed of the gas. The derivation of this formula is given in Appendix A. The total TOF is then simply the sum over the TOFs of all geometric parts. Using the geometry of the sampling tube given in Table I and mapping it to a straight tube with constant diameters in each section, we can calculate the total TOF of the P-DRGA sampling tube.

An experimental comparison of this calculation was conducted by controlled gas puffing with different gases into the evacuated machine on the inner midplane, observing the pressure with gauges at various positions in the plasma vessel. The pressure at the sampling tube tip is inferred from the measured pressure in symmetric position in the top subdivertor space. A total pressure gauge in the P-DRGA analysis chamber is used to measure the pressure at the RGA. Due to constraints, these TOF experiments had to be performed outside campaign time and we had to deal with a few restrictions. Without magnetic field, the calibration of the manometers did not apply and the raw time trace data could be used. Measured pressure traces were analyzed for the pressure peak timing and the TOF deduced as time difference between the subdivertor pressure and analysis chamber pressure. The results of this analysis are shown in Fig. 4, where we compare the predicted TOF with the measured TOF. The error bars denote the standard deviation of the conducted measurements, and the remaining differences can be attributed to suboptimal experiment conditions and the simplicity of the model.

The dependence of the TOF on the gas mass requires a deconvolution of time dependent DRGA measured signals to accurately reflect the time dependence of the divertor gas composition.

The measurement requirements for the ITER DRGA systems specify a time response of 1 s for the divertor DRGA and 10 s for the equatorial DRGA. Since the sample piping of the P-DRGA is shorter than that planned for the ITER divertor DRGA, it is concerning that the measured TOF delay (~1.6 s) is longer than the

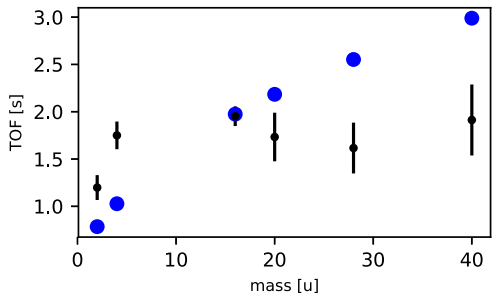

FIG. 4. Comparison of TOF for different gases: prediction from calculation (blue) and measured data (black).

ITER measurement requirement (1 s). However, there are a number of factors which can be used to improve the pumping response, which are planned for the ITER implementation including larger diameter tubing to improve the conductance and a higher throughput turbomolecular pump. The experimental results shown in Fig. 4 indicate a largely mass-independent TOF. Further investigation for the origin of this yet not understood discrepancy remains for future work.

IV. MAGNETIC FIELD EFFECTS

The plasma confining magnetic field[12] falls off quickly with the distance, but is not negligible at the P-DRGA position. With a minimum distance of 2.5 m to the outer vessel of W7-X, the maximum stray field at the position of the P-DRGA reaches up to 6 mT for W7-X main coil currents of ~16 kA (3 T on the axis field case, 108 turns). This is within the specification of most parts used, but requires shielding for the QMS. Magnetic shielding was achieved with a spaced double layer of mu-metal foil folded as two cylinders with closing pieces in the front and back. It should be noted that prior testing of the P-DRGA at ORNL indicated that 6 layers of mu-metal shielding would be sufficient to reduce the level of the external stray field (6 mT) to the values acceptable for the QMS operation (<0.5 mT). The solution was chosen over a solid mu-metal shield for simplicity and cost reasons. Due to insufficient shielding, magnetic field effects could be observed in the RGA signal on W7-X.

To benchmark the shielding, a constant flow of calibration gas was fed into the chamber and the partial pressures were observed during field ramps of the *high mirror* configuration. Figure 5 shows the signal attenuation of some of the calibration gases along with the background water vapor (18 u) against the mean coil current of the main coil system. A notable feature is the slight increase in pressure up until 4 kA, which suggests an increased sensitivity with the partially ramped field. This might be due to a partial compensation of the local geomagnetic field.

Thin layers of the mu-metal are effective as a magnetic shield, due to the high magnetic permeability of the alloy, as compared to equivalent thicknesses of "soft iron," which is also typically used to provide magnetic shielding to sensitive components. However, the effectiveness of mu-metal (or any material) at providing magnetic shielding is greatly reduced if the magnitude of the external magnetic field is sufficient to saturate the magnetic response of the

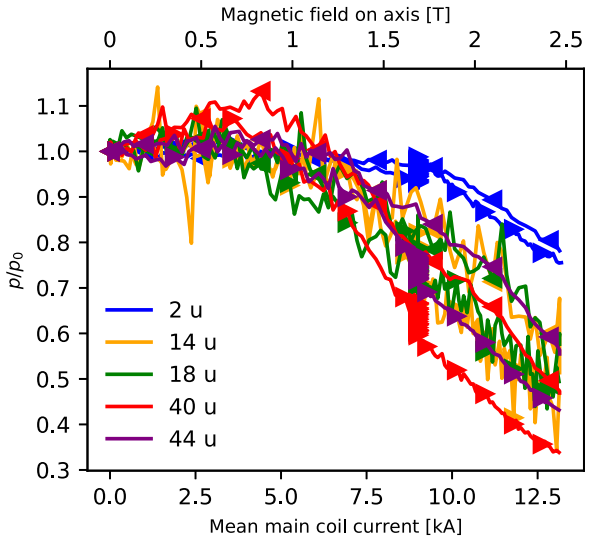

FIG. 5. Normalized partial pressure of several gases during main field ramp-up (triangle-right) and ramp-down (triangle-left). The magnetic configuration is so-called high mirror.

shielding material, i.e, the external field is large enough to permeate the full thickness of the shielding material. Figure 5 shows evidence that the 2-layer mu-metal shield which was used in this testing begins to saturate (and thus become ineffective) for mean main coil currents of >4 kA. The gas mass dependence of this effect is most likely due to the internal sensor geometry and a varying sensitivity to the effects of magnetic field on the flight paths of ions in the sensor. The main conclusion which can be drawn from this data is that additional magnetic shielding must be applied to the QMS in future campaigns when W7-X is operated at high main coil currents. It may be sufficient to add additional layers of mu-metal; however, for very high coil currents, an external soft-iron shield may be necessary to reduce the applied B-field to a level which prevents the mu-metal (in reasonable thickness) from saturating.

V. EXAMPLE DATA FROM W7-X PLASMAS

The P-DRGA was commissioned and operated during W7-X campaign OP1.2b. Example data from a W7-X plasma are shown in Fig. 6. The data presented were taken in the detachment program conducted in the *standard magnetic configuration* with main coil currents of about 13 kA. At this current, significant B field effects on the sensors should be expected, as indicated in Fig. 5. Nevertheless, the data will be presented as measured. The plasma lasted for 36 s and was powered with 4 MW of ECH power with a step-down to 3 MW at around 28 s. The line-integrated electron density stayed constant at 11×10^{19} m^{-2}. The plasma phase is highlighted with a shaded area in Fig. 6.

A. Mass spectra

The RGA mostly operated in the peak jump mode with a varying set of masses. The measured masses were adapted to the

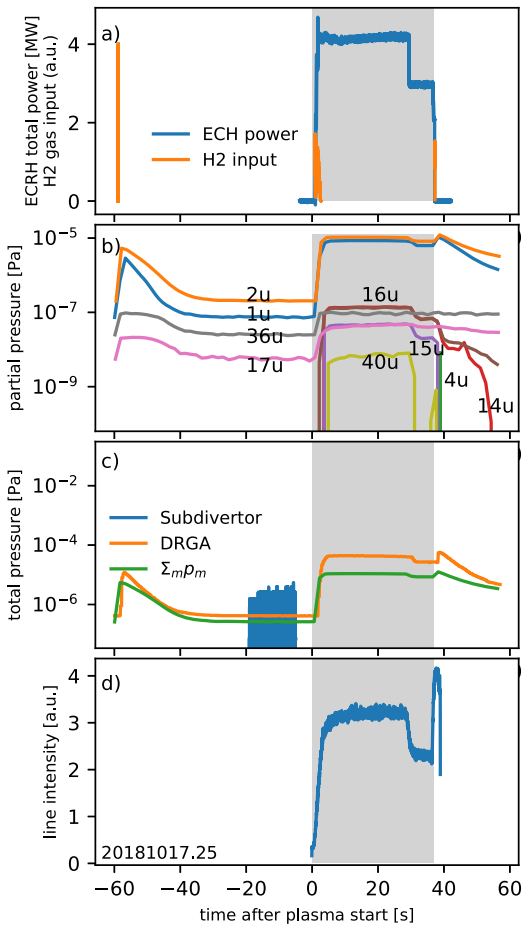

FIG. 6. Sample data from W7-X program 20181017.25 with an initial heating power of 4 MW and a step to 3 MW at 28 s and overall constant line-integrated electron density of 11×10^{19} m^{-2} (shaded region): (a) ECH total power and total H_2 gas flow. (b) Mass spectra as obtained from the RGA. Additional masses measured but omitted here for clarity reasons. (c) Comparison of pressures in the subdivertor space (AEH41), analysis chamber, and the sum of all measured partial pressures. (d) Emission intensity as measured by the filterscope for H_α (656.3 nm). See Sec. V, for further explanations.

programs planned. During the last day, full spectra were recorded between plasmas.

In Fig. 6(b), we show the time traces of selected masses for the previously described experiment. The valve test at −60 s is clearly visible in the partial pressure. During plasma startup, the partial pressures also rise significantly in the analysis chamber. The drop in heating power at 28 s is also visible as a drop in neutral pressure [see Fig. 6(c)] and partial pressure in the DRGA analysis chamber due to changing divertor condition (e.g., recycling flux). After the plasma heating is turned off and the plasma neutralizes, a clear peak in neutral and partial pressure is observed, as well as the wall outgassing afterward. The occurrence of a wide range of species shows the P-DRGAs ability to reliably detect trace gases, e.g., from plasma chemistry and outgassing.

The total pressure drop at 30 s, as shown in Fig. 6(c), occurs in the divertor pumping duct shortly before it is visible in the DRGA total pressure. This is in accordance with the results from the TOF calculations in Sec. III, which is, however, beyond the time resolution of the utilized measurement mode. The sum of partial pressures in Fig. 6(c) does not reach the total pressure measured in the analysis chamber, presumably due to the previously described stray magnetic field effects.

B. Spectroscopic measurements

The spectroscopic measurements were not fully commissioned. An Alcatel Penning trap was operated successfully, and the light was collected and transmitted via a 56 m long fiber with a 1 mm core and connected to the filterscope system of W7-X. It occupied four filterscope tubes, between which the light was shared via beam splitters. The first tube observed the H_α line and received 50% intensity, while the other three observed He lines and received 25%, 12%, and 12%, respectively. Due to the relatively dim discharge in the Penning trap and the vast majority of plasmas being hydrogen-only plasmas, the filter order was optimized for the hydrogen line. For more detailed information on the filterscopes, see Refs. 7 and 8.

Only tube 1 with the H_α filter showed a signal above noise. All other tubes (He-I lines) were not able to pick up a signal, even though several diagnostics observed residual helium in the plasma throughout the experimental campaign. Example data for the aforementioned experiment are shown in Fig. 6(d).

In other experiments with dedicated helium puffing, a slight increase in the He-I signal could be observed. Figure 7 shows a plasma of constant 4.5 MW heating and a line-integrated electron-density of about 8×10^{19} m^{-2} also in the standard magnetic configuration. The H_α reaches its maximum about 1 s after the hydrogen puff, and the He lines show a sharp onset at 8 s, about 2 s after the first puff. This is well in line with the prediction from Sec. III.

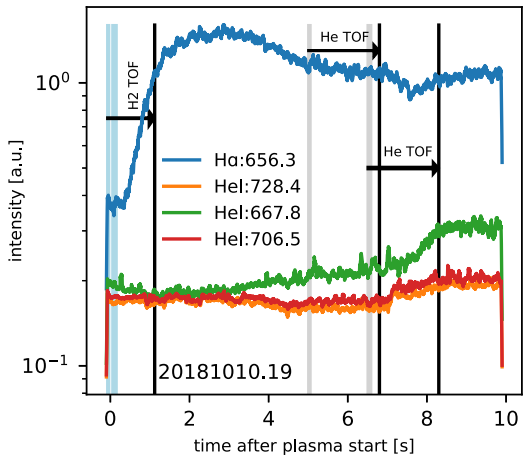

FIG. 7. Example plasma with gas puffing (20181010.19): spectroscopic lines in nanometer, shaded areas denote gas puffing: blue—H_2, gray—He. Black lines indicate the time of gas puff plus measured TOF from Sec. III.

VI. OPERATIONAL REMARKS

Before the campaign, the DRGA sampling tube and analysis chamber were baked out at a temperature of 80 °C for two weeks. The base pressure in the analysis chamber reached $2–3 \times 10^{-7}$ Pa. Due to a brief unscheduled opening of the vacuum, the bakeout of the outer sampling tube was repeated for about 50 h. The base pressure then reached 7×10^{-7} Pa and further improved with the ongoing campaign.

VII. SUMMARY AND NEXT STEPS

We have demonstrated successful integration of the P-DRGA into W7-X and demonstrated its ability to monitor partial pressures of plasma exhaust gases with time resolution of seconds and have also developed solutions to practical problems such as microwave radiation and pressure reducing orifice dimension. The time response of the system was measured and found to be in the expected range. This proved the general fitness of the DRGA concept for exhaust monitoring in magnetic fusion devices, but open questions remain.

Further work will concentrate on several points, technical and conceptual. The inclusion of the ITMS will provide the ability to scan full spectra in near real time. Thorough shielding with soft iron and mu-metal, as foreseen in the ITER DRGA design, will improve the resilience against magnetic field effects. A different data acquisition approach to the spectroscopic Penning trap with full observation of the spectrum or a changed filterset for the filterscopes promises to allow reliable and fast discrimination of deuterium and tritium,[13] highly relevant for fuel cycle monitoring. In addition, the data acquisition, control automation, and automatic data postprocessing state of the P-DRGA are not satisfying yet.

ACKNOWLEDGMENTS

This work was carried out within the framework of the EUROfusion Consortium and received funding from the Euratom research and training programme 2014–2018 and 2019–2020 under Grant Agreement No. 633053. The views and opinions expressed herein do not necessarily reflect those of the European Commission.

This work was supported in part by the U.S. Department of Energy, Office of Science, Office of Fusion Energy Sciences, under Grant No. DE-AC05-00OR2272.

We wish to acknowledge the support of the U.S.-ITER for the loan of the P-DRGA to W7-X, S. Hughes, vacuum group, ITER Organization for helpful advise, C. Marcus and M. Gamradt for extensive technical support, and the W7-X team for its great support during integration of the prototype into the machine.

APPENDIX A: DERIVATION OF GAS TOF

In this section, we derive the TOF through a straight circular tube of diameter D and length L (1). The conductance of such a tube is given by

$$c = \frac{\pi}{12} \cdot \frac{D^3}{L} \cdot \nu, \tag{A1}$$

with the mean molecular speed $v = \sqrt{\frac{8RT_g}{\pi m}}$. The pumping speed at a point separated from a point of pumping speed S_0 by a pipe of conductance c is given by

$$S = \frac{S_0 \cdot c}{S_0 + c}. \tag{A2}$$

The gas throughput through a system has to be constant along the line in an assumed equilibrium; here, given at the point of the RGA,

$$Q = p_{rga} \cdot S_{rga} \tag{A3}$$

gives the pressure along the tube,

$$p = \frac{Q}{S} = Q\frac{S_0 + c}{S_0 \cdot c}. \tag{A4}$$

The propagation time (TOF) of gas through a set of cylindrical volumes V_n with pressures p_n can be expressed by

$$\tau = \sum_n \frac{p_n \cdot V_n}{Q} = \frac{\pi D^2}{4Q} \sum_n p_n l_n, \tag{A5}$$

which can be transformed into an integral along the axis, giving the following expression for the TOF through a pipe with geometry of diameter D and length L:

$$\tau = \frac{\pi D^2}{4Q} \int_0^L p(l)dl, \tag{A6}$$

$$= \frac{12}{4DS_0 v} \int_0^L l\left(S_0 + \frac{\pi}{12} \cdot \frac{D^3}{l} \cdot v\right)dl \tag{A7}$$

$$= \frac{L}{4}\left(\frac{\pi D^2}{S_0} + \frac{6L}{Dv}\right) \tag{A8}$$

$$= \frac{\pi D^3 vL + 6S_0 L^2}{4DvS_0}. \tag{A9}$$

The complete propagation time in the case of the P-DRGA is gained by taking the sum over all pipe geometry sections.

Pumping speed unspecified by the vendor was derived using Ref. 14.

APPENDIX B: DERIVATION OF ORIFICE DIAMETER

The conductance of a tube can also be expressed in terms of the gas throughput Q and the pressure drop Δp between the ends,

$$c = \frac{Q}{\Delta p}, \tag{B1}$$

which, in turn, means that with the known gas throughput we can calculate the required conductance to yield a given pressure difference.

The conductance of an ideal orifice with a length of zero is[15]

$$c_{\text{ideal orifice}} = \frac{v}{4}A = \frac{\pi}{16}D^2 v \tag{B2}$$

with the mean molecular speed v and the area A of the circular orifice of diameter D. The conductance of a (long) tube is calculated by

$$c_{\text{tube}} = c_{\text{ideal}} \cdot P \tag{B3}$$

with the transmission probability P for a circular pipe of length L and diameter D being

$$P = \frac{4}{3}\frac{D}{L}, \tag{B4}$$

yielding

$$c_{\text{real}} = \frac{v}{4}A \cdot P = \frac{\pi}{12}\frac{D^3}{L}v. \tag{B5}$$

For a short tube edge, effects have to be taken into account, which yields the real conductance for an orifice—or short tube[16]—as

$$c_{\text{real orifice}} = \frac{c_{\text{ideal orifice}} \cdot c_{\text{tube}}}{c_{\text{ideal orifice}} + c_{\text{tube}}}, \tag{B6}$$

where the length now is the plate thickness.

The optimal diameter of the orifice is thus determined by the equilibrium condition

$$\frac{Q}{\Delta p} = c_{\text{real orifice}}. \tag{B7}$$

The conductance of the ECH cover is calculated as the number of holes times the conductance of a single orifice (D = 0.7 mm, L = 2 mm, N = 286) and accordingly (B1) reduces Δp.

REFERENCES

[1] C. C. Klepper, T. M. Biewer, V. B. Graves, and P. Andrew, Fusion Eng. Des. **96**, 803–807 (2015).
[2] T. R. Younkin, T. M. Biewer, and C. C. Klepper, Rev. Sci. Instrum. **85**(11), 11E816 (2014).
[3] C. Beidler *et al.*, Fusion Technol. **17**, 148 (1990).
[4] H. S. Bosch *et al.*, Nucl. Fusion **53**(12), 126001 (2013).
[5] R. C. Wolf *et al.*, IEEE Trans. Plasma Sci. **44**, 1466 (2016).
[6] C. C. Klepper, T. M. Biewer, C. Marcus, P. Andrew, W. L. Gardner, V. B. Graves, and S. Hughes, J. Instrum. **12**(10), C10012 (2017).
[7] R. J. Colchin, D. L. Hillis, R. Maingi, C. C. Klepper, and N. H. Brooks, Rev. Sci. Instrum. **74**, 2068 (2003).
[8] L. Stephey, G. A. Wurden, O. Schmitz, H. Frerichs, F. Effenberg, C. Biedermann, J. H. Harris, R. König, P. Kornejew, M. Krychowiak, E. A. Unterberg, and W7-X Team, Rev. Sci. Instrum. **87**, 11D606 (2016).
[9] M. Thumm, P. Brand, H. Braune, G. Dammertz, V. Erckmann, G. Gantenbein, and C. Lechte, Plasma Fusion Res. **5**, S1006 (2010).
[10] J. Ongena, A. Messiaen, D. Van Eester, B. Schweer, P. Dumortier, F. Durodie, and A. Krivska, Phys. Plasmas **21**(6), 061514 (2014).
[11] D. Hathiramani, R. Binder, R. Brakel, T. Broszat, B. Brucker, A. Cardella, and S. Thiel, Fusion Eng. Des. **88**(6-8), 1232–1235 (2014).
[12] T. Sunn Pedersen, M. Otte, S. Lazerson, P. Helander, S. Bozhenkov, C. Biedermann, T. Klinger, R. C. Wolf, H.-S. Bosch, and W7-X Team, Nat. Commun. **7**, 13493 (2016).
[13] C. C. Klepper, S. Vartanian, B. Pegourie, D. Douai, E. Delabie, I. Jepu, and U. Kruezi, in Bulletin of the American Physical Society, 2018, see https://scholar.google.com/scholar?cluster=14344157583079379155&hl=de&as_sdt=0,5&as_ylo=2018.
[14] O. B. Malyshev, Vacuum **81**(6), 752–758 (2007).
[15] M. Wutz *et al.*, *Handbuch Vakuumtechnik* (Vieweg, 2000).
[16] J. M. Lafferty and L. G. Rubin, "Foundations of vacuum science and technology," Phys. Today **52**(3), 86 (1999).

A.3. Article III

»Performance of new crystal cathode pressure gauges for long-pulse operation in the Wendelstein 7-X stellarator«
U. Wenzel, G. Schlisio, M. Mulsow, T. S. Pedersen, M. Singer, M. Marquardt, D. Pilopp and N. Rüter
Review of Scientific Instruments, Vol. 90.12 (Dec. 2019), doi: 10.1063/1.5121203

Review of Scientific Instruments ARTICLE scitation.org/journal/rsi

Performance of new crystal cathode pressure gauges for long-pulse operation in the Wendelstein 7-X stellarator

Cite as: Rev. Sci. Instrum. 90, 123507 (2019); doi: 10.1063/1.5121203
Submitted: 25 July 2019 • Accepted: 26 November 2019 •
Published Online: 17 December 2019 • Publisher Error Corrected: 20 December 2019

Uwe Wenzel,[a] Georg Schlisio, Matthias Mulsow, Thomas Sunn Pedersen, Martin Singer, Mirko Marquardt, Dirk Pilopp, and Nils Rüter

AFFILIATIONS

Max Planck Institute for Plasma Physics, Wendelsteinstrasse 1, 17491 Greifswald, Germany

[a]E-mail: uwe.wenzel@ipp.mpg.de

ABSTRACT

To improve the reliability of the ASDEX pressure gauges in the plasma vessel of the Wendelstein 7-X stellarator, nine of them were equipped with a LaB_6 crystal electron emitter for the first time. These crystal cathode pressure gauges were operated during the last campaign in 2018 (operation phase 1.2b) with only 2 A heating current for over 40 h in a magnetic field of about 2.1 T without failure. Owing to this excellent performance, we have decided to equip all pressure gauges with crystal cathodes for the next campaign of Wendelstein 7-X (operation phase 2). We report on a pretest in a superconducting magnet, show a measurement of the neutral pressure in Wendelstein 7-X, and demonstrate the long-term stability of the crystal cathode pressure gauges.

I. INTRODUCTION

Measurement of the neutral pressure is a key diagnostic for the island divertor of the Wendelstein 7-X stellarator. From the subdivertor neutral pressure in front of the pumping ducts, it is possible to calculate the particle exhaust rate. ASDEX pressure gauges (APGs) are the state-of-the-art devices for these measurements in the strong magnetic fields of fusion devices.[1] They are used in several tokamaks, among them DIII-D[2] and ASDEX Upgrade,[3] and their use is also foreseen for ITER.[4] At ITER, they are called diagnostic pressure gauges (DPGs). We also use them in Wendelstein 7-X at several subdivertor and midplane positions. The typical magnetic field is 2.1 T.

APGs are hot-cathode ionization pressure gauges. The first cathodes for Wendelstein 7-X were made from thoriated tungsten wires with a diameter of 0.6 mm (OSRAM G18). These cathodes were heated with currents between 14 and 18 A to obtain an electron current of 200 μA at the anode grid. However, in the first two operation phases, namely, OP1 and OP1.2a, they were frequently found to be deformed, presumably as a result of the $\mathbf{j} \times \mathbf{B}$ force on the cathode wires.[5] Since we use plug-ins to position the pressure gauges, we were able to retract them to repair the damaged ones. This could be done only between operation phases, so not all installed APGs were available for pressure measurements.

Similar problems were reported from the tokamaks JET[6] and KSTAR.[11] As in Wendelstein 7-X, the typical bending pattern of a 0.6 mm tungsten wire can lead to a short circuit by contact with the control electrode.

Hoping to improve the robustness of the pressure gauges, we substituted the tungsten wires with a different emitter for 11 of the APGs during the third operation phase of Wendelstein 7-X, OP1.2b. This type of pressure gauge was recently developed by Wenzel *et al.*[7] It makes use of a LaB_6 crystal rod as a thermionic bulk emitter. LaB_6 has the advantage of better electron emission than thoriated tungsten by the lower work function. With the LaB_6 crystal, the pressure gauge was operated in the laboratory with a very low heating current of 1.5 A, i.e., with a considerably lower current than needed for the APGs with the 0.6 mm tungsten cathodes. The successful initial test in a superconducting magnet at comparable field strength and hydrogen pressures (see Sec. II) encouraged us to use a larger number in Wendelstein 7-X. After OP1.2a, 8 pressure gauges either remained unchanged or were equipped with a fresh tungsten

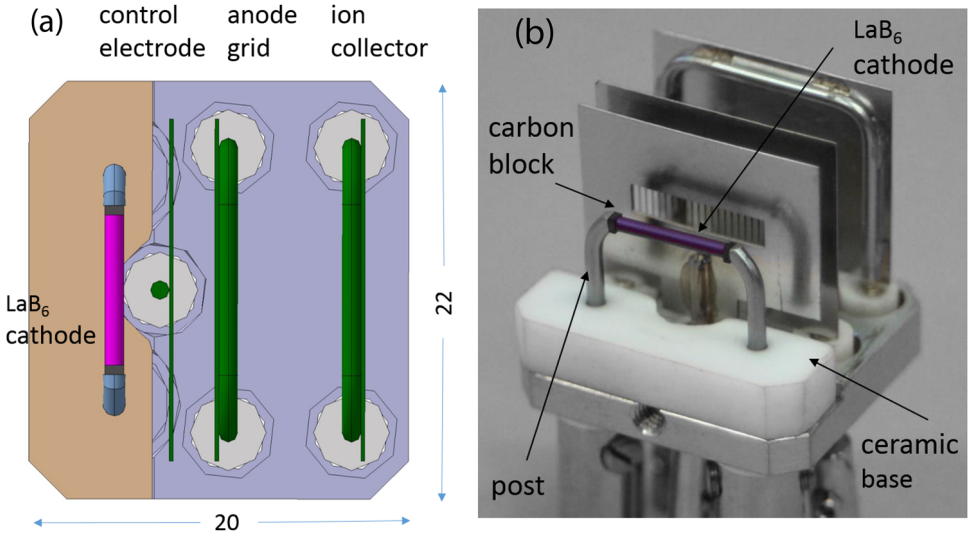

FIG. 1. (a) Schematic of the pressure gauge head with the LaB_6 cathode (bird's eye view) and (b) the realized gauge head mounted on port AEP51.

cathode, while the other 11 were replaced by the new pressure gauges. We call the new design a crystal cathode pressure gauge (CCPG). These are basically ASDEX pressure gauges with a crystal emitter, although the crystal emitter is not the only distinguishing feature: in addition, the distance between the emitter and the control electrode, as well as the electrode biasing settings, is different from previous gauges. Crystals cannot be ohmically heated because of the low resistance. Instead, small pyrolytic graphite blocks are heated by ohmic dissipation, and the blocks, in close contact with the crystal, heat the crystal indirectly (the so-called Vogel mount;[8] see also Fig. 1 for an image of the crystal emitter).

We report on the performance of the CCPGs in Wendelstein 7-X during OP1.2b. First, some results of a pretest in a superconducting magnet are described in Sec. II. In Sec. III, the setup of the 11 CCPGs in Wendelstein 7-X is described. Two of the CCPGs had some problems from the beginning. One was not functional after baking, while the other was not exactly oriented along the magnetic field, with the consequence that only a small electron current could be drawn from the LaB_6 emitter. Neither pressure gauge was routinely operated. The calibration of the nine other CCPGs is also described in Sec. III. In Sec. IV, we report on the behavior of the CCPGs in OP1.2b. We give an example of a neutral pressure measurement and demonstrate the large reduction in the heating current of the CCPG in a direct comparison with a standard APG. Finally, we characterize the long-term behavior of the CCPGs in Sec. V from three different aspects: stability of the heating current in a strong magnetic field, stability of the pressure measurement, and visual inspection after OP1.2b.

II. PRETESTS IN A SUPERCONDUCTING MAGNET

Before the application in Wendelstein 7-X, we tested the first prototype of a CCPG over 5 days in a superconducting magnet at 3.1 T. Details of the pressure gauge with the LaB_6 crystal emitter and the experimental setup are described in Ref. 7. The long-term test was carried out in the following way. The pressure was set to 5 $\times 10^{-3}$ mbar hydrogen using a Baratron mounted 1 m away from the magnet. The pressure on the axis of the magnet (at 3.1 T) was measured continuously over 29 min with the CCPG. After a break of 1 min, the next measurement, with a sample time of 29 min, was started. This procedure was repeated for 12 h per day. We performed in total $24 \times 5 = 120$ measurements and accumulated 29 min $\times$ 120 = 58 h operation time.

During the long-time experiment, the CCPG was operated in the feedback mode on an electron current of 200 μA. Figure 2 shows the ion and heating currents in each of the measurements and the hydrogen pressure, as measured by the Baratron. Since we did not actively control the pressure, it varied over the five experimental days. To eliminate this variation, the measured ion current was normalized to the pressure measured with the Baratron. The CCPG data were averaged over 25 min, with the exception of the first 5 min.

The heating current shows two characteristic effects. At the start of each day, a decrease is observed. We call this the *formation effect*, and it occurs after a rest of 12 h in vacuum without hydrogen gas. By fitting the decaying current level to an exponential function, a formation time of 42 min is obtained. We suspect that this is due to the capability of the carbon blocks to store hydrogen (see the discussion in Sec. V A). Another effect is the small increase in the heating current from day to day. We call this the *aging effect*. Assuming a linear aging trend, the heating current limit of 3 A (to avoid overheating of the emitter unit) would be reached after 1172 h.

We observed that the ion current is not constant as expected for a constant hydrogen pressure [see Fig. 2(a)]. We think that this is the consequence of an ambiguity of the ion current because the ion current sometimes exhibited spontaneous jumps during the 29 min runs in the magnet. Figure 3(a) shows examples of jumps observed during the long-term experiment and in Wendelstein 7-X. In the CCPG, spontaneous jumps of the ion current occurred despite a constant hydrogen pressure. In this particular example, the ion current jumped from 7.1 to 6.1 μA and stayed at this level for more than 10 min. Then, a jump to 6.7 μA occurred and, again, the ion current stayed at this level for more than 10 min. It must be emphasized

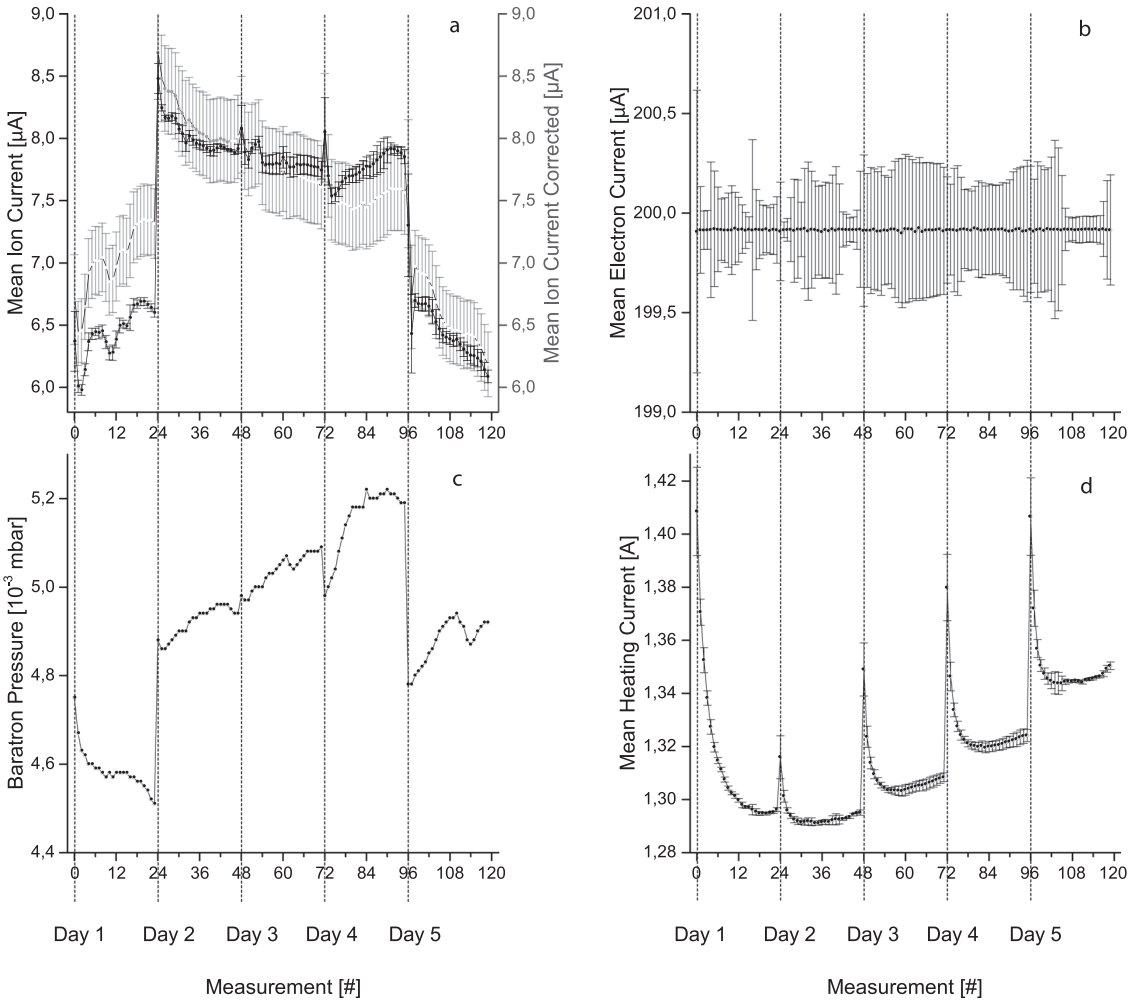

FIG. 2. Response of the CCPG in a steady-state magnetic field of 3.1 T over 58 h. The reference pressure was measured with a Baratron. It is about 5×10^{-3} mbar [see (c)]. The CCPG data {raw ion [(a), black line], electron (b), and heating current (d)} are plotted vs the number of the measurement. The ion current of the CCPG was normalized to the reference pressure [gray line in (a)].

that the electron current was constant at 200 μA for all three levels of ion current due to the feedback operation. Such behavior is not a property of the LaB_6 cathode but was also observed in pressure gauges with cathodes made from tungsten wires [see the example in Fig. 3(b) from Wendelstein 7-X]. The electron current had the same value of 200 μA. We see a transition between the two levels with an ambiguous behavior in the transition phase. The measurement accuracy is reduced by this instability since we do not know which level the pressure gauge is in during the measurement compared with the level during the calibration. When we take the jump from 7.1 μA to 6.1 μA, i.e., 1 μA (which is about 15% from the larger value of 7.1 μA), then the accuracy is about 15%. The example from Wendelstein 7-X shows even larger relative jumps of about 25%, but this seems to be the case only in a transition phase from level 1 to level 2. At the moment, we have no sure explanation for this effect.

Finally, we studied the behavior of the CCPG at high neutral pressures. In hydrogen, we found an upper pressure limit of 2×10^{-2} mbar. At this pressure, the ion current begins to saturate. Since for the island divertor of Wendelstein 7-X, maximum values of the order of 10^{-3} mbar were predicted,[9] this limit is sufficient for the experiments in Wendelstein 7-X.

III. SETUP AND CALIBRATION OF THE CCPGs

The successful pretest of the CCPG in the superconducting magnet encouraged us to install 11 CCPGs in Wendelstein 7-X. After baking and the first tests, we found nine of them to be fully functional, while two had severe problems that prevented operation. These problems, however, were not caused by the pressure gauges themselves but by mounting. Table I shows some details of the setup of the remaining nine CCPGs.

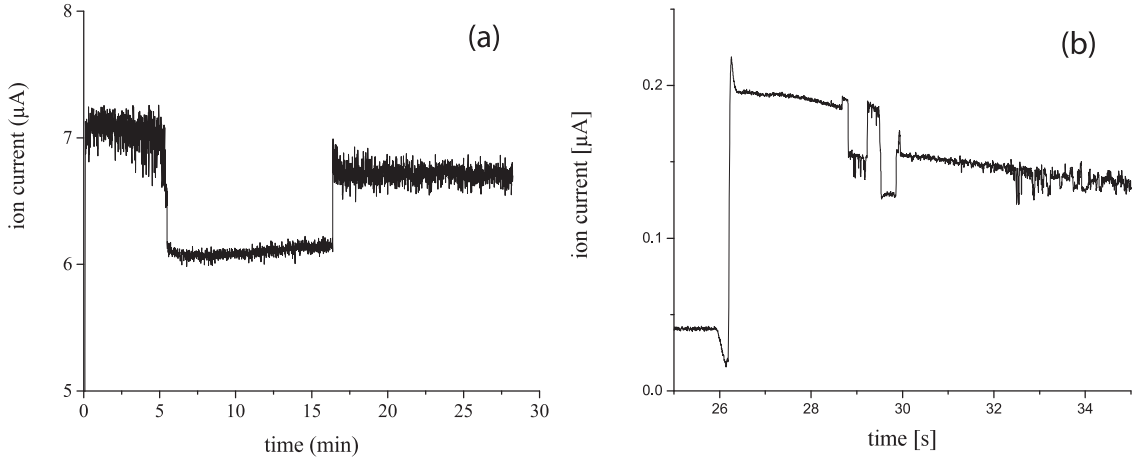

FIG. 3. Spontaneous jumps of the ion currents of different pressure gauges at (nearly) constant hydrogen pressure: (a) LaB_6 cathode (superconducting magnet) and (b) tungsten cathode (Wendelstein 7-X). This instability limits the measurement accuracy. When we take the jumps observed in the ion current of the CCPG, the accuracy is estimated to be 15%.

The CCPGs were positioned at several relevant positions in the plasma vessel: two in midplane positions, three near the pumping gaps of the divertor (through port AEI), and four in the front of the pumping ducts (two in the AEP ducts and two in the AEH ducts). Figure 4 shows a poloidal cross section of W7-X with the positions of the CCPGs. The highest pressures were expected near the pumping gaps of the island divertor (port AEI) and the lowest at the midplane (port AEE or AEA). The placement of gauges at different positions ensures that the CCPGs are tested over a wide pressure range.

At the beginning of the campaign, all CCPGs were calibrated against a reference pressure obtained from gas type independent capacitance manometers and gas type corrected Penning gauges in their respective pressure range. The calibration was performed in the magnetic standard configuration as was set up as a series of hydrogen puffs into a unpumped vacuum vessel leading to phases of the equilibrated pressure. The obtained ion current was fitted to the reference pressure with a linear model without offset ($p = C * I_i$), which is a common approach for hot ion cathode gauges in the low and medium pressure range (see Fig. 9). Figure 5 shows the time traces of the calibrated CCPGs overplotted with the reference pressure. Residual deviations could be corrected with a more complex model. All calibrations were performed only for an electron current of 200 μA, at which all CCPGs were operated throughout the campaign.

IV. MEASUREMENT RESULTS

During OP1.2b, the CCPGs were operated for a total of about 40 h in the magnetic field, i.e., slightly less than in the long-term test in the magnet. We start the analysis of the performance of the CCPGs with an example of the pressure measurements in the standard divertor configuration. Then, we compare the heating current of the new LaB_6 cathode design with that of the standard APG with a tungsten cathode.

A. Example of a neutral pressure measurement

Figure 6 shows the pressure distribution of a typical plasma experiment in the so-called standard divertor configuration. In this

TABLE I. Details of the spatial positions and the calibration factors C of the nine CCPGs in Wendelstein 7-X. Calibration of the CCPG in port AEH41 was obtained after the operation phase 1.2b (marked by an asterisk).

Port	Functionality	Module	Position	C (10^{-4} mbar/μA)
AEA21	Plasma vessel	2	Midplane	2.845
AEH30	Pumping duct (standard)	3	Bottom	4.0627
AEP30	Pumping duct (high iota)	3	Bottom	3.892
AEE41	Plasma vessel	4	Midplane	2.2146
AEP51	Pumping duct (high iota)	5	Top	2.5248
AEH41	Pumping duct (standard)	4	Top	2.5835*
AEI30	Pumping gap (standard)	4	Bottom	2.7546
AEI50	Pumping gap (standard)	5	Bottom	2.6260
AEI51	Pumping gap (standard)	5	Top	2.5846

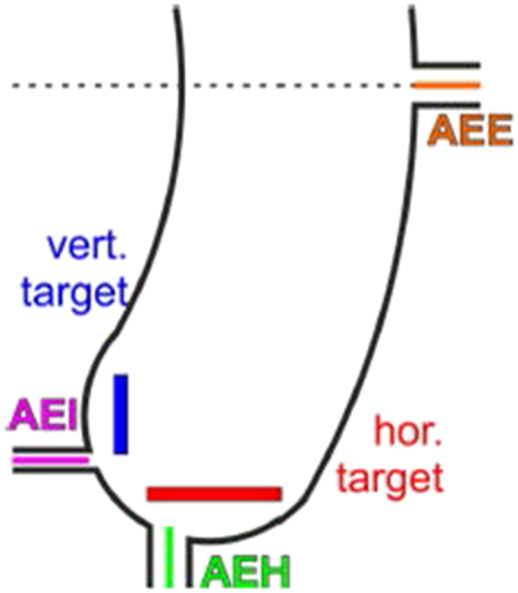

FIG. 4. Schematic poloidal cross section of Wendelstein 7-X with some typical positions of the CCPGs: near the divertor pumping gap (port AEI), in the pumping duct (port AEH), and at the midplane (ports AEE and AEA).

configuration, particles are mainly deposited at the low-iota tail of the divertor target (near the AEH and AEI ports). This experiment has three electron cyclotron resonance heating (ECRH) power steps (2 MW, 3 MW, and 4 MW) at an almost constant line-integrated density of 5×10^{19} m^{-2}. Figure 6 shows the neutral pressures measured in the midplane (an average of AEE41 and AEA21), in the pumping ducts (AEH41 and AEH30), and near the pumping gaps (AEI50 and AEI51).

We can distinguish the two phases. The *experiment phase* is 7 s long and is followed by the *outgassing phase*. In the experiment phase, the three power steps are clearly visible in the subdivertor neutral pressures. The maximum pressure is measured near the pumping gap. The subdivertor pressure at the pumping ducts is

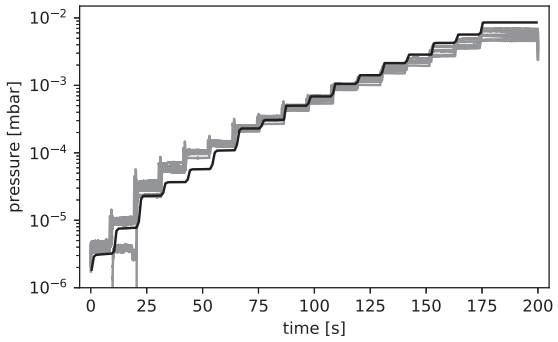

FIG. 5. Pressure steps in hydrogen gas in the vacuum vessel of Wendelstein 7-X with a standard magnetic field. The reference pressure is plotted in black. All CCPGs are plotted in gray with their individual calibration factors given in Table I.

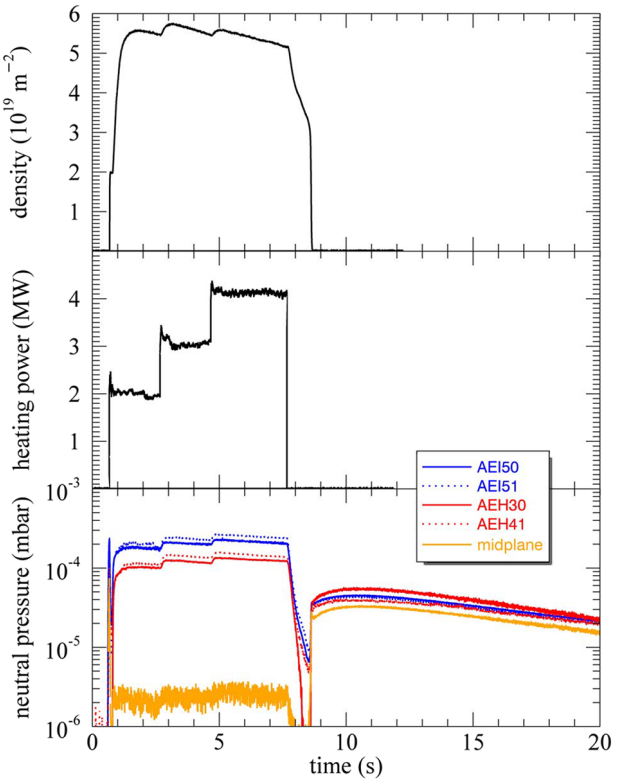

FIG. 6. Neutral pressures in a typical plasma experiment with three heating power steps and constant plasma density (in the so-called magnetic standard configuration). The experiment number is 20181010.005.

a factor of 2 lower. The neutral compression, defined as the pressure ratio between the midplane and pumping duct (AEH), is about 50. The subdivertor neutral pressures in the divertors on top are slightly higher. In the outgassing phase, there is no plasma and no gas fueling from external valves. Neutral particles that are released from the first wall fill the plasma vessel, and the measured neutral pressures are close to each other, independently of the position of the pressure gauge.

The maximum subdivertor neutral pressure was 2×10^{-3} mbar measured in the AEP51 pumping duct in the magnetic high-iota configuration.

B. Comparison of the heating currents of APG and CCPG

The new pressure gauges were designed to reduce the heating current of the emitter in the magnetic field. Figure 7 compares the electrical parameters of the cathode circuits of both types of pressure gauges. Data were sampled in experiment 20181010.005 shown in Fig. 6. The time interval in Fig. 7 is the same as in Fig. 6. APG data are from two AEH pumping duct positions (AEH11 in module 1 and AEH51 in module 5). The electron current at the anode grid was set to 200 μA, independently of the pressure gauge type. CCPGs need about 2 A to obtain this current, while the heating current for the

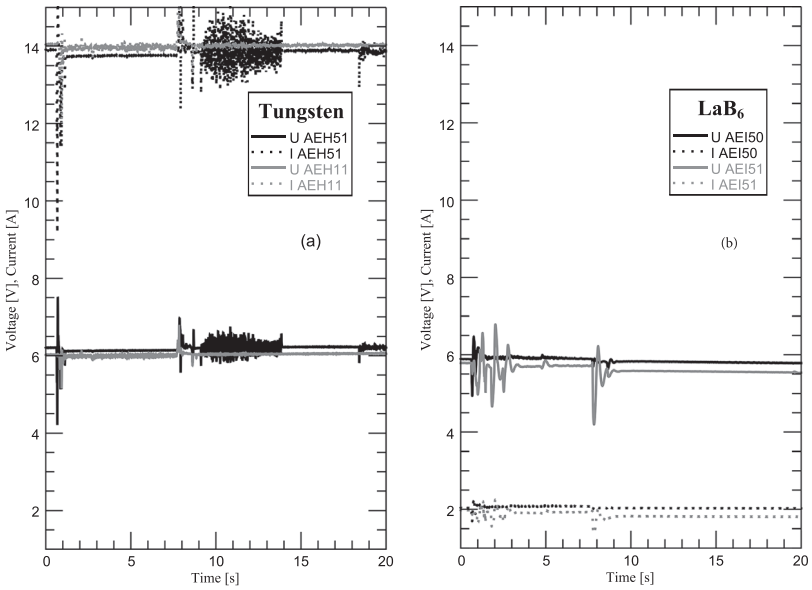

FIG. 7. Comparison of the heating currents *I* and voltages *V* of the two types of pressure gauge in the same experiment as shown in Fig. 6: (a) with tungsten cathodes and (b) with LaB_6 cathodes. With the new LaB_6 cathode design, the heating current is reduced from 14 A to 2 A.

two APGs is 14 A. The voltage of the power supply needed to drive the heating currents is about 6 V in both cases.

V. LONG-TERM BEHAVIOR OF THE CCPGs IN WENDELSTEIN-X

A. Heating current of the LaB_6 emitter

All nine CCPGs were operated for 40 h in the magnetic field of Wendelstein 7-X without failure, i.e., a bit less than the long-term test in the superconducting magnet. Figure 8 shows the current and resistance of an emitter circuit from all experiments in OP1.2b. Data are from the pressure gauge in port AEA21 (midplane position in the plasma vessel, module 2). The pressure measurement was started 20 s before the ignition of the plasma. Data are averaged between 6 and 19 s after the trigger event, i.e., in the time before the plasma.

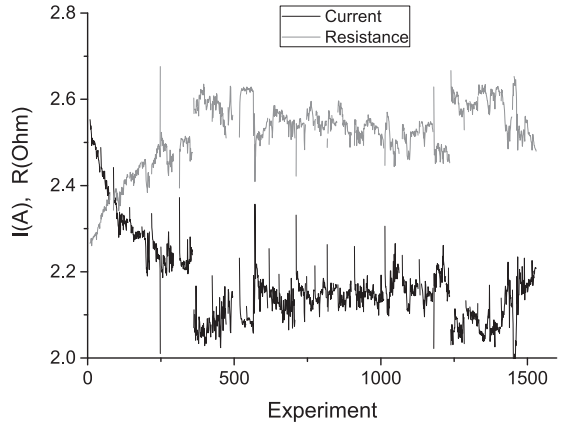

FIG. 8. Heating current *I* and resistance *R* of the emitter circuit of the CCPG in port AEA21 vs the experiment number. Data are from the whole of OP1.2b. The heating current is feedback-controlled to ensure an electron current of 200 μA at the anode grid.

The resistance increases in the first 250 experiments from 2.3 Ω to 2.5 Ω. At the same time, the heating current decreases from 2.5 A to about 2.25 A. Furthermore, two sudden jumps are observed in the resistance from 2.5 Ω to 2.6 Ω and consequently in the heating current too.

We interpret the data as follows. The resistance of the emitter circuit is determined by the carbon blocks, which are the elements with the highest resistance compared to the posts and the crystal. The change in resistance is consequently due to the carbon blocks. Carbon is known for its property of storing a substantial amount of hydrogen. In the initial phase, the blocks store hydrogen, which presumably increases their electrical resistance. This hypothesis is supported by laboratory studies. At least for raw graphite, an increase in resistance was found when hydrogen was stored.[10] By this effect, the blocks become hotter and less heating current is needed to obtain an electron current of 200 μA at the anode grid. After 250 experiments, the blocks are saturated with hydrogen, and the resistance stays constant. The two jumps in resistance from 2.5 Ω to 2.6 Ω correlate with the boronization of the plasma vessel. Apparently, the boronization can also change the resistance of the blocks. Again, the higher resistance leads to a lower heating current owing to the hotter blocks.

The absolute current limit of the LaB_6 emitters is 4 A. It is determined by the maximum allowed temperature of the carbon blocks. With the heating current in the range of 2.1–2.5 A before plasma operation, there is a sufficient margin to the 4 A limit of the emitters during the plasma phase.

B. Long-term stability of the pressure measurement

To check the long-term stability of the pressure gauges, the calibration was repeated at the end of OP1.2b. Again, a pressure ramp

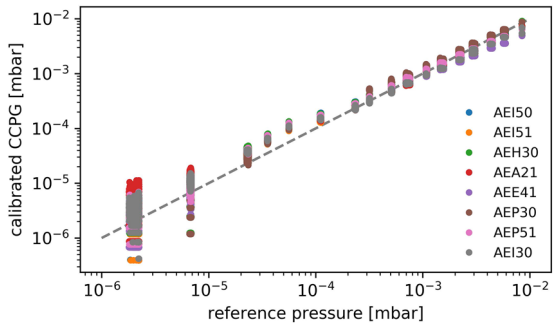

FIG. 9. Comparison of the reference pressure and calibrated CCPG sensor data overplotted with the dashed line of ideal match. For the CCPGs, the calibration from beginning of the campaign was used; the signal and reference pressure were measured at the end of the campaign. All CCPGs still work and show no significant sensor drift.

was carried out with a hydrogen gas inlet into the plasma vessel with closed gate valves, i.e., without plasma. The magnetic field was set to the standard configuration. Figure 9 shows the result of the procedure using the individual calibration factors determined at the beginning of OP1.2b (see Table I). All pressure gauges measure the pressure steps within a certain interval; above 10^{-5} mbar, there is no pressure gauge with a larger deviation than the estimated 15% accuracy. All pressure gauges were fully functional after 40 h operation in the magnetic field. Only one CCPG in port AEP51 had a temporary problem: the heating current showed some low frequency oscillations, but these disappeared after a while.

C. Visual inspection of the CCPGs after operation

After OP1.2b, all CCPGs were removed. The pressure gauge heads were dismounted from the plug-ins and stored in a desiccator. We found no degradation of the emitter units. The gauge head from port AEP51 may serve as an example (Fig. 1). This position was selected because we measured the highest neutral pressures there. Only a thin layer is visible on the control electrode, but it does not affect operation. Such a layer was expected because some cathode material is evaporated during operation. This result suggests that all emitters can be used again in the next operation phase, in contrast to the APGs. Some tungsten cathodes were heavily deformed in the magnetic field and could not be operated over the whole of OP1.2b. An example of such a deformation is given in Ref. 5.

VI. CONCLUSION

The CCPGs exhibited a very good performance in Wendelstein 7-X during OP1.2b. We demonstrated the operation of nine pressure gauges over 40 h in a magnetic field of about 2.1 T without failure. We believe that the stable behavior of the CCPGs is due to the strong reduction in the heating current. Data were used to characterize particle exhaust and neutral compression in the island divertor with an accuracy of 15%. The robust design we hoped to achieve was confirmed: the LaB_6 emitter had no problems with boronization of the vacuum vessel, gas injection into the vacuum vessel for radiation cooling, or the hydrogen gas at high neutral pressures.

The next campaign, operation phase 2 (OP2), is planned with an actively cooled island divertor for long-pulse operation. Because of the persistent problems with the APGs (with thoriated tungsten cathodes), we have decided to equip Wendelstein 7-X only with CCPGs for the future. A full setup with 18 CCPGs will allow a more comprehensive testing of this new concept during long-pulse plasma operation and, hopefully, over longer operation times in a magnetic field.

ACKNOWLEDGMENTS

We would like to thank B. Magera and B. Mackie from AP-TECH for supplying the LaB_6 cathodes. A. Scarabosio wrote the software for testing the CCPG prototype in the superconducting magnet. We also thank A. Graband for excellent technical support.

This work has been carried out within the framework of the EUROfusion Consortium and has received funding from the Euratom Research and Training Programme 2014-2018 and 2019-2020 under Grant Agreement No. 633053. The views and opinions expressed herein do not necessarily reflect those of the European Commission.

REFERENCES

[1]G. Haas and H.-S. Bosch, "In vessel pressure measurement in nuclear fusion experiments with ASDEX gauges," Vacuum **51**, 39–46 (1998).
[2]C. C. Klepper, T. E. Evans, G. Haas, G. L. Jackson, and R. Maingi, "Neutral pressure studies with a fast ionization gauge in the divertor region of the DIII-D tokamak," J. Vac. Sci. Technol., A **11**(2), 446–450 (1993).
[3]A. Scarabosio, G. Haas, H. W. Müller, R. Pugno, and M. Wischmeier, "Measurements of neutral gas fluxes under different plasma and divertor regimes in ASDEX Upgrade," in *Proceedings of the 18th International Conference on Plasma-Surface Interactions in Controlled Fusion Devices* [J. Nucl. Mater. **390-391**(Suppl. C), 494–497 (2009)].
[4]A. Arkhipov, A. Scarabosio, G. Haas, F. Mackel, J. Koll, H. Meister, H. Eixenberger, O. Paz, F. Seyvet, S. Terron, and P. Andrew, "Status of the development of diagnostic pressure gauges for the operation in ITER," Fusion Eng. Des. **123**, 1049 (2016).
[5]U. Wenzel, T. Kremeyer, G. Schlisio, M. Marquardt, T. S. Pedersen, O. Schmitz, B. Mackie, J. Maisano-Brown, and W7-X Team, "Advanced neutral gas diagnostics for magnetic confinement devices," J. Instrum. **12**(09), C09008 (2017).
[6]G. Haas, R. E. Wirth, H. J. Albrecht, J. Ehrenberg, T. Schneider, and H. Völkel, "Tests of pressure gauges in high-magnetic fields at Forschungszentrum Karlsruhe (FZK)," Technical Report IPP 2019-14, Max-Planck-Institut für Plasmaphysik, Garching, Germany, 2019, http://hdl.handle.net/21.11116/0000-0003-F279-4.
[7]U. Wenzel, T. S. Pedersen, M. Marquardt, and M. Singer, "An ionization pressure gauge with LaB_6 emitter for long-term operation in strong magnetic fields," Rev. Sci. Instrum. **89**(3), 033503 (2018).
[8]S. F. Vogel, "Pyrolytic graphite in the design of a compact inert heater of a lanthanum hexaboride cathode," Rev. Sci. Instrum. **41**(4), 585–587 (1970).
[9]Y. Feng, F. Sardei, P. Grigull, K. McCormick, J. Kisslinger, and D. Reiter, "Physics of island divertors as highlighted by the example of W7-AS," Nucl. Fusion **46**, 807–819 (2006).
[10]J. Im, S. Yang, and Y. Lee, "Investigation of the hydrogen storage mechanism of expanded graphite by measuring electrical resistance changes," Bull. Korean Chem. Soc. **33**, 3033–3038 (2012).
[11]M. Kim, "The new attempts for the in-vessel pressure gauge operation in the KSTAR plasma," Fusion Eng. Des. **146**, 2011–2014 (2019).

B
Acknowledgements

This work has been carried out within the framework of the EUROfusion Consortium and has received funding from the Euratom research and training programme 2014-2018 and 2019-2020 under grant agreement No 633053. The views and opinions expressed herein do not necessarily reflect those of the European Commission.

First I would like to thank my academic supervisor Prof. Thomas Sunn Pedersen for accepting me as a Ph.D. student, providing guidance during my research and the strong support for the DRGA project. Another important person is my daily supervisor Dr. Uwe Wenzel, whom I'd like to thank for the warm welcome in IPP and who spend a lot of time especially in the beginning introducing me to the field and provided guidance and insight throughout my thesis project.

I'd like to thank Dr. Chris C. Klepper for the idea to bring the P-DRGA to W7-X and Dr. Ralf König, who instantly saw both the possibilities and the window of opportunity before OP1.2b. Dr. Jeff H. Harris pushed the DRGA project over all administrative hurdles at ORNL, US-ITER and DOE, and supported me on all ends.

In the course of the integration of the P-DRGA at W7-X I received tremendous support from both ORNL staff (Dr. T. M. Biewer, C. Marcus) as well as many IPP staff: Project coordination, quality management, design department, mechanical workshop, assembly, welding workshop, CoDaC and operation department. Large support also came from engineers and technicians in E4, namely Dirk Pilopp, Marc Gamradt, Georg Isberner, Dirk Rondeshagen, Alex Card and Marco Krause.

Throughout my Ph.D. project, the vacuum group, notably Dr. Heinz Grote, Olaf Volzke and Holger Viebke, have been a valuable resource for both technical details and solutions as well as discussion of basic principles and methods.

The HEPP graduate school offered great possibilities to improve soft skills, gain presentation experience and even attend conferences. Dr. Birger Buttenschön has always with full commitment seeked to support the doctoral researchers in the HEPP, and I'd like to thank him for his dedication.

The daily work in the office was very pleasant thanks to many fruitful discussions with my office mates Valeria, Marco and Alex. Fellow Ph.D. students and Post-Docs from the institute, namely Holger, Doro, Felix, Lukas, Victoria and many more have contributed to my general understanding of fusion, plasma physics, W7-X, and also politics and virtually every other topic imaginable. I'd like to thank Dr. Udo Höfel and Dr. Daniel Böckenhoff for creating, maintaining and supporting the LaTeX thesis template, which makes making shiny theses a walk in the park and served as sound base for the layout of this thesis.

And then, I'd also like to thank all of my friends and family outside of IPP, who always followed my work with interest, visited and kept asking about new insights. Special thanks goes to Karla for thoroughly reading the introduction and providing lots of helpful feedback, and also continued interest in work and work-live-balance questions throughout the Ph.D. project. Last but not least I want to thank my wife for her continuous support and patience, especially during times of high work load and much extended working hours.

Thank you all, this thesis would not have been possible without your support.

Statutory declaration

Eigenständigkeitserklärung

Hiermit erkläre ich, dass diese Arbeit bisher von mir weder an der Mathematisch-Naturwissenschaftlichen Fakultät der Universität Greifswald noch einer anderen wissenschaftlichen Einrichtung zum Zwecke der Promotion eingereicht wurde. Ferner erkläre ich, dass ich diese Arbeit selbstständig verfasst und keine anderen als die darin angegebenen Hilfsmittel und Hilfen benutzt und keine Textabschnitte eines Dritten ohne Kennzeichung übernommen habe.

Greifswald, 30.09.2020

Georg Schlisio